INFORMATION TO USERS

This manuscript has been reproduced from the microfilm master. UMI films the text directly from the original or copy submitted. Thus, some thesis and dissertation copies are in typewriter face, while others may be from any type of computer printer.

The quality of this reproduction is dependent upon the quality of the copy submitted. Broken or indistinct print, colored or poor quality illustrations and photographs, print bleedthrough, substandard margins, and improper alignment can adversely affect reproduction.

In the unlikely event that the author did not send UMI a complete manuscript and there are missing pages, these will be noted. Also, if unauthorized copyright material had to be removed, a note will indicate the deletion.

Oversize materials (e.g., maps, drawings, charts) are reproduced by sectioning the original, beginning at the upper left-hand corner and continuing from left to right in equal sections with small overlaps. Each original is also photographed in one exposure and is included in reduced form at the back of the book.

Photographs included in the original manuscript have been reproduced xerographically in this copy. Higher quality 6" x 9" black and white photographic prints are available for any photographs or illustrations appearing in this copy for an additional charge. Contact UMI directly to order.

UMI

A Bell & Howell Information Company
300 North Zeeb Road, Ann Arbor MI 48106-1346 USA
313/761-4700 800/521-0600

Reproduced with permission of the copyright owner. Further reproduction prohibited without permission.

Reproduced with permission of the copyright owner. Further reproduction prohibited without permission.

HIGH PERFORMANCE OPTOELECTRONIC TRANSMITTERS FOR THE NEXT GENERATION OPTICAL SYSTEMS

by

Ramanarayanan Jambunathan

A dissertation submitted in partial fulfillment
of the requirements for the degree of
Doctor of Philosophy
(Electrical Engineering)
in The University of Michigan
1997

Doctoral Committee:

Professor Pallab Bhattacharya, Co-Chair
Professor Jasprit Singh, Co-Chair
Associate Professor Theodore Norris
Professor Duncan Steel

Reproduced with permission of the copyright owner. Further reproduction prohibited without permission.

UMI Number: 9732105

UMI Microform 9732105
Copyright 1997, by UMI Company. All rights reserved.

This microform edition is protected against unauthorized copying under Title 17, United States Code.

UMI
300 North Zeeb Road
Ann Arbor, MI 48103

Reproduced with permission of the copyright owner. Further reproduction prohibited without permission.

© Ramanarayanan Jambunathan 1997
All Rights Reserved

Reproduced with permission of the copyright owner. Further reproduction prohibited without permission.

To my parents, for all of their love and guidance

Reproduced with permission of the copyright owner. Further reproduction prohibited without permission.

ACKNOWLEDGEMENTS

The path from green apprentice to fledgling scientist is a tremendous journey of intellectual and personal growth. Along the way, my life has been graced by many individuals, the effects of which I am sure I will never be able to fully realize. It is my hope that the small measures of gratitude expressed here will convey some sense of the appreciation I have toward the people I have encountered along the way.

First, I would like to thank Professor Singh and Professor Bhattacharya for the wisdom, patience, and guidance they have afforded me in my graduate studies. Professor Singh was kind enough to mentor me, and it was his excellent suggestion that I approach Professor Bhattacharya with the intention of carrying out experimental work to balance the theoretical studies I would be undertaking. I would like to thank Professor Bhattacharya for allowing me to perform research in his laboratories, filled with equipment and resources few other university research groups can match. I'd also like to thank my co-mentors for affording me the opportunity to publish papers and attend conferences; my knowledge and enthusiasm greatly increased from these experiences.

Deb Swartz, Linda Jaarda, Betty Cummings, and Mikki Hale are all instrumental in making administrative processes run smoothly, and were always immediately helpful in assisting me with a problem or were kind enough to lend an ear when frustrations mounted. I salute them and give them my sincere appreciation

Being part of large research group allowed me to interact with many other stu-

Reproduced with permission of the copyright owner. Further reproduction prohibited without permission.

dents and research fellows, solidifying my understanding in not only my chosen topic but also a breadth of topics as well. Special thanks should go to Dr. Igor Vurgaftman for giving me his invaluable guidance when I first joined. I'd also like to thank Dr. Sanjay Sethi, Dr. Kaiyan Zhang, and Dr. Xiangkun Zhang for useful discussions. I am grateful to have collaborated with Dr. Howard Yoon regarding the tunneling injection laser. Dr. Paul Freeman merits significant appreciation from me for his help in Unix-, life-, and computer game-related topics.

A special note of gratitude I give to Dr. Kishore Kamath, who gave me terrific advice on my research throughout my study. Kishore was always willing to help me understand a problem or grow a structure regardless of his own time constraints. I hope to emulate his selflessness.

I am fortunate to have associated with several other students here. I'd like to thank Omar Qasimeh, Jae-Sung Rieh, Mike Gerhold, Hong-Tao Jiang, Jamie Phillips, Boaz Kochman, Dan Haver, and Peter Goetz for fruitful office discussions and banter. I benefitted greatly collaborating with Ya-hsing Yuan on integrated laser-modulator and DBR laser studies. Kojo Linder was a most accomodating office partner for the untidy excuse I labeled a desk. I will always have warm memories from the collaboration and friendships I was priveleged to have with Herte Gebretsadik, Dave Klotzkin, and Kao-Chih Syao.

Fond memories will be had of the "late-night" crew as well: Kao-Chih, Herte, Ya-hsing, Kojo, Jae-Sung, Omar, and Arjun Selvakumar, toiling away at hours most people, nay, even most graduate students would consider "not quite sane". I will remember and attempt to incorporate the tremendous work ethic and enthusiasm these friends had.

There were people I did not directly work with, who helped me, that I feel

Reproduced with permission of the copyright owner. Further reproduction prohibited without permission.

should also be acknowledged. I'd like to thank Sunil Bindiganavale for help on my initial work in FEM. Sanjay Raman was kind enough to let me peruse the Radiation Laboratory's selection of equipment.

Although finding free time here appeared to be a futile endeavor, on the occasions it was stumbled upon I was able to make use of it with the help of my cohorts. My former roommates Dave Ladd and Justin Yunke were good people to relieve stress with. Late night discussions with Erik Berg and Phil Marsh always promised to be a colorful journey into the unknown. Don Sawdai, Egor Alekseev, Jim Webster, and Peter were among my earliest friends here at U of M, and I'm thankful for their friendship, and that they would take the trouble to ask me if I would do something with them, even if they knew it was a moot point. I'd like to thank Dave for being a great partner in running and duathlon training. Herte, Dave, Arjun, Tracy Bell, Frank Bannon, and Jan Palmer all were fellow pillars of the "support group". And, I'd like to thank Jan for her friendship, support, and help in dominating the Fall and Spring UM tennis tournaments.

Finally, and most importantly, I give my wholehearted gratitude to my parents. Undoubtedly, without their love, support, and guidance, I would never have trodded down this path.

Reproduced with permission of the copyright owner. Further reproduction prohibited without permission.

TABLE OF CONTENTS

DEDICATION ii

ACKNOWLEDGEMENTS iii

LIST OF FIGURES x

LIST OF TABLES xvi

LIST OF APPENDICES xvii

CHAPTER

I. INTRODUCTION 1

1.1 Motivation 1
1.2 Transmission Schemes 2
1.2.1 Large Signal (Pulse Code) Modulation 2
1.2.2 Small Signal Modulation 3
1.2.3 Time Division Multiplexing 3
1.2.4 Subcarrier Multiplexing 3
1.2.5 Coherent Detection 4
1.2.6 A Novel System Utilizing the Concept of Gain Switching 7
1.3 Laser Issues in Optical Transmission Systems 8
1.3.1 Linewidth and the Linewidth Enhancement factor . 8
1.3.2 Nonuniform Charge Injection 9
1.3.3 Large Signal Modulation Using Gain Switching . . . 10
1.3.4 Monolithic Implementation and Short Cavity Lasers 10
1.4 Thesis Outline 11

II. OPTOELECTRONIC FORMALISM 13

2.1 Motivation and Background 13
2.2 Calculation of the Bandstructure 16
2.2.1 The k · p Method 16
2.2.2 Describing conduction band states 18

Reproduced with permission of the copyright owner. Further reproduction prohibited without permission.

2.2.3 Describing valence band states 19
2.2.4 Incorporating biaxial strain 20
2.3 Density of States Calculation 22
2.4 Calculation of Laser Characteristics 27
2.4.1 Calculation of Gain and Spontaneous Emission Rates 29
2.4.2 Current and Photon Density Calculations 31

III. STRAIN AND TEMPERATURE DEPENDENCE OF THE LINEWIDTH ENHANCEMENT FACTOR 35

3.1 Motivation 35
3.2 Theoretical Calculations 36
3.2.1 Background 36
3.2.2 Calculations 37
3.2.2.1 $In_xGa_{1-x}As/GaAs$ calculations 37
3.2.2.2 $In_{1-x}Ga_xAs_yP_{1-y}/InP$ calculations . . . 40
3.3 Experimental Results 46
3.4 Conclusions 52

IV. EFFECTS OF NON-UNIFORM CHARGE INJECTION ON GAIN, THRESHOLD CURRENT, AND LINEWIDTH ENHANCEMENT FACTOR FOR InP-BASED AND GaAs-BASED MULTIPLE QUANTUM WELL LASERS 57

4.1 Introduction 57
4.2 Formalism 58
4.3 Theoretical Results 62
4.4 Conclusions 69

V. CARRIER DYNAMICS INVESTIGATIONS USING LARGE PULSE MODULATION 73

5.1 Introduction 73
5.2 Formalism 75
5.3 Experiment 79
5.4 Discussion 83
5.4.1 Analysis of output pulses 83
5.4.2 MLQD performance 90
5.4.3 Jitter 90
5.4.4 Chirp 91
5.5 Conclusions 91

VI. WAVE PROPAGATION FORMALISM 93

Reproduced with permission of the copyright owner. Further reproduction prohibited without permission.

6.1 Motivation 93
6.2 Background 95
6.3 Studies in Two Dimensions 96
6.3.1 Formalism 96
6.3.2 Implementation 98
6.3.3 Improvements for Fast Computation 100
6.3.3.1 Variable Finite-Differences 101
6.3.3.2 Symmetry Considerations 102
6.3.3.3 Boundary Termination 105
6.3.4 Application 108
6.4 Studies in Three Dimensions 116
6.4.1 Formalism 116
6.4.2 Implementation 117
6.4.2.1 Iterative Methods 117
6.4.2.2 Successive Overrelaxation 118
6.4.2.3 Mesh Traversal 121
6.4.2.4 Terminating Successive Approximations 122
6.4.2.5 Symmetry Considerations 124
6.4.2.6 Simulation Region Size 124
6.4.2.7 Timestep size 124
6.4.3 Application 125

VII. DESIGN STUDIES FOR DISTRIBUTED BRAGG REFLECTORS FOR SHORT CAVITY EDGE EMITTING LASERS 130

7.1 Introduction 130
7.2 Formalism 132
7.3 Results 134
7.3.1 Simulation Characteristics 134
7.3.2 Periodically Spaced Mirrors With Abrupt Surfaces . 136
7.3.3 Aperiodically Spaced Mirrors With Abrupt Surfaces 138
7.3.4 Periodically Spaced Mirrors With Non-Uniform Surfaces 139
7.3.5 Wavelength Dependence of the Reflectivity of the External DBR 141
7.3.6 Periodically Spaced Mirrors with Varying Gap Dielectrics 146
7.4 Experimental Results 148
7.5 Conclusions 148

VIII. CONCLUSIONS AND RECOMMENDATIONS FOR FUTURE STUDY 155

8.1 Review of present work 155

Reproduced with permission of the copyright owner. Further reproduction prohibited without permission.

8.2 Suggestions for future work 157

APPENDICES 162

BIBLIOGRAPHY 180

Reproduced with permission of the copyright owner. Further reproduction prohibited without permission.

LIST OF FIGURES

Figure

1.1 Typical multiplexed transmission schemes: (a) TDM, (b) SCM. After [6]. 5

1.2 Block diagram of a typical coherent detection system. After [9]. . . 6

1.3 Architecture for high speed serial data transmission system examined in this thesis. 8

2.1 The structure of a typical high-performance laser. 15

2.2 Valence bandstructure along the [100] and [110] directions in a 50 ÅGaAs/$Al_{0.3}Ga_{0.7}As$ (on GaAs) quantum well. 22

2.3 Valence bandstructure along the [100] and [110] directions in a 50 Å$In_{0.1}Ga_{0.9}As$/$Al_{0.3}Ga_{0.7}As$ (on GaAs) quantum well. 23

2.4 Valence bandstructure along the [100] and [110] directions in a 50 Å$In_{0.2}Ga_{0.8}As$/$Al_{0.3}Ga_{0.7}As$ (on GaAs) quantum well. 24

2.5 Valence bandstructure along the [100] and [110] directions in a 50 Å$In_{0.3}Ga_{0.7}As$/$Al_{0.3}Ga_{0.7}As$ (on GaAs) quantum well. 25

2.6 The hole density of states functions for a 50 ÅIn_xGa_{1-x}/$Al_{0.3}Ga_{0.7}As$ (on GaAs) quantum well. 28

2.7 Peak TE mode material gain versus injected carrier density for a 50 ÅIn_xGa_{1-x}/$Al_{0.3}Ga_{0.7}As$ (on GaAs) quantum well. 31

2.8 Spontaneous emission rate versus injected carrier density for 50 ÅIn_xGa_{1-x}/$Al_{0.3}Ga_{0.7}A$ (on GaAs) quantum well. 32

2.9 Total photon density versus injected carrier density for 50 ÅIn_xGa_{1-x}/$Al_{0.3}Ga_{0.7}As$ (on GaAs) quantum well. 34

Reproduced with permission of the copyright owner. Further reproduction prohibited without permission.

3.1 Peak material gain versus radiative carrier density for a 50 Å $In_xGa_{1-x}As$ well (on GaAs) at (a) 300K and (b) 77K. 39

3.2 Linewidth enhancement factor versus radiative carrier density for a 50 Å$In_xGa_{1-x}As$ well (on GaAs) system at (a) 300K and (b) 77K. . 41

3.2 (c) Linewidth enhancement factor versus peak material gain for a 50 Å $In_{0.1}Ga_{0.9}As$ QW on GaAs, showing the different contributions to α. 42

3.3 Peak material gain versus radiative carrier density for a 50 Å $In_{1-x}Ga_xAs_yP_{1-y}$ well (on InP) with (a) compressive strain and (b) tensile strain. . . 43

3.4 Linewidth enhancement factor versus radiative carrier density for a 50 Å $In_{1-x}Ga_xAs_yP_{1-y}$ well (on InP) (a) compressive strain and (b) tensile strain. 44

3.5 Carriers confined in the wells do not contribute to the plasma effect for the TM polarization as they are not free to move in the along in the transverse direction. After [37]. 45

3.6 MQW-SCH strained layer laser structure used for the devices under study in this chapter. From [41]. 46

3.7 The experimental setup used for measuring linewidth enhancement factor. 47

3.8 The spectrum for the 4 QW $In_{0.63}Ga_{0.37}As$/InP laser at T=20C (a) slightly above threshold and (b) slightly below threshold. 50

3.8 (c) spectra for the 4 QW $In_{0.63}Ga_{0.37}As$/InP laser at two currents below threshold and (d) $G(\lambda)$. 53

3.9 Measured linewidth enhancement factor versus composition for the devices, at different temperatures, for the devices used in this study. 54

3.10 Measured linewidth enhancement factor versus temperature for the 4QW $In_{.58}Ga_{.42}As$/InP laser. The plot indicates the error due to temperature fluctuations and spectrometer resolution. 55

3.11 A plot of $\frac{d\lambda}{dT}$ with In composition for the devices studied. From [47]. 56

4.1 (a) Visualization of non-uniform charge injection into a MQW structure from the n-injection side. 60

Reproduced with permission of the copyright owner. Further reproduction prohibited without permission.

4.1 (b) Normalized injected electron density distribution for an 8-well MQW laser for the uniform and non-uniform charge injection cases considered in this study. 61

4.2 Single well gain spectrum of the well closest to the n-injection side and the well closest to the p-injection side for L_d = 783 Å, and single well gain spectrum of well under uniform injection. The slight irregularities in the gain curves are a consequence of the numerical procedure and have no noticeable effect on the quoted results. . . . 64

4.3 Total peak gain versus total injected carrier density for an 8-well quantum well laser for the uniform and non-uniform charge injection cases considered in this study. 66

4.4 Total spontaneous emission rate versus total injected carrier density for an 8-well quantum well for the uniform and non-uniform charge injection cases considered in this study. 67

4.5 Threshold current density vs total active region gain for an 8-well quantum well structure for the L_d = 783 Å and uniform injection cases. 68

4.6 Linewidth enhancement factor versus total injected carrier density for an 8-well quantum well structure for the uniform and non-uniform charge injection cases considered in this study. 70

4.7 Total differential gain spectrum for an 8-well quantum well structure for the L_d = 783 Å and uniform injection cases, at two different injected carrier densities. The slight irregularities in the differential gain curves are a consequence of the numerical procedure and have no noticeable effect on the quoted results. 71

5.1 Experimental set-up for gain switching. 81

5.2 Equivalent circuit model used to fit $Z(\omega)$. 82

5.3 Real and parts of the complex impedance of the diode in the small signal regime. The current I_{bias} = 10 mA. 84

5.4 The input signal from the comb generator: (a) The input pulse train separated by 10ns, and (b) a single input from the comb generator. 85

Reproduced with permission of the copyright owner. Further reproduction prohibited without permission.

5.5 The output pulses from the 8 QW InP TIL laser: (a) The output pulse train separated by 10ns, and (b) a single output from the comb generator. Relaxation frequencies in (a) are due to the feedthrough. 86

5.6 Layer structure for the 8 QW InP-based TIL laser. 88

5.7 Calculated output for the InP-based TIL laser, where the input bias current is the solid line, carrier density N is the dotted line, and the photon density S is the dashed line. The width of the output optical pulse S is ~ 8 ps. 89

6.1 Constant and variable mesh spacings for a symmetric waveguide about a core of 0.1 μm. 103

6.2 (a) A symmetric waveguide and (b) the initial wavepacket injected into the waveguide. 104

6.3 (a) Reflection coefficient and (b) fraction of absorbed energy of an incident wavepacket at an air/absorber interface ($n_r = 1.0$) as a function of n_i. 107

6.4 (a) Layer structure and (b) refractive index profile of the 1.54μm laser-modulator. 109

6.5 Scanning electron micrographs of (a) the fabricated laser-modulator and (b) the coupling region. 110

6.6 Wavepacket propagation in the laser cavity of the integrated laser-modulator: (a) initial wavepacket injected into the laser cavity, (b) profile of wavepacket at the coupling facets. 112

6.6 Wavepacket propagation in the laser cavity of the integrated laser-modulator: (c) steady-state mode profile of the wavepacket in the laser cavity after reflection. 113

6.7 Effective reflectivity versus gap distance for the laser-modulator. The dashed portion of the curve indicates the effective reflectivity for the estimated value of d_g. 114

6.8 Threshold current density versus inverse cavity length characteristics for the 1.54μm integrated laser-modulator. 115

Reproduced with permission of the copyright owner. Further reproduction prohibited without permission.

6.9 (a) Magnitude of residual error vector versus iteration number and (b) oscillations in residual error vector after convergence for a typical case. 123

6.10 (a) The waveguide and (b) the associated fundamental eigenvector for the 3D simulation. 127

6.11 (a) The x- and z-components of the initial wavepacket, in the x-z plane at $y = 3\mu$m. 128

6.12 (a) The x- and z-components of the wavepacket upon reflection, in the x-z plane at $y = 3\mu$m. 129

7.1 A three-dimensional visualization of the basic structure for the model used in this study and (b) a two-dimensional projection of (a) with the corresponding parameters labeled. 133

7.2 Reflection coefficient calculations using the structure presented in Fig. 7.1 for 1,2,and 3 mirrors. The mirrors are periodically spaced and assumed to have uniform surfaces. 137

7.3 (a) The model for a structure assuming aperiodically spaced mirrors and (b) reflection coefficient calculations using the structure presented in (a). The mirrors are assumed to have uniform surfaces. 140

7.4 (a) the model for a structure assuming mirrors with nonuniform (parabolic) surfaces, and reflection coefficient calculations considering (b) one mirror. 142

7.4 (c) Reflection coefficient calculations considering two mirrors for the structure in (a). 143

7.5 External DBR wavelength reflectivity calculations using the structure presented in Fig. 7.1 considering (a) 1 mirror with $d_{gap} = \frac{\lambda_0}{4}$, and (b) 2 mirrors with $d_{gap} = \frac{\lambda_0}{4}$ 145

7.5 External DBR wavelength reflectivity calculations using the structure presented in Fig. 7.1 considering (c) 3 mirrors with $d_{gap} = \frac{\lambda_0}{4}$, and (d) 3 mirrors with $d_{gap} = \frac{3\lambda_0}{4}$ 150

7.5 External DBR wavelength reflectivity calculations using the structure presented in Fig. 7.1 considering (e) 5 mirrors with $d_gap = \frac{5\lambda_0}{4}$ 151

Reproduced with permission of the copyright owner. Further reproduction prohibited without permission.

7.6 Reflection coefficient calculations using the structure presented in Fig. 7.1 considering 3 mirrors with varying gap refractive index. . . 152

7.7 A schematic and scanning electron micrograph of the edge emitting laser with air/semiconductor DBR mirror etched via RIE. (From [103]) 153

7.8 Measured L-I characteristics for edge emitting lasers with DBRs on one side. The light output is taken from the cleaved facet. (From [103].) 154

8.1 Envisioned short-period VCSEL examining (a) 3D view of mirror stack before etch with intermixing region shown, (b) 3D and 2D views of mirror stack after etch. 160

8.2 Edge emitting laser with DBR showing (a) 3D view of structure using flat mirrors as in Chapter VII, (b) top view of structure in (a), and (c) top view of structure in (a) with curved mirrors. The arrows are meant to emulate the light emerging from and being reflected by the laser cavity and the mirrors. 161

Reproduced with permission of the copyright owner. Further reproduction prohibited without permission.

LIST OF TABLES

Table

3.1 Parameters used in the calculations in this chapter. The listed values are for T=300K. 38

3.2 Measured threshold current density J_{th} versus and characterstic temperature T_0 versus device temperature for the compositions used in this study 48

5.1 Measured FWHM output at optimal bias currents for the different devices used in this study. 83

5.2 Relevant parameters used in large signal modulation calculations for the 8 QW InP-based TIL. 87

Reproduced with permission of the copyright owner. Further reproduction prohibited without permission.

LIST OF APPENDICES

Appendix

A. THE DEPENDENCE OF LINEWIDTH ON THE LINEWIDTH ENHANCEMENT FACTOR 163

A.1 Derivation of the linewidth enhancement factor 163
A.1.1 Anomalous dispersion 163
A.1.2 Plasma dispersion 166
A.2 Sources of phase fluctuations 166
A.3 Derivation of the phase rate equation 168
A.4 Linewidth enhancement 169

B. IMPROVEMENT OF STABILITY FOR THE PARABOLIC TWO-DIMENSIONAL WAVE EQUATION USING THE SLOW-WAVE APPROXIMATION 171

C. POTENTIAL LOCALLY ONE-DIMENSIONAL FINITE DIFFERENCE TIME DOMAIN SCHEMES FOR FULLY-VECTORIAL THREE DIMENSIONAL SIMULATIONS 175

C.1 Split 1: Incorporation of known field values at advanced timesteps 177
C.2 Split 2: Use of previous field values exclusively at advanced timesteps 178

Reproduced with permission of the copyright owner. Further reproduction prohibited without permission.

CHAPTER I

INTRODUCTION

1.1 Motivation

With 1996 being dubbed in the media as *The Year of the Internet* [1], the communications revolution, on a macroscopic level, was fully entrenched the public mind. More people got "plugged in" to the internet than ever before, and words such as "bandwidth" and "bit rate", once reserved for researchers, are now tools of laymen who use such terms as bargaining points in the purchase of their internet port. It is not enough for a person to have but a simple one-dimensional cellular phone; now one can purchase a computer/phone hybrid no larger than the cellular phone of a decade ago [2]. And as the demand for miniaturization and integration of different components increases, so does the demand for increased speed, from both a wider system viepoint and a more in-depth device viewpoint.

On the device level, a communication system (such as the internet link described above) is composed of an incoming signal, a transmitter, a communication link, a receiver, and the receiver's output. The transfer of data is achieved using the propagation of electromagnetic waves through the communication link, be it a transmission line, atmosphere, or an optical fiber. Given that the advantages of optoelectronic technologies include smaller device size, reduction in EMI, and low-cost of fiber optic

Reproduced with permission of the copyright owner. Further reproduction prohibited without permission.

cable, research has accelerated in the last quarter-century on optical data transmission systems.

1.2 Transmission Schemes

In the following sections will be briefly outlined three common optical transmission schemes, along with a fourth scheme which will be examined in detail in this thesis. The first two, the pulse code modulation (PCM) and the small signal modulation (SSM) systems, rely on the amplitude of the pulse to be modulated. The third method, coherent detection has the additional features of allowing the phase and frequency of the carrier wave to be modulated as well. Noting advantages and disadvantages of these systems leads to the discussion of a fourth systems involving large signal modulation utilzing time-division multiplexing (TDM) and space division multiplexing (SDM) to achieve high speed data transmission.

1.2.1 Large Signal (Pulse Code) Modulation

The most basic system for communication has been the on/off system for transmitting information. With this in mind, the semiconductor laser can be operated in a manner similar to which the ancient smoke signal was used to transmit data streams over long distances using zeros and ones (pulses). A PCM system is implemented first biasing the laser above threshold with a current I_b. Utilizing stimulated emission, the application of an additional current I_m to the laser causes a large number of photons to be emitted. Thus a "1" has been transmitted. Conversely, the bias current I_b alone yields a photon output corresponding to a "0". By ensuring the bias remains above threshold, the modulation depth remains high while the laser response remains relatively fast ($\sim$10 GHz). However, the lasing spectrum under pseudorandom PCM depends on the bit pattern input due to a redistribution of

Reproduced with permission of the copyright owner. Further reproduction prohibited without permission.

power in the lasing modes [3]. In addition, the modulation bandwidth decreases as the modulation depth increases, compared to that of small signal modulation [4].

1.2.2 Small Signal Modulation

Much like the PCM method, the small signal modulation involves impressing an additional signal on the input bias to the transmitting laser. Unlike PCM, though, the modulating current is significantly smaller than I_b ($\frac{I_m}{I_b} < 10\%$). The modulation depth is therefore smaller than in PCM. On the other hand, the largest modulation bandwidth possible is obtained. Recently, a measured bandwidth of 43 GHz (CW) and an intrinsic bandwidth of 110 GHz have been reported using a tunneling-injection multi-quantum well laser structure [5].

1.2.3 Time Division Multiplexing

In a time division multiplexed (TDM) optical system, as in Fig. 1.1(a), N channels each with bit rate B are electrically multiplexed. The TDM signal, now with bit rate NB is transmitted through an optical fiber and detected by a receiver with bandwidth $3NB$. The detected signal is then demultiplexed. The optical fiber bandwidth required is $2NB$, so each channel needs a bandwidth $2B$.

1.2.4 Subcarrier Multiplexing

In Fig. 1.1(b) N channels are multiplexed by a combiner in the microwave frequency range. The SCM signal modulates an optical modulator, which requires a bandwidth of $4NB$, assuming each channel requires a bandwidth $2B$ and subcarrier frequencies occupy a single octave band. The signal is then detected by a receiver with bandwidth $8NB$, and each channel is selected by its own electrical filter with bandwidth $2NB$. Since a bandwidth of $8NB$ is used in the fiber, this method requires

Reproduced with permission of the copyright owner. Further reproduction prohibited without permission.

a bandwidth of $8B$ per channel.

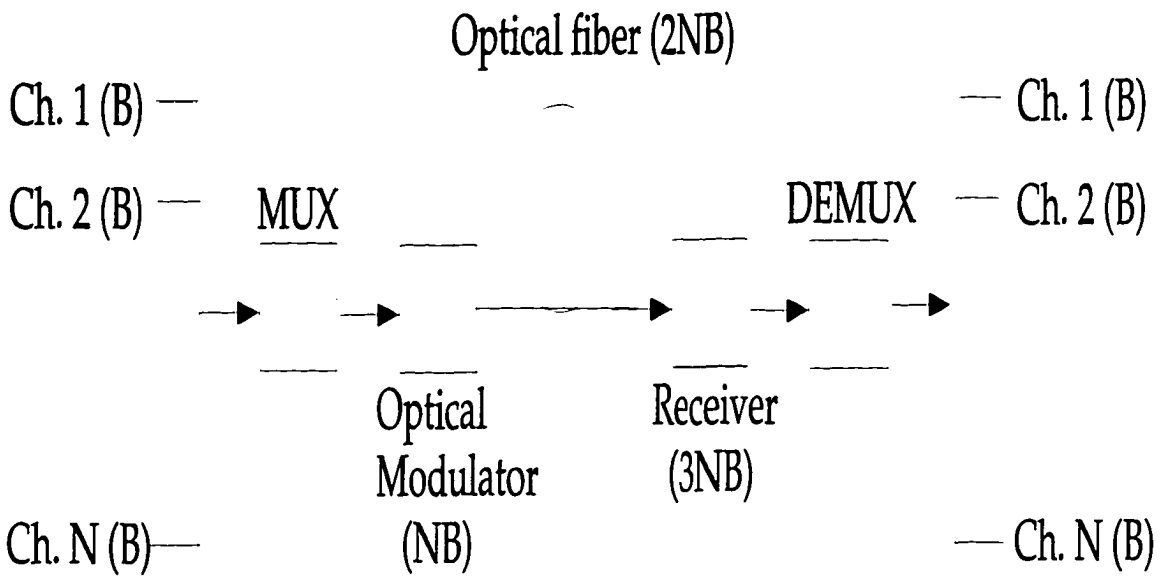
1.2.5 Coherent Detection

Coherent detection schemes represent the "holy grail" of communication. Introduced by Saito, Yamamoto, and Kimura [7], this method takes advantage of the optical fiber's nearly unlimited bandwidth [8] in moving vast amounts of data. Although since 1970 research on optical communication systems has progressed rapidly, coherent detection systems were limited by the large FM noise in the semiconductor lasers of that time, and therefore limited practical communication systems to PCM [9].

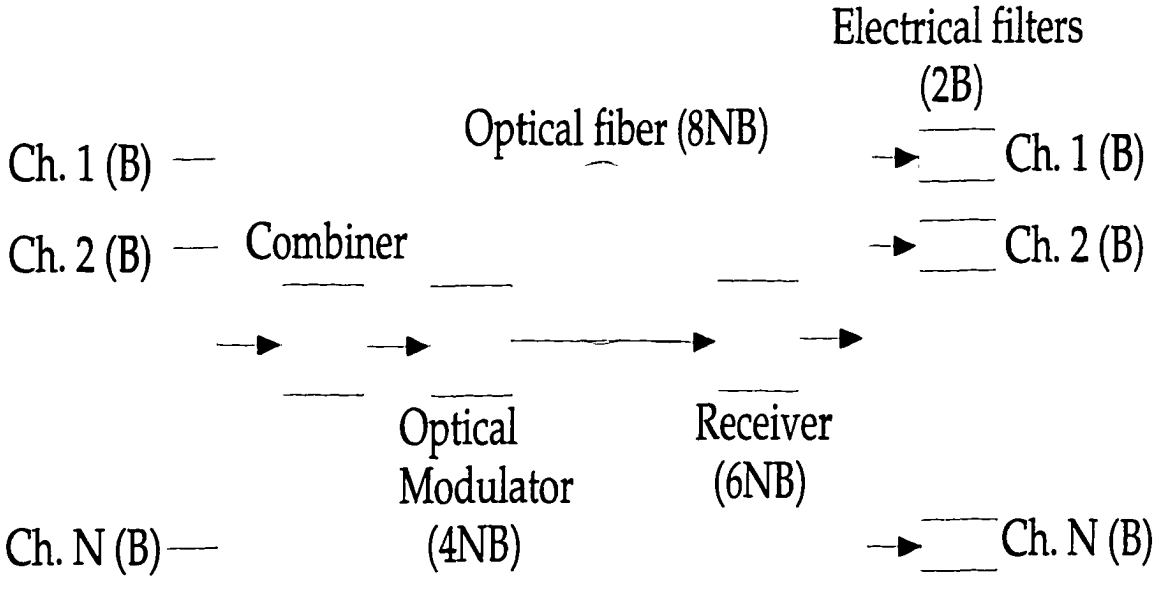
As soon as low FM noise semiconductor lasers (such as quantum well lasers) were developed, stable modulation of their frequencies became possible. A typical coherent detection system is presented in Fig. 1.2.5. By using a heterodyne or a homodyne demodulation system, the detection sensitivity becomes much higher than that of a conventional modulation/demodulation scheme, which also means the signal transmission span could be increased.

Coherent detection systems offer the advantages of allowing larger data capacity and the flexibility of a variety of modulation schemes. However, several stringent requirements are places on the components of these systems. To keep the bit-error rate (BER) low, a high extinction ratio is necessary [10]. Short frequency switching times are necessary for flexible OFDM systems [11]. The narrow laser linewidths required can be obtained by using a distributed feedback (DFB) laser at high injection currents; however, thermal drift becomes a problem [12]. These issues, resolved in microwave communications, have limited the use of coherent detection to field testing, though promising transmission rates as high as 1 Tbit/s have been reported [13].

Reproduced with permission of the copyright owner. Further reproduction prohibited without permission.



(a)



(b)

Figure 1.1: Typical multiplexed transmission schemes: (a) TDM, (b) SCM. After [6].

Reproduced with permission of the copyright owner. Further reproduction prohibited without permission.

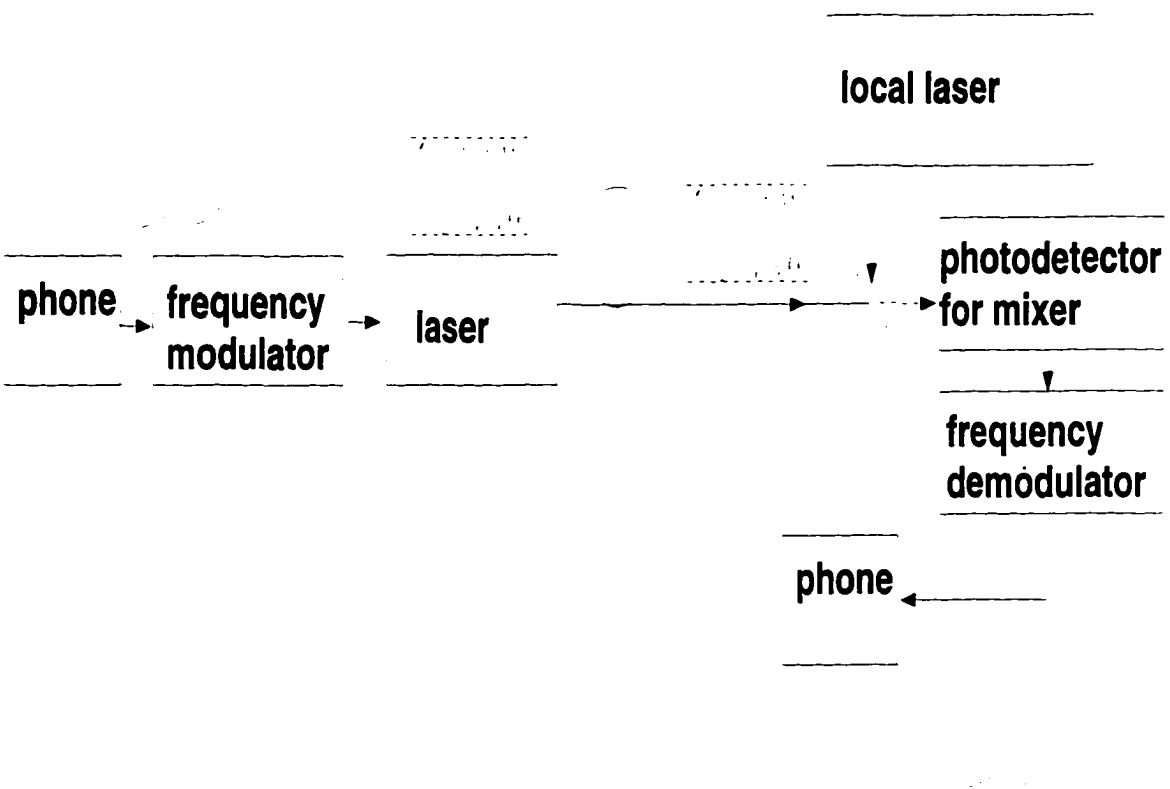


Figure 1.2: Block diagram of a typical coherent detection system. After [9].

Reproduced with permission of the copyright owner. Further reproduction prohibited without permission.

1.2.6 A Novel System Utilizing the Concept of Gain Switching

In the previous paragraphs standard transmission methods have been examined along with some mention of the positive and negative characteristics of each system. The systems based on amplitude modulation alone are easily realized but do not have the capability of exploiting the fiber bandwidth. Coherent detection systems can have extremely high transmission rates due to their versatility, but in the same token are difficult to realize. Can one combine the benefits of these systems into a high speed optical transmission system?

In this thesis, this question is examined using an amplitude modulation system incorporating both TDM and SDM. As stated before, large signal modulation systems are limited $\sim$ 10 GHz; this is because of the dependence of the large signal modulation relaxation oscillations on the spontaneous recombination time. However, these oscillations can be clipped off using gain switching.

An architecture that incorporates a multi-laser system is presented in Fig. 1.2.6. The envisaged system consists of N lasers as shown. The output of the lasers is coupled into the same outgoing fiber. The incoming electrical data stream is demultiplexed so each laser has a *short operation time and a long recovery time.* An incoming electrical data stream is multiplexed electronically across an array of lasers so that a single datum pulse causes gain switching of a particular laser. The next pulse is used to gain switch the next laser and so on. As a result, each laser is gain switched at a rate of B/N where B is the data rate of the incoming signal. Since N can be made to be $\sim$30, each laser has a fairly long recovery time before it is gain switched again.

The previous sections have given, from a general systems point of view, an introduction to types of transmission schemes which are (or could be) used to transmit

Reproduced with permission of the copyright owner. Further reproduction prohibited without permission.

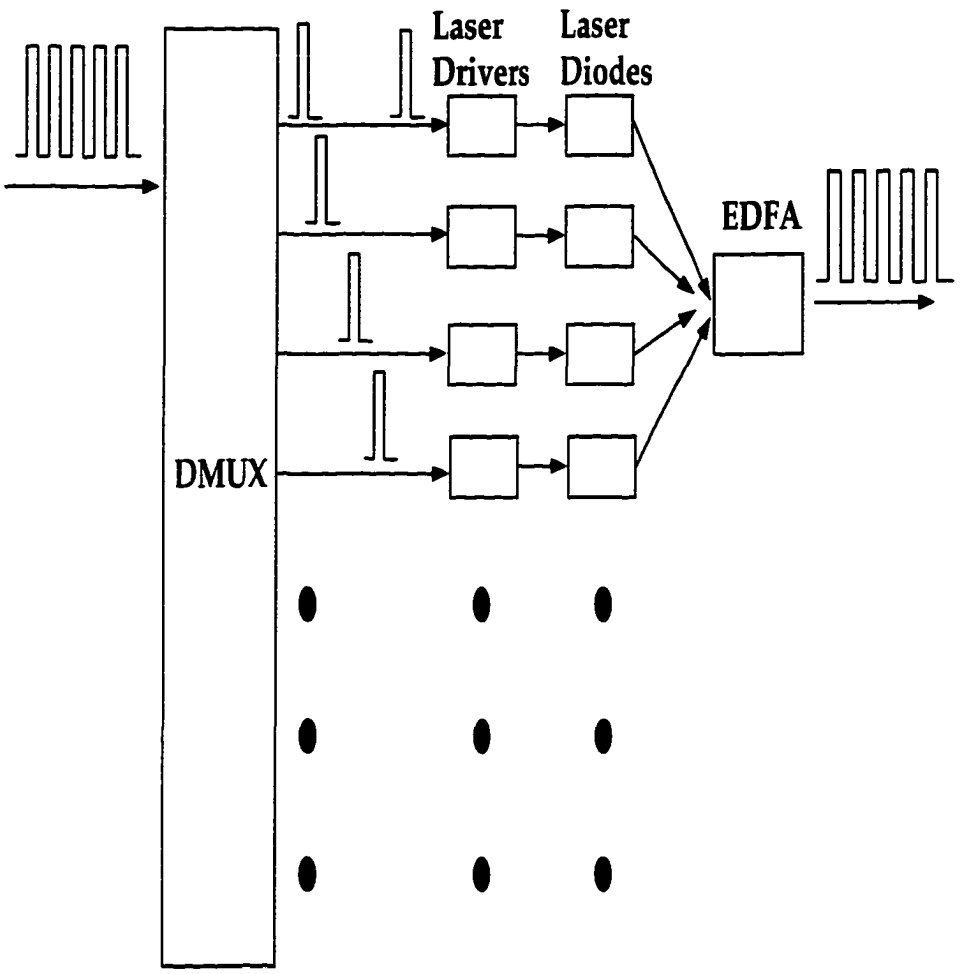


Figure 1.3: Architecture for high speed serial data transmission system examined in this thesis.

data. Factors such as bandwidth, linewidth, and intracavity photon power are important parameters which can affect the transmitters which drive these systems. Therefore an examination of these systems is incomplete without also addressing these issues.

1.3 Laser Issues in Optical Transmission Systems

1.3.1 Linewidth and the Linewidth Enhancement factor

As mentioned previously, the linewidth is a parameter encountered in coherent detection systems. Low-chirped lasing operation is desirable for high-speed high-

Reproduced with permission of the copyright owner. Further reproduction prohibited without permission.

bit rate optical transmission. Under direct modulation, the spectral chirping width [14],[15] is broadened by a factor of $1+\alpha^2$ [16], and the spectral linewidth exceeds the Schawlow-Townes limit by $1+\alpha^2$ [16], where α is known as the linewdith enhancement factor [14]. A reduction in α tends to reduce the waveform distortion due to the dispersion of optical fibers because the spectral spread induced by the chirping is suppressed. Hence, for optimal communication operation, is important to minimize α.

Strain engineering has become an important technology in the manufacturing of high frequency semiconductor components for optical systems. The use of strain has been demonstrated to improve many semiconductor laser characteristics, including mode gain, threshold current, multiple quantum well device fabrication, and device reliability. Additionally, low temperature operation of transmission systems has been suggested, due to the increases in gain and differential gain which low temperature operation provides. Such increases undoubtedly provide additional performance in the form of increased modulation bandwidth in amplitude modulation systems. However, it is also of interest to see the effect of temperature on coherent detection schemes via the change in the linewidth enhancement factor, and to see how the combination of both strain and temperature can minimize this parameter. I examine these concerns in Chapter 3.

1.3.2 Nonuniform Charge Injection

Indium-Phosphide based lasers rely heavily on multiple-quantum wells in order to overcome the large material loss associated with this system. Advantages of moving to a larger number of wells include a lower gain needed per well for lasing and enhanced differential gain, which in turn improves bandwidth. Generally when

Reproduced with permission of the copyright owner. Further reproduction prohibited without permission.

calculations are made and devices are designed it is assumed that charge is uniformly injected into the active region, with the number of electrons and holes in each well to be equal. However, it is reasonable to expect that the number of carriers (n or p) in each well will be unequal since carrier capture and emission rates differ. Thus, will designed-for and desired performanced be borne out, or does non-uniform injection seriously impair device performance? I examine this question in Chapter 4 with regard to gain, threshold current, and linewidth enhancement factor.

1.3.3 Large Signal Modulation Using Gain Switching

Earlier I discussed a PCM system incorporating an array of lasers in order to obtain a high bit-rate optical transmission system, utilizing gain switched pulses to drive the lasers. It is therefore important to understand the properties of a gain-switched pulse from a dynamic point of view. A study is undertaken in Chapter 5, involving carrier capture in two different types of laser structures, separate confinement heterostructure (SCH) and tunneling injection (TI), in order to understand how gain switching can affect laser transient response. After this, the novel transmission system is then discussed, with emphasis being placed on transmitter characteristics, such as output pulse width, jitter, and chirp.

1.3.4 Monolithic Implementation and Short Cavity Lasers

Reduction in device size for edge-emitting semiconductor laser devices offers gains in two areas: 1) lower parasitic capacitances and 2) increased component density per chip. In reducing parasitics we cause the 3dB bandwidth to increase. Since capacitance is proportional to area, via $C = \frac{\epsilon_0 A}{d}$, a reduction in device length would decrease the associated parasitic capacitance. However, low mirror reflectivities preclude the use of very short cavity edge-emitting lasers since the mirror loss is too

Reproduced with permission of the copyright owner. Further reproduction prohibited without permission.

high.

Typical edge-emitting distributed feedback (DFB) or distributed Bragg reflector (DBR) lasers, involving etch and regrowth steps, use a Bragg reflector placed in the path of the optical beam. Unfortunately the device construction is such that a very small fraction (~1–2%) of the beam sees the Bragg action. As a result, while these structures offer better mode selectivity, the overall mirror relectivity remains low. In addition, the slight change in index of refraction in these structures necessitates a large number of periods to be used, which eliminates their potential for use as a short cavity laser.

The question arises then, can one find a material which provides a large refractive index difference which could be used in a Bragg structure yielding a high reflectivity yet only a few periods? The answer is yes, if that "other" material is none other than air. In Chapter 7 a DBR design study for a short cavity laser is undertaken, in order to see how the air/semiconductor refractive index difference can be exploited.

1.4 Thesis Outline

The issues discussed in the preceeding sections necessitate a foundation upon which these issues may be studied. The concerns of linewidth enhancement, nonuniform injection, and laser response all appear to be centered around issues relating to bandstructure and opto-electronics formalism, while the issues of short cavity design would appear to be more appropriately dealt with using wave propagation theory. In fact, this is how how the situation has been approached.

In Chapter 2, the method of study with respect to optoelectronics, incorporating bandstructure, density of states, and gain spectra calculations, is detailed. The formalism presented in this chapter will provide the foundation for the work of Chapters

Reproduced with permission of the copyright owner. Further reproduction prohibited without permission.

3, 4, and 5.

The foundation for studies involving wave propagation is laid in chapter 6. After introducing the concepts, simulations involving a fast and flexible two-dimensional propagation simulator are presented, including the examination of an integrated laser-modulator. Expanding on this, an example study is carried out involving a more powerful three-dimensional fully vectorial simulator. Issues involving both the conceptual and practical aspects of such implementations are discussed.

Reproduced with permission of the copyright owner. Further reproduction prohibited without permission.

CHAPTER II

OPTOELECTRONIC FORMALISM

2.1 Motivation and Background

The multiple-quantum well (MQW) laser is the primary transmitter in high-speed optoelectronic systems today, and therefore will be at the heart of the work in this thesis. The QW laser holds significant advantages over its bulk heterostructure counterparts, including higher mode material gain and differential gain, leading to smaller threshold currents and higher modulation bandwidths. Growth of QW lasers has been actively researched over the last fifteen years and is well-understood, unlike issues now being raised in the promising quantum dot-based devices. Quantum wire lasers provide only small additional benefits for the difficulty in the growth and fabrication of such devices.

The success of novel optoelectronic devices has relied on basis of well-developed materials engineering. The development of molecular beam epitaxy (MBE) by Cho in the early 1970's [17] created a multitude of opportunities to realize multilayer heterostructures with atomic monolayer precision. The advent of other semiconductor growth techniques such as metalorganic chemical vapor deposition (MOCVD) further increased the capability to tailor the bandstructures of semiconductors.

When a feature size of a device is on the order of a deBroglie wavelength, as in a

Reproduced with permission of the copyright owner. Further reproduction prohibited without permission.

quantum well laser, the electronic states become quantized. The formation of discrete energy subbands in the conduction and valence bands depending on the quantum well thickness and the effective masses allows the capability to tune the emission wavelength. In addition, the density of states of a two-dimensional structure can be altered so that the bandedge population of carriers is increased, resulting in a reduced transparency carrier density and threshold current compared to a bulk structure.

In Fig. 2.1 is a schematic of a typical high performance MQW laser. During lasing electrons injected from the n-contact enter the active region and scatter into the lowest statistically occupiable subband energy state in the conduction band well, where it recombines with an injected hole which has thermalized to the lowest statistically occupiable energy state in the valence band well, and emits a photon at an energy $h\nu$ slightly greater than effective bandgap $E_{c1} + E_{v1} + E_g$. The design of the inner and outer clad thickness are important, as these will determine the fraction of the lasing mode intensity will be guided withing the active region/inner clad guide, and thus regenerate photons via stimulated emission.

Certain aspects of semiconductor laser performance to be examined in this thesis were emphasized in Chapter I, including: the linewidth enhancement factor, the effects of non-uniform injection in MQW heterostructure lasers, and dynamic response of semiconductor lasers during gain switching. These effects can be studied by formulating the electronic and optoelectronic properties of the quantum well laser. Therefore, in this chapter will be presented the theoretical foundation for the studies in chapters III-V.

This chapter is organized as follows. In the first section is the method of describing the bandstructure for devices examined in this thesis, the $\mathbf{k} \cdot \mathbf{p}$ method. Following this, the next section illustrates the method (and importance) of properly

Reproduced with permission of the copyright owner. Further reproduction prohibited without permission.

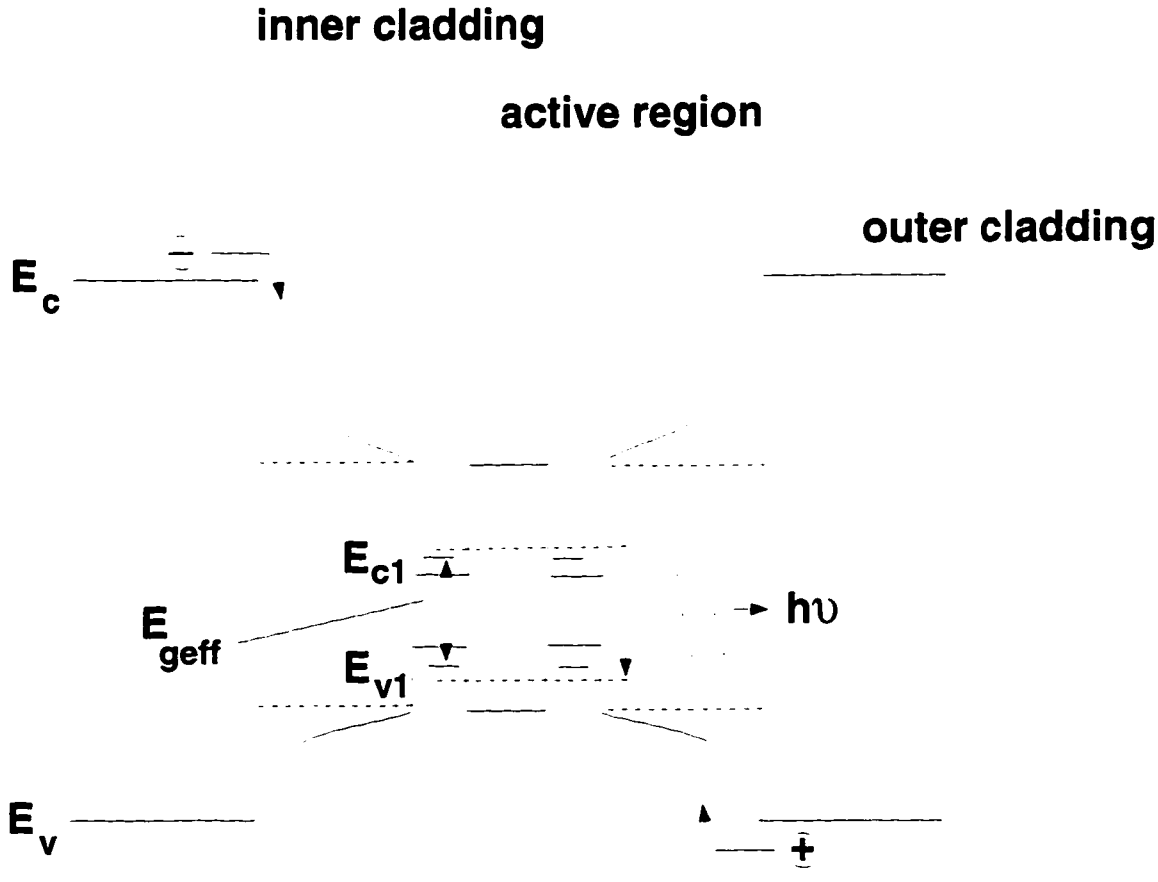


Figure 2.1: The structure of a typical high-performance laser.

Reproduced with permission of the copyright owner. Further reproduction prohibited without permission.

calculating the density of states functions. Finally, in the last section, important parameters of operation, such as material gain, spontaneous emission rate, and cavity photon density, are calculated. The importance of this is two-fold. First, the calculation of device parameters employs the formalism used in this thesis. Second, an appreciation can be developed for how methods of bandstructure engineering, such as the incorporation of biaxial strain, can be used to dramatically improve device performance.

2.2 Calculation of the Bandstructure

Many methods can be used to calculate the bandstructure, $E(\mathbf{k})$, of a heterostructure quantum well. These methods include the nonlocal pseudopotential method [18], the tight binding method (TBM) [19], and the $\mathbf{k} \cdot \mathbf{p}$ [20]–[22] method. Of these, the nonlocal pseudopotential method is considered the definitive calculation of bulk bandstructure; however, it is the most computationally expensive. The tight-binding method has the capacity to calculate the bandstructure at *any* point in the Brillouin zone, and has been applied to evaluate strained semiconductor device performance [23],[24]. The characterization of the electronic properties and gain spectra of a semiconductor laser, though, requires the bandstructure over only a small region of the Brillouin zone, near the high symmetry (Γ) point. Therefore, the perturbative $\mathbf{k} \cdot \mathbf{p}$ method is used.

2.2.1 The k · p Method

For any spatially periodic potential the electron wavefunction, Ψ, can be expressed as a Bloch function of form

$$\Psi(\mathbf{k}, \mathbf{r}) = \sum_n b_n(\mathbf{k}) \psi_n(\mathbf{k}_0, \mathbf{r}) e^{i(\mathbf{k}-\mathbf{k}_0)\cdot\mathbf{r}}, \tag{2.1}$$

Reproduced with permission of the copyright owner. Further reproduction prohibited without permission.

where $b_n(\mathbf{k})$ is a Fourier expansion coefficient and $\psi_n(\mathbf{k_0}, \mathbf{r})$ is a basis vector with band index n at momentum space position $\mathbf{k_0}$. In the subsequent discussions presented here (following [25]), $\mathbf{k_0}$ will represent a high symmetry point around which Ψ can be expanded.

In the $\mathbf{k} \cdot \mathbf{p}$ method the solution to the unperturbed Schrödinger equation is assumed to be known a-priori at some point $\mathbf{k_0}$. Schrödinger's equation is

$$H\Psi = E\Psi. \tag{2.2}$$

where E is the eigenenergy of the system. The Hamiltonian, H, is written

$$H = \frac{p^2}{2m_0} + V(\mathbf{r}). \tag{2.3}$$

Note that it is unnecessary to know what V(r) is, since it is already known what the bandstructure is at $\mathbf{k_0}$. Now, the secular equation

$$\left\| < \psi_{n'}(\mathbf{k_0}, \mathbf{r}) | H - E | \psi_n(\mathbf{k_0}, \mathbf{r}) > \right\| = 0 \tag{2.4}$$

is rewritten, after some algebra, as

$$\left\| \left\langle \left[\frac{\hbar^2}{2m_0}(\mathbf{k} - \mathbf{k_0})^2 + E_n(\mathbf{k_0}) - E \right] \delta_{n'n} + \frac{\hbar}{m_0}(\mathbf{k} - \mathbf{k_0}) \cdot \mathbf{P}_{n'n}(\mathbf{k_0}) \right\rangle \right\| = 0 \tag{2.5}$$

where $\mathbf{P}_{n'n}$ is the momentum matrix element given by

$$\mathbf{P}_{n'n} = \int \psi^*_{n'}(\mathbf{k_0}, \mathbf{r}) \mathbf{p} \psi_n(\mathbf{k_0}, \mathbf{r}) dV. \tag{2.6}$$

It is now convenient to write Eq. (2.2) in a perturbed form, as

$$\begin{aligned} (H_0 + H_1 + H_2) u_{n\mathbf{k}} &= E_{n\mathbf{k}} u_{n\mathbf{k}} \\ H_0 &= \frac{p^2}{2m_0} + V(\mathbf{r}) \\ H_1 &= \frac{\hbar}{m_0} \mathbf{k} \cdot \mathbf{p} \\ H_2 &= \frac{\hbar^2 k^2}{2m_0} \end{aligned} \tag{2.7}$$

Reproduced with permission of the copyright owner. Further reproduction prohibited without permission.

where $u_{n\mathbf{k}}$ is the central cell part of the Bloch function. For zeroth order, obviously $u_{n\mathbf{k}} = u_{n0}$, $E_{n\mathbf{k}} = E_n(0)$. Note that the point of expansion is $\mathbf{k}_0 = 0$ (i.e., at Γ).

2.2.2 Describing conduction band states

Using non-degenerate perturbation theory, the correction to the conduction band states can be found. For the first order correction,

$$u_{n\mathbf{k}} = u_{n0} + \frac{\hbar}{m_0} \sum_{n' \neq n} \mathbf{k} \cdot \frac{< n'_0|\mathbf{p}|n_0 >}{E_n(0) - E_{n'}(0)} u_{n'0}, \tag{2.8}$$

$$E_{n\mathbf{k}} = E_{n0} + \frac{\hbar}{m_0} \mathbf{k} \cdot < n'_0|p|n_0 > . \tag{2.9}$$

Some important points can be noted. From Eq. (2.8), the first order correction is seen to depend on (1) the coupling, and (2) how far interacting states are separated. By (2), we can ignore the upper conduction band states, since the denominator of the summation will be large. From (1), if there exists inversion symmetry (such as in Si), the energy correction in the first order is zero. Because of this, in a crystal like GaAs, where this inversion symmetry is not present, a small band warping occurs.

The second order correction, in the nondegenerate perturbation theory, is

$$E_n(\mathbf{k}) = E_n(0) + \sum \frac{\hbar^2 \mathbf{k}_i \cdot \mathbf{k}_j}{2m^*_{ij}} \tag{2.10}$$

where

$$\frac{m}{m^*_{ij}} = \delta_{ij} + \frac{2}{m_0} \sum_{n' \neq n} \frac{< n|p_i|n'_0 >< n_0|p_j|n'_0 >}{E_n(0) - E'_n(0)}. \tag{2.11}$$

For the conduction band, this reduces to

$$E_c(\mathbf{k}) = E_c(0) + \frac{\hbar^2 k^2}{2m^*_c}, \tag{2.12}$$

$$\frac{1}{m^*_c} = \frac{1}{m} + \frac{2p^2_{cv}}{m^2_0} \frac{1}{3} \left[\frac{2}{E_{g\Gamma}} + \frac{1}{E_{g\Gamma} + \Delta} \right], \tag{2.13}$$

where m^*_c is the conduction band effective mass, $E_{g\Gamma}$ is the direct energy gap at the Γ-point, $E_{g\Gamma} + \Delta$ is the distance to the split-off band (at $\mathbf{k} = 0$), and p^2_{cv} is the

Reproduced with permission of the copyright owner. Further reproduction prohibited without permission.

oscillator strength (given by the numerator in the summmation in Eq. (2.11). It is apparent only the heavy-hole (HH), light-hole (LH), and split-off (SO) bands are included in the calculation.

2.2.3 Describing valence band states

Using the $\mathbf{k} \cdot \mathbf{p}$ theory the valence band states can also be described. Unlike the conduction band case, however, degenerate perturbation theory must be applied. Ignoring the conduction band states (assuming $\frac{1}{E_g}$ is much less than the HH-LH interaction) leaving a 6 $\times$ 6 Hamiltonian. Furthermore, it is a good assumption in most semiconductors to ignore the contribution of the SO band to the states near the bandedge, which results in a 4 $\times$ 4 Hamiltonian. One treatment of this type yields what is known as the Kohn-Luttinger (KL) 4 $\times$ 4 Hamiltonian:

$$-\begin{bmatrix} H_{hh} & b & c & 0 \\ b^\dagger & H_{lh} & 0 & c \\ c^\dagger & 0 & H_{lh} & -b \\ 0 & c^\dagger & -b^\dagger & H_{hh} \end{bmatrix} \begin{bmatrix} g_m^{3/2,3/2}(\mathbf{k},z) \\ g_m^{3/2,1/2}(\mathbf{k},z) \\ g_m^{3/2,-1/2}(\mathbf{k},z) \\ g_m^{3/2,-3/2}(\mathbf{k},z) \end{bmatrix} = E_m(\mathbf{k}) \begin{bmatrix} g_m^{3/2,3/2}(\mathbf{k},z) \\ g_m^{3/2,1/2}(\mathbf{k},z) \\ g_m^{3/2,-1/2}(\mathbf{k},z) \\ g_m^{3/2,-3/2}(\mathbf{k},z) \end{bmatrix}$$

where the matrix entries are given by

$$H_{hh} = \hbar^2\left[(k_x^2+k_y^2)(\gamma_1+\gamma_2) - (\gamma_1-2\gamma_2)\frac{\partial^2}{\partial z^2}\right] - V^h(z) \tag{2.14}$$

$$H_{lh} = \hbar^2\left[(k_x^2+k_y^2)(\gamma_1-\gamma_2) - (\gamma_1+2\gamma_2)\frac{\partial^2}{\partial z^2}\right] - V^h(z) \tag{2.15}$$

$$c = \frac{\sqrt{3}\hbar^2}{2m_0}[\gamma_2(k_x^2+k_y^2-2i\gamma_3 k_x k_y] \tag{2.16}$$

$$b = -\frac{\sqrt{3}\hbar^2}{m_0}(k_x - ik_y)\gamma_3\frac{\partial}{\partial z}. \tag{2.17}$$

Here V_h is the potential profile for holes, z is the growth direction, $g_m^{3/2,3/2}(\mathbf{k},z)$ and $g_m^{3/2,-3/2}(\mathbf{k},z)$ represent the are envelope functions for the heavy holes (spin up and

Reproduced with permission of the copyright owner. Further reproduction prohibited without permission.

spin down), $g_m^{3/2,1/2}(\mathbf{k}, z)$,$g_m^{3/2,-1/2}(\mathbf{k}, z)$ are the envelope functions for the light holes. $\frac{\partial}{\partial z}$ is the differential operator on the hole wavefunctions (in place of k_z), and γ_1, γ_2, γ_3 are fitting parameters known as the Kohn-Luttinger parameters.

2.2.4 Incorporating biaxial strain

The use of biaxial strain changes the electronic properties of the materials and consequently can improve the performance characteristics of semiconductor lasers. In this section the incorporation of strain into the KL Hamiltonian is described. Following this, sample bandstructure calculations will be presented. Here it is assumed no dislocations occur due to strain, and the biaxial strain is within the epilayer, with growth along [001].

In the pseudomorphic regime

$$\epsilon_{||} = \frac{a_s}{a_L} - 1$$
$$\epsilon_{\perp} = \frac{-\epsilon_{||}}{\sigma} \tag{2.18}$$

where a_s is the substrate lattice constant, a_L is the epilayer lattice constant, $\epsilon_{||}$ is the amount of biaxial strain, $\epsilon_{\perp}$ is the amount of uniaxial strain, and σ is the Poisson ratio. Through deformation potential theory it can be shown that the effect of strain is essentially a perturbation to the Hamiltonian matrix described before.

For the conduction band at Γ for a direct gap semiconductor, the shift in the conduction band energy δE_c is [25]

$$H_\epsilon = \delta E_c = 2\epsilon_{||}\Xi^{(000)}(1 - \frac{c_{12}}{c_{11}}). \tag{2.19}$$

Here H_ϵ represents the strain perturbation Hamiltonian, $\Xi^{(000)}$ is the dilation defomation potential for the conduction band (000) valley, and c_{11} and c_{12} are elements of the stress tensor.

Reproduced with permission of the copyright owner. Further reproduction prohibited without permission.

The effects of strain are more complicated at the valence bandedge due to the degenerate nature of the LH and HH states. The resulting perturbation matrix has only diagonal components:

$$H^{\epsilon}_{hh} = \left[2a\left(\frac{c_{11}-c_{12}}{c_{11}}\right) + \left(\frac{c_{11}+2c_{12}}{c_{11}}\right)\right]\epsilon \tag{2.20}$$

$$H^{\epsilon}_{lh} = \left[2a\left(\frac{c_{11}-c_{12}}{c_{11}}\right) - b\left(\frac{c_{11}+2c_{12}}{c_{11}}\right)\right]\epsilon \tag{2.21}$$

where H^{ϵ}_{hh} and H^{ϵ}_{lh} are the HH and LH matrix elements of the Hamiltonian, $\epsilon = \epsilon_{||}$, and a and b are valence band deformation potentials. The difference $\delta = H^{\epsilon}_{hh} - H^{\epsilon}_{lh}$ is the splitting between the heavy and light hole states due to the strain.

As stated in the preceding discussion, the growth direction here is [001]. A question may arise: why not grow along other directions? In the GaAs-based system, along [001] only one monolayer of all Ga or As atoms is seen. Therefore, there exists a double bond configuration between these planes. Along [110] or [1$\bar{1}$0] single bonds exist between planes. Because the wafer is weaker along these directions, cleaving preferentially occurs along these planes. Thus, the [110] planes are unsuitable.

From electronic considerations, the [111] plane appears to be an attractive candidate. Due to anisotropy, hole masses will vary with direction; along [111], the hole mass is smallest (in a QW) since the density of states is small. In addition, growing along [111] yields distortion, which implies off-diagonal terms in the strain Hamiltonian can be non-zero. Therefore, a large built-in electric field can be obtained from displaced anions and cations forming dipoles. So far it has not been possible to grow high quality quantum wells along [111] due to the asymmetric bonding along this direction (3 bonds up, 1 down or 3 bonds down, 1 up for [111] versus 2 bonds up, 2 down along [001]).

In Figs. 2.2 - 2.5 are shown the calculated valence bandstructures, using the $\mathbf{k} \cdot \mathbf{p}$

Reproduced with permission of the copyright owner. Further reproduction prohibited without permission.

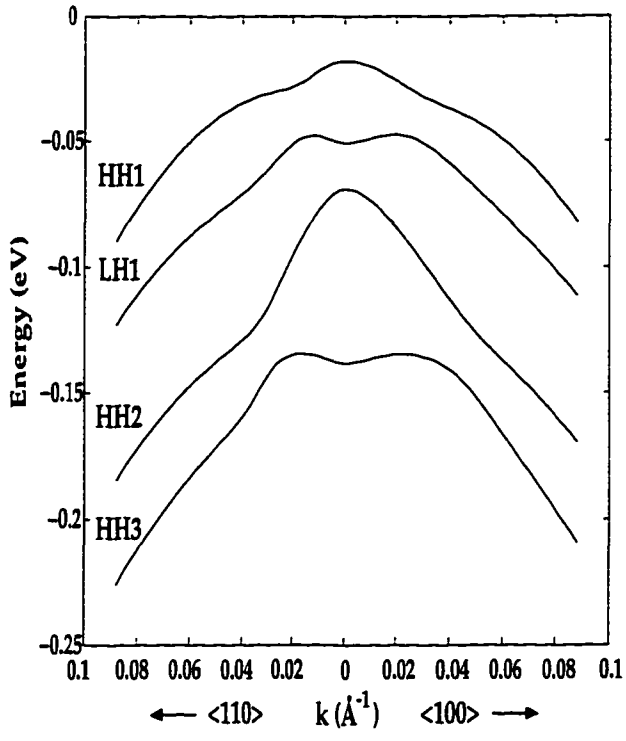


Figure 2.2: Valence bandstructure along the [100] and [110] directions in a 50 ÅGaAs/$Al_{0.3}Ga_{0.7}As$ (on GaAs) quantum well.

method, for $In_xGa_{1-x}As/Al_{0.3}Ga_{0.7}As$ quantum wells, with $x \subset \{0\%, 10\%, 20\%, 30\%\}$. The effect of the *compressive* biaxial strain is clear: the HH states are raised in energy above the LH states. As will be discussed in Section 2.4, TE-polarized light couples 3 times as strongly to HH states as to LH states; thus, strain will play an important role in selecting the output light polarization.

2.3 Density of States Calculation

The electronic density of states, $D(E)$, affects many laser properties; the most important being its influence on the carrier density necessary for inversion. . From statistical physics $D(E)$ is defined as the number of energy states, $N(E)$, between E and $E + dE$. Since both N and E can both be conveniently expressed in terms of

Reproduced with permission of the copyright owner. Further reproduction prohibited without permission.

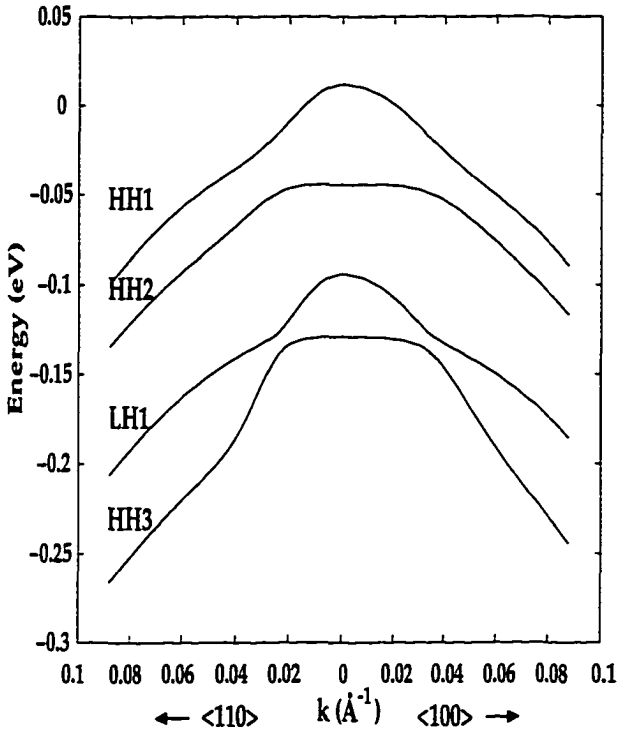


Figure 2.3: Valence bandstructure along the [100] and [110] directions in a 50 Å$In_{0.1}Ga_{0.9}As/Al_{0.3}Ga_{0.7}As$ (on GaAs) quantum well.

Reproduced with permission of the copyright owner. Further reproduction prohibited without permission.

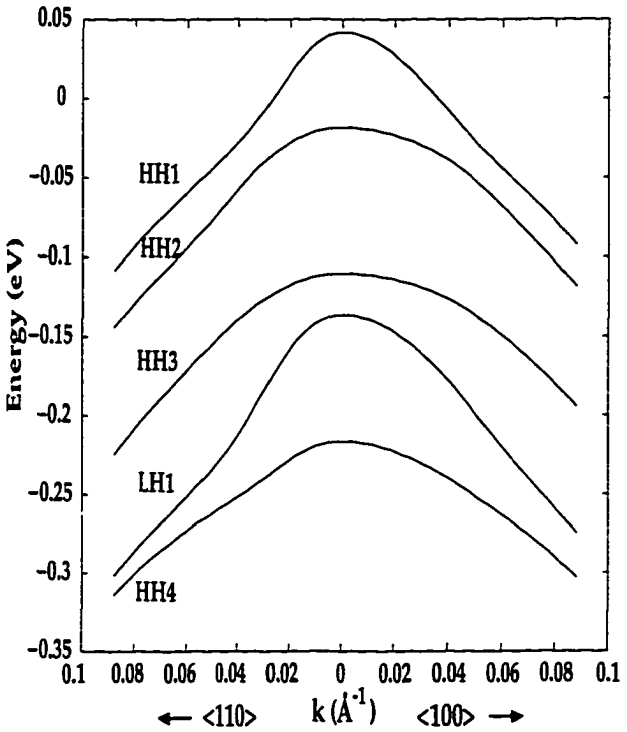


Figure 2.4: Valence bandstructure along the [100] and [110] directions in a 50 Å$In_{0.2}Ga_{0.8}As/Al_{0.3}Ga_{0.7}As$ (on GaAs) quantum well.

Reproduced with permission of the copyright owner. Further reproduction prohibited without permission.

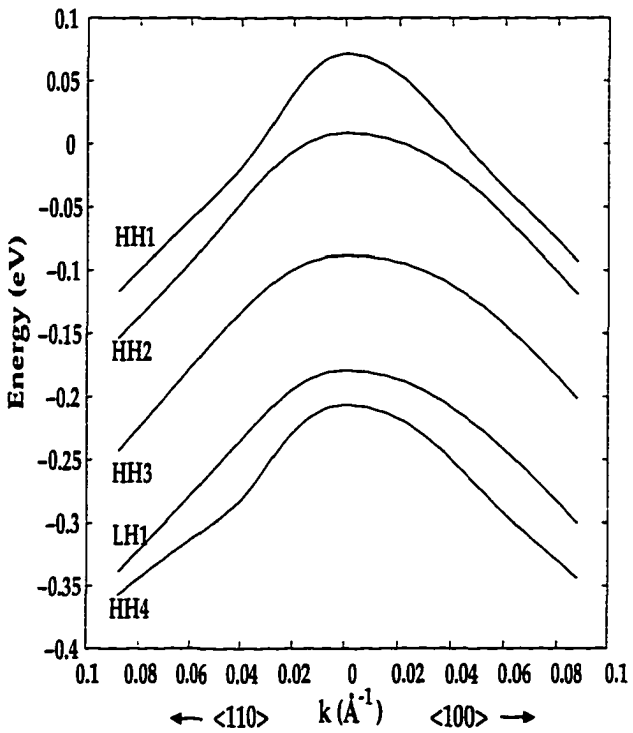


Figure 2.5: Valence bandstructure along the [100] and [110] directions in a 50 Å$In_{0.3}Ga_{0.7}As/Al_{0.3}Ga_{0.7}As$ (on GaAs) quantum well.

Reproduced with permission of the copyright owner. Further reproduction prohibited without permission.

the the wavevector k,

$$D(E) = \frac{dN(k)/dk}{dE(k)/dk}. \tag{2.22}$$

The number of particles, $n(E)$, between E and $E + dE$ is

$$n(E) = D(E)f(E)dE \tag{2.23}$$

where $f(E)$ is the probability of a particle occupying energy state E at temperature T. By integrating over all energy states the total number of particles can be found. For fermions $f(E)$ is the Fermi distribution function.

In a quantum well laser the interest lies in seeing how the electron and hole distribution functions, $f_e(E)$, and $f_h(E)$, change with the injected number of carriers into quantum well. The effective mass approximation facilitates the use of a paraboloid to describe the conduction band around k=0. For the 2D electron gas inside the well, the density of states, $D_e(E)$, is

$$D_e(E_n) = \frac{m^*}{\pi\hbar^2 W}, \tag{2.24}$$

where the subscript n denotes the n^{th} conduction band well subband, and W is the width of the quantum well. The 2D density of states for a parabolic band is independent of energy. For the valence band it is necessary to numerically calculate the density of states to accurately include the effect of state-mixing in the valence bandstructure. The density of states for the valence band well subbands, $D_h(E)$, by Eq. (2.22), is given in a discrete computational form as,

$$D_h(E_m) = \frac{(k_2 + k_1)/4\pi}{(E(k_2) - E(k_1))/(k_2 - k_1)} \tag{2.25}$$

where

$$k_1 = \sqrt{(\mathrm{k}_x - \delta\mathrm{k}_x)^2 + (\mathrm{k}_y - \delta\mathrm{k}_y)^2} \tag{2.26}$$

Reproduced with permission of the copyright owner. Further reproduction prohibited without permission.

$$k_2 = \sqrt{(\mathbf{k}_x + \delta\mathbf{k}_x)^2 + (\mathbf{k}_y + \delta\mathbf{k}_y)^2}. \tag{2.27}$$

Here $\mathbf{k}_x$ and $\mathbf{k}_y$ are wavevectors, $\delta\mathbf{k}_x$ and $\delta\mathbf{k}_y$ effect a small change in the magnitude vectors k_1 and k_2 to facilitate computation of the hole density of states at $(\mathbf{k}_x.\mathbf{k}_y)$ for the m^{th} valence band well subband. The electron and hole distribution functions can then be calculated through their chemical potentials (quasi-Fermi levels), E_{fn} and E_{fp}, iteratively solved from

$$n = \sum_n \int_{E_{en}}^{\infty} D_e(E_n) \frac{dE}{1 + exp(\frac{E - E_{fn}}{k_B T})} \tag{2.28}$$

$$p = \sum_m \int_{-\infty}^{E_{hm}} D_h(E_m) \frac{dE}{1 + exp(\frac{E_{fp} - E}{k_B T})} \tag{2.29}$$

where N and P are the injected number of electrons and holes, with contributions summed over all m and n valence and conduction subbands.

Figure 2.6 shows the calculated hole density of states functions for the quantum well structures considered earlier, $x \subset \{0\%, 10\%, 20\%, 30\%\}$. The density of states functions are not constant between subband energies due to changes in the curvature of the bandstructure, as seen in Figs. 2.2 - 2.5. The step-like discontinuities, evident in the figure for each curve, result from the additional states available once the next subband is reached. In addition, once the subband is outside of the well, the density of states begin to take on 3-dimensional (bulk) characteristics; these have been included in the calculation. However, these states at these energies are, by the Fermi distribution function, almost completely unoccupied and thus will have no effect on the quasi-Fermi level (for the carrier densities considered in these studies).

2.4 Calculation of Laser Characteristics

After calculating the bandstructure, density of states, and the carrier distribution functions, it is possible to obtain laser operation characteristics, such as threshold

Reproduced with permission of the copyright owner. Further reproduction prohibited without permission.

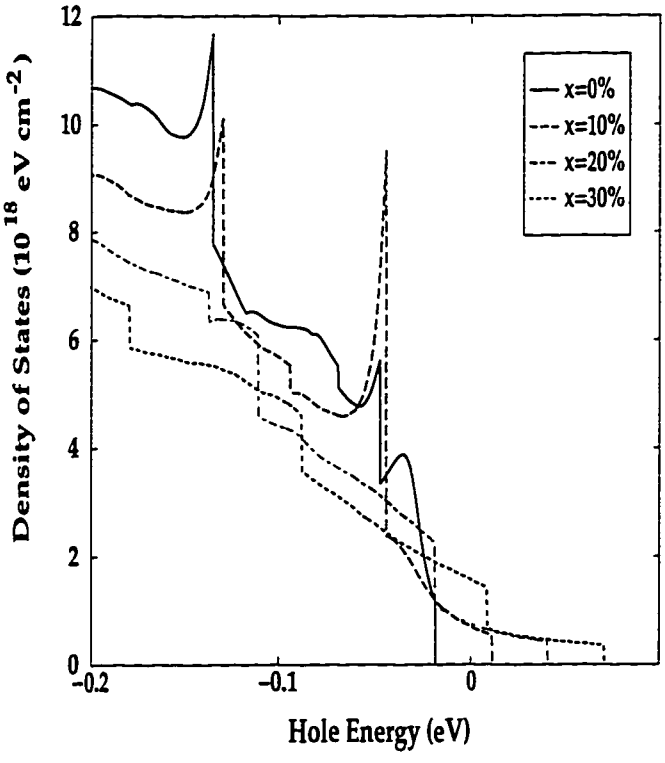


Figure 2.6: The hole density of states functions for a 50 Å$In_xGa_{1-x}/Al_{0.3}Ga_{0.7}As$ (on GaAs) quantum well.

Reproduced with permission of the copyright owner. Further reproduction prohibited without permission.

current and photon output. In Section 2.2 stationary perturbation theory was used in the $\mathbf{k}\cdot\mathbf{p}$ method to describe the bandstructure. In contrast, the method for examining electron-photon interactions is time-dependent perturbation theory, resulting in a relation known as Fermi's Golden Rule, or,

$$R = \frac{dP}{dt'} = \frac{2\pi}{\hbar}|H^1_{n'n}|^2 D(E), \tag{2.30}$$

where P is the transition probability from state n to state n'.

2.4.1 Calculation of Gain and Spontaneous Emission Rates

Using Fermi's Golden rule, the material gain and spontaneous emission rates can be obtained (using the proper gauge operators in the matrix element). With the appropriate basis being provided in the last section, the final results will be presented here.

The subband-to-subband optical gain is given (in mks units) by [25]

$$\begin{aligned} g_{nm}(n,p,E) &= \frac{\pi e^2\hbar}{\epsilon_0 n_0 c m_0^2 W E}\frac{1}{(2\pi)^2}\int d\mathbf{k}\sum_\sigma |\hat{\epsilon}\times\mathbf{P}^\sigma_{nm}(\mathbf{k})|^2 \\ &\quad\times\delta(E^e_n(\mathbf{k}) - E^h_m(\mathbf{k}) - E)\cdot[f^e(E^e_n(\mathbf{k})) + f^h(E^h_m(\mathbf{k})) - 1] \end{aligned} \tag{2.31}$$

Likewise, the spontaneous emission rate (in mks units) can be calculated from [25]

$$\begin{aligned} R_{sp}(n,p) &= \int dE \frac{4e^2 n_0 E}{3m_0^2 c^3\hbar^2}\frac{1}{(2\pi)^2}\sum_{nm}\int d\mathbf{k}\sum_\sigma |\mathbf{P}^\sigma_{nm}(\mathbf{k})|^2 \\ &\quad\times\delta(E^e_n(\mathbf{k}) - E^h_m(\mathbf{k}) - E)\cdot[f^e(E^e_n(\mathbf{k}))][f^h(E^h_m(\mathbf{k}))]. \end{aligned} \tag{2.32}$$

Here $g_{nm}(n,p,E)$ is the optical gain at photon energy E in the quantum well with electron density n and hole density p from the n^{th} electron subband and m^{th} hole subband, $R_{sp}(n,p)$ is the spontaneous emission rate from the well, e is the electron charge, n_0 is the refractive index of the active region, c is the vacuum speed of light, m_0 is the free electron mass, W is the active region width, $\hat{\epsilon}$ is the polarization of

Reproduced with permission of the copyright owner. Further reproduction prohibited without permission.

the light, $\mathbf{P}^{\sigma}_{nm}$ is the optical matrix element, and $f^e(E^e_n(\mathbf{k}))$ and $f^h(E^h_m(\mathbf{k}))$ are the distribution functions for electrons and holes in the n^{th} and m^{th} subbands with momentum $\mathbf{k}$ and energies $E^e_n(\mathbf{k})$ and $E^h_m(\mathbf{k})$, respectively. The optical matrix element is given as [25]

$$\mathbf{P}^{\sigma}_{nm}(\mathbf{k}) = \sum_{\nu} \int f^{*}_{n}(\mathbf{k}, z) g^{\nu}_{m}(\mathbf{k}, z) dz < U^e_{\sigma} | \mathbf{p} | U^h_{\nu} > . \tag{2.33}$$

Here the momentum matrix elements $< U^e_{\sigma}|\mathbf{p}|U^h_{\nu} >$ are evaluated by using the form of the basis states $|U>$

$$|U^e_{\sigma}> = |s> \sigma \tag{2.34}$$

$$|U^h_{\frac{3}{2}}> = \frac{1}{\sqrt{2}}(|x> + i|y>) \uparrow \tag{2.35}$$

$$|U^h_{\frac{1}{2}}> = \frac{i}{\sqrt{6}}[(|x> + i|y>) \downarrow -2|z> \uparrow] \tag{2.36}$$

$$|U^h_{\frac{-1}{2}}> = \frac{1}{\sqrt{6}}[(|x> - i|y>) \uparrow +2|z> \downarrow] \tag{2.37}$$

$$|U^h_{\frac{-3}{2}}> = \frac{i}{\sqrt{2}}(|x> - i|y>) \downarrow \tag{2.38}$$

along with the orthonormality of the spin states $\uparrow$ and $\downarrow$ and the symmetry property that $< s|p_x|x > = < s|p_y|y > = < s|p_z|z >$ and that all other matrix elements vanish. Note that $\hat{x}$-polarized couples 3 times as strongly to the HH states as $\hat{z}$-polarized light and that the LH states couple exclusively to $\hat{z}$-polarized light.

To get the total material gain $g(E)$, a summation is done over all subbands n, m, and a convolution is performed with a Lorentzian broadening function, $\Delta(E)$, to account for broadening. The result is [52]

$$g(n, p, E) = \int dE' \sum_{nm} g_{nm}(n, p, E') \Delta(E - E'). \tag{2.39}$$

.

In Fig.(2.7) the peak material gain versus carrier density has been plotted for the four compositions of $In_xGa_{1-x}As$ previously discussed. The effect of strain is

Reproduced with permission of the copyright owner. Further reproduction prohibited without permission.

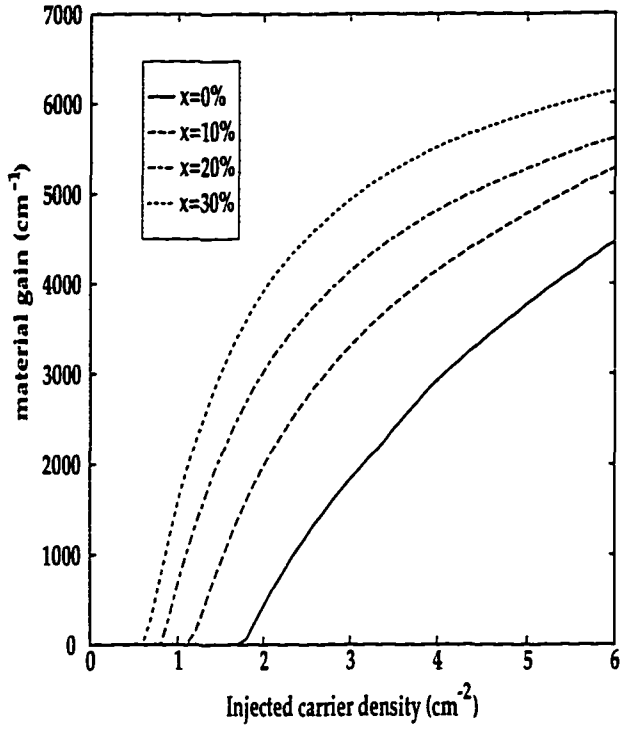


Figure 2.7: Peak TE mode material gain versus injected carrier density for a 50 Å$In_xGa_{1-x}/Al_{0.3}Ga_{0.7}As$ (on GaAs) quantum well.

clearly evident, as the gain has monotonically increased with percent strain, due to the strong coupling of TE light with the HH states. For the same reason, the spontaneous emission rate increases for increasing strain. This is plotted in Fig. 2.7

2.4.2 Current and Photon Density Calculations

Using the formalism presented, the laser operating characteristics can be examined. In this section I will describe how the current and photon densities in steady state can be calculated via the rate equations. These equations will be extensively utilized in Chapters III-V.

The interactions between the carrier concentration and the photon population in the active region of the laser can be expressed by the coupled multimode rate

Reproduced with permission of the copyright owner. Further reproduction prohibited without permission.

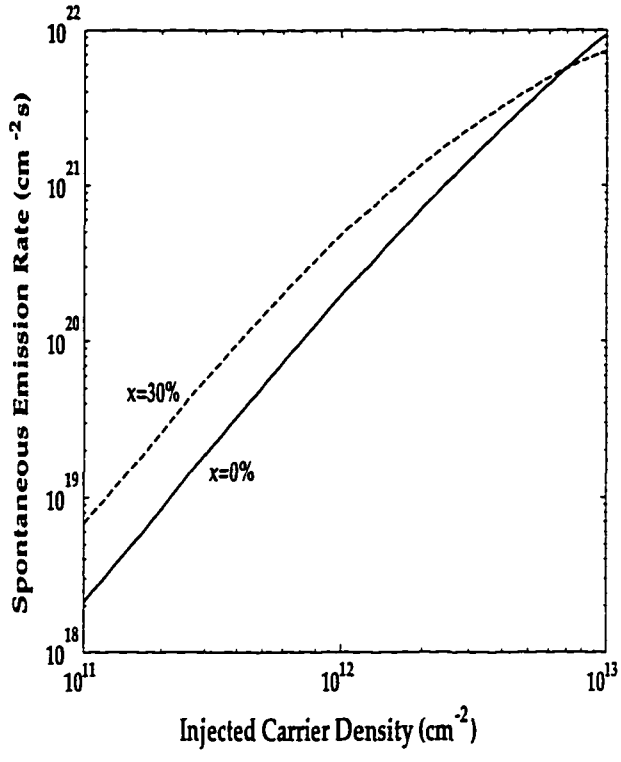


Figure 2.8: Spontaneous emission rate versus injected carrier density for 50 Å$In_xGa_{1-x}/Al_{0.3}Ga_{0.7}As$ (on GaAs) quantum well.

Reproduced with permission of the copyright owner. Further reproduction prohibited without permission.

equations [53]

$$\frac{dS_{\hat{\epsilon},m}}{dt} = [N\Gamma g(n, E_m) - \alpha_c](\frac{c}{n_g})S_{\hat{\epsilon},m} + \beta N R_{sp}(n) \tag{2.40}$$

$$\frac{dn}{dt} = \frac{J}{eN} - R_{sp}(n) - (\frac{c}{n_g})\sum_{\hat{\epsilon},m} \Gamma g(n, E_m)S_{\hat{\epsilon},m} \tag{2.41}$$

where $S_{\hat{\epsilon},m}$ is the photon density per unit area in the cavity for the m^{th} longitudinal mode propagating with polarization ϵ and energy E_m, n is the carrier density, $\Gamma N g(n, E_m)$ is the net gain experienced in the active region with confinement factor Γ with N wells, α_c is the cavity loss, n_g is the group index of refraction in the cavity, β is the spontaneous emission factor, $R_{sp}(n)$ is the spontaneous emission rate, and J is the injected radiative current density. The index m includes all longitudinal modes which show gain at threshold, given by

$$\lambda_m = \frac{2n_0 L}{m}, \tag{2.42}$$

while $\hat{\epsilon}$ denotes either the TE or TM mode.

Setting the time derivatives of Eqs.(55) and (56) to zero yields the steady-state equations

$$S_{\hat{\epsilon},m} = \frac{\beta N R_{sp}(n)}{\frac{c}{n_g}[\alpha_c - N\Gamma g(n, E_m)]}, \tag{2.43}$$

$$\frac{J}{e} = N R_{sp}(n)\Big\{1 + \sum_{\hat{\epsilon},m} \frac{\beta N\Gamma g(n, E_m)}{[\alpha_c - N\Gamma g(n, E_m)]}\Big\}. \tag{2.44}$$

Here it is assumed that 1) the photon and carrier distributions are spatially uniform, 2) the refractive index is constant as a function of space, time, polarization, and wavelength, 3) the optical confinement factor Γ and spontaneous emission factor β are constant per well, and 4) gain compression is ignored. (In chapter V, however, gain compression will be considered.)

In Fig. (2.9) shows calculations of cavity photon density versus injected carrier density for the GaAs-based compositions considered in this chapter, assuming $\alpha_c =$

Reproduced with permission of the copyright owner. Further reproduction prohibited without permission.

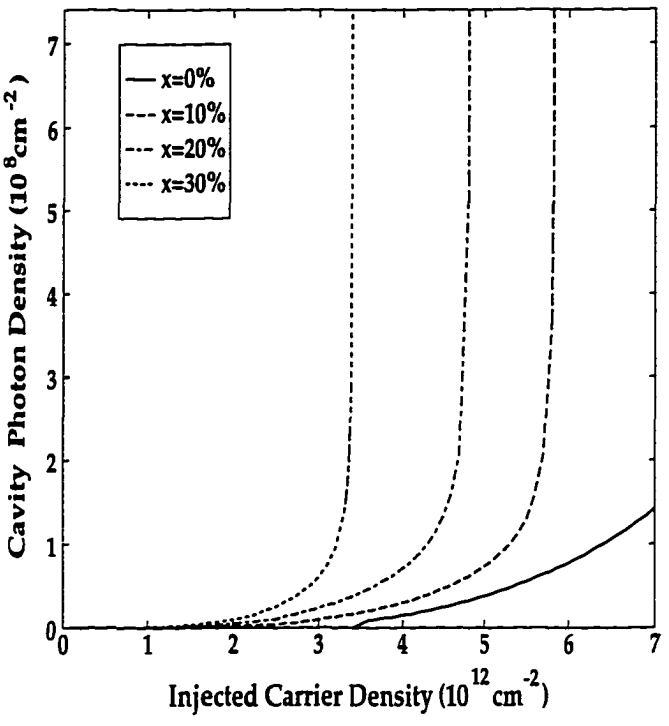


Figure 2.9: Total photon density versus injected carrier density for 50 Å$In_xGa_{1-x}/Al_{0.3}Ga_{0.7}As$ (on GaAs) quantum well.

65cm^{-1}, $L = 200\mu$m, $\Gamma = 0.0125$, and $N = 1$, which are typical values for loss and Γ for fabricated devices. It is seen that as the compressive strain increases, the threshold carrier density decreases. This decrease in threshold carrier density with strain, offsets the corresponding increase in $R_{sp}(n_{th})$ and, by Eq. (2.44), results in a lower threshold current density. In addition, the sharp rise of photon density at threshold shows the dominance of the stimulated emission process in this regime.

Reproduced with permission of the copyright owner. Further reproduction prohibited without permission.

CHAPTER III

STRAIN AND TEMPERATURE DEPENDENCE OF THE LINEWIDTH ENHANCEMENT FACTOR

3.1 Motivation

As stated in the introductory chapter, it is desirable to mimimize the linewidth enhancement factor, α, due to reductions in spectral chirping width, spectral linewidth, and waveform distortion. The use of strain provides many benefits in lasers, such as improved material gain and differential gain. The linewidth enhancement factor, which is proportional to changes in the active medium refractive index caused by fluctuations in the carrier density, can be related to the gain and differential gain of a laser through the Kramers-Kronig relations. Thus the study of the dependence of α on strain has elicited interest.

It is well-known that the reduction in the laser operating temperature also effects improvements in parameters, including gain, differential gain, and small-signal bandwidth. It has then been suggested that a reduction in temperature may be of use in coherent systems in order to take advantage of these improved parameters [62]. Although studies have been done examining the effects of strain on α, it has yet to be seen whether the temperature dependence of α is of concern in InP-based

Reproduced with permission of the copyright owner. Further reproduction prohibited without permission.

devices, which generally have a lower characteristic temperature.

The chapter is organized as follows. In the first section, a theoretical background for α is given, followed by calculation of the strain and temperature dependence of α for $In_xGa_{1-x}As/GaAs$ and $In_{1-x}Ga_xAs_yP_{1-y}/InP$ structures. These results serve as a framework to examine experimental measurements of α on MQW $In_xGa_{1-x}As/InP$ lasers.

3.2 Theoretical Calculations

3.2.1 Background

The linewidth enhancement factor determines the relation of the AM to FM modulation indices [27] as well as the degree to which the spectral purity is degraded through coupling [28]-[31]. The ratio of the power spectral density (from carrier induced fluctuations) and FM noise from spontaneous emission, is α^2. A discussion of the physics and derivation of α is done in Appendix A, based on the classic paper by Henry [14]. Although the derivation is an adiabatic one, it agrees with the less-intuitive but more rigorous and general quantum mechanical derivation by Lax [63].

The linewidth enhancement factor has two contributing factors: 1) changes in the active medium refractive index from changes in the gain of the medium, known as *anomalous* dispersion, and 2) changes in the active medium refractive index due to carrier movement caused by the optical field, known as free carrier or *plasma* dispersion [32].

The anomalous dispersion term can be written as [35]

$$\alpha_a = \frac{d\chi_R}{d\chi_I} \tag{3.1}$$

where

$$\frac{d\chi_I(N, E_l}{dN} = \int_0^\infty dE \frac{dg(N,E)}{dN} \frac{\hbar/T_2}{(E - E_l)^2 + (\hbar/T_2)^2}, \tag{3.2}$$

Reproduced with permission of the copyright owner. Further reproduction prohibited without permission.

and, through the Kramers-Kronig relations,

$$\frac{d\chi_R(N,E_l}{dN} = \int_0^\infty dE \frac{dg(N,E)}{dN} \frac{(E-E_l}{(E-E_l)^2+(\hbar/T_2)^2}, \tag{3.3}$$

where χ_R and χ_I are the real and imaginary parts of the complex susceptibility, E_l is the lasing photon energy, N is the radiative carrier density, and a Lorentzian function has been introduced to include collision broadening, whose time is given as T_2. The contribution to α from plasma dispersion, α_p, is

$$\alpha_p(\lambda_l) = \frac{q^2\lambda_l}{2\pi\epsilon_0 nc^2 m_r^* m_0}\left(\frac{dg(N,\lambda_l)}{dN}\right)^{-1}, \tag{3.4}$$

where λ_l is the lasing wavelength, n is the refractive index, and $m_r^* m_0$ is the reduced mass of the electron-hole pair (evaluated from the density of states). Then,

$$\alpha(\lambda_l) = \alpha_a(\lambda_1) + \alpha_p(\lambda_l). \tag{3.5}$$

3.2.2 Calculations

In this section linewidth enhancement factor calculations are made using the equations given for α and the formalism set in Chapter II, on typical α $In_xGa_{1-x}As/GaAs$ and $In_{1-x}Ga_xAs_yP_{1-y}/InP$ quantum well structures. Calculations on the structures serve to establish the dependence of α versus both strain and temperature.

3.2.2.1 $In_xGa_{1-x}As/GaAs$ calculations

In this section effects of strain and temperature are considered for a 50 Å $In_xGa_{1-x}As$ QW with $Al_{0.3}Ga_{0.7}As$ barriers, assuming the substrate is GaAs. The various parameters used in the calculations are obtained using the virtual crystal approximation [25], i.e. a ternary interpolation of the binary parameters, and are listed in Table 3.1. The parameters in Table 3.1 are assumed in this calculation to be constant with temperature, while the bulk energy bandgaps of the various materials are assumed

Reproduced with permission of the copyright owner. Further reproduction prohibited without permission.

parameter	InAs	GaAs	InP	GaP
a_0 [25]	6.0583	5.6532	5.8687	5.4505
m_c [26]	0.023	0.067	0.080	0.135
γ_1 [51]	19.67	6.85	6.28	4.20
γ_2 [51]	8.37	2.10	2.90	0.98
γ_3 [51]	9.29	2.90	2.76	1.66
$\frac{p_{cv}^2}{2m_0}$ [51]	22.2	28.8	20.4	22.2

Table 3.1: Parameters used in the calculations in this chapter. The listed values are for T=300K.

to change by the form [25]

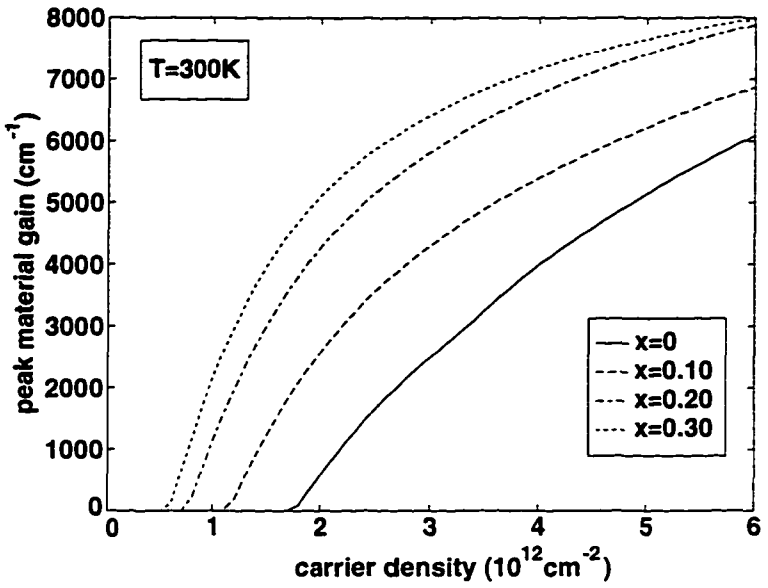
$$E_g = E_{g0} - \frac{aT}{b + T^2} \tag{3.6}$$

where E_{g0} and E_g represent the bandgap of each binary at 0 K and 300 K respectively. Although the approximation is not entirely correct, the changes in parameters of Table 3.1 are much less significant in the calculation than the change in the gain spectrum resulting from the sharpening of the Fermi occupation probability function at low temperatures.

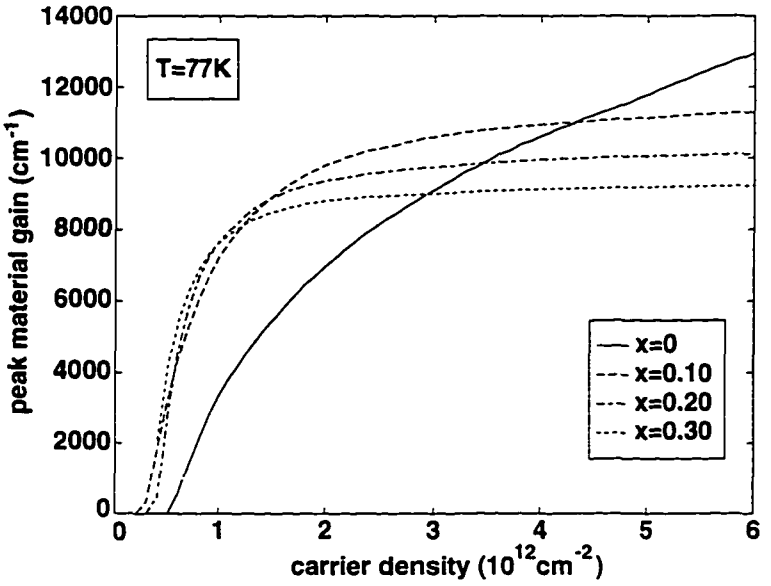
In Fig. 3.1 the peak gain $g_{max}(N)$ versus radiative carrier density N is shown, at both T=300K (Fig. 3.1(a)) and T=77K (Fig. 3.1(b)). Since the electron and hole Fermi occupational probability functions f_n and f_p maximize at lower carrier densities with a decrease in temperature, it is clear from Fig. 3.1 that the unstrained well has the largest overlap integral (Eq. (2.33)).

Figure 3.2 shows plots of α versus g_{max}, where g_{max} is the peak material gain at a particular value of N. It is clear from both Fig. 3.2(a) and Fig. 3.2(b) that for typical values of threshold gain/well in a MQW laser, that α decreases with strain, due to the increase of $\frac{dg}{dN}$ with strain. The reduction in α at 77K serves to establish

Reproduced with permission of the copyright owner. Further reproduction prohibited without permission.



(a)



(b)

Figure 3.1: Peak material gain versus radiative carrier density for a 50 Å $In_xGa_{1-x}As$ well (on GaAs) at (a) 300K and (b) 77K.

Reproduced with permission of the copyright owner. Further reproduction prohibited without permission.

the dependence of α on strain and temperature.

In Fig. 3.2(c) is plotted α versus g_{max} for $x = 10\%$. The anomalous dispersion is seen to steadily decrease as gain increases. This is due to the dependence of $\frac{d\chi_R}{dN}$ on $E - E_l$; as the carrier density increases E_l shifts towards the peak of the differential gain spectrum, and therefore α_a decreases. The plasma dispersion contribution steadily increases with g_{max}, since in Eq. (3.4) it is proportional to $\left(\frac{dg}{dN}\right)^{-1}$, which decreases as N increases.

3.2.2.2 $In_{1-x}Ga_xAs_yP_{1-y}$/InP calculations

In this section the effects of compressive and tensile strain on an 80 Å $In_xGa_{1-x}As_yP_{1-y}$ well (λ=1.55 μm) with unstrained $In_xGa_{1-x}As_yP_{1-y}$ barriers (λ=1.2 μm), on InP. Parameters Q(x,y) for the calculations are obtained using the quarternary interpolation [54]

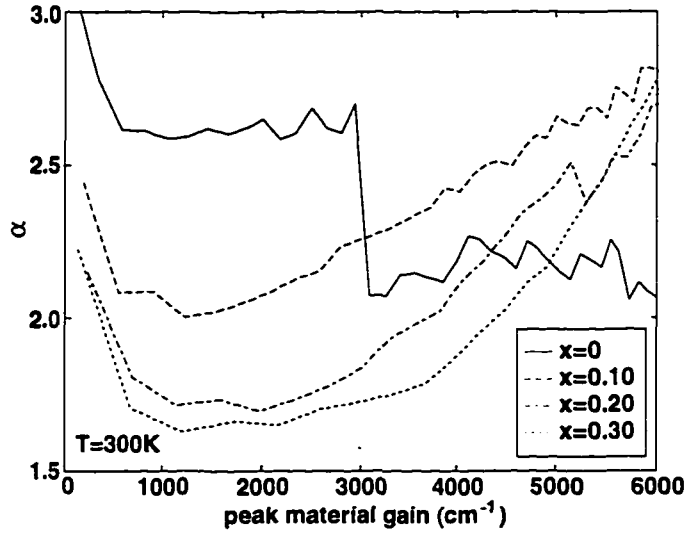
$$Q(x,y) = \frac{x(1-x)[(1-y)t_{12}(x) + yt_{43}(x)] + y(1-y)[(1-x)t_{14}(y) + xt_{23}(y)]}{x(1-x) + y(1-y)}, \tag{3.7}$$

where t_{ij} material parameter for the ternary alloy formed by binaries i and j, while the fractions x and y were obtained by interpolation using energy bandgap contours (see [59]) at $T = 300K$.

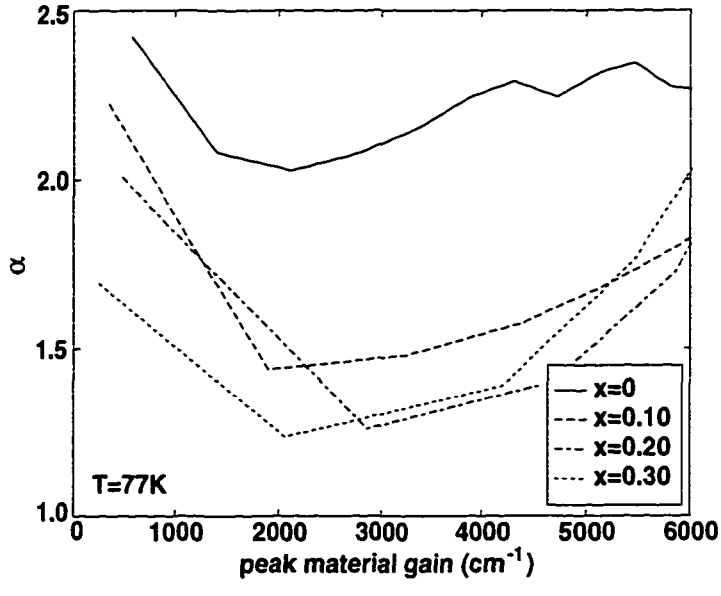
Figure 3.3 shows calculated peak gain curves for compressive strain (Fig. 3.3(a)) and tensile strain (Fig. 3.3(b)). (Note, in Fig. 3.3(b), for the ϵ=0% (no strain) and the ϵ=0.25% cases, the TE-mode still slightly dominates, and it is the TE-mode peak gain curves that have been plotted here.) It is seen that peak gain increases as either tensile or compressive strain is applied, and is larger for the tensilely-strained case.

Figure 3.4 shows the variation in linewidth enhancement factor for compressive or tensile strain. As in the GaAs-based system, α decreases with increasing strain

Reproduced with permission of the copyright owner. Further reproduction prohibited without permission.



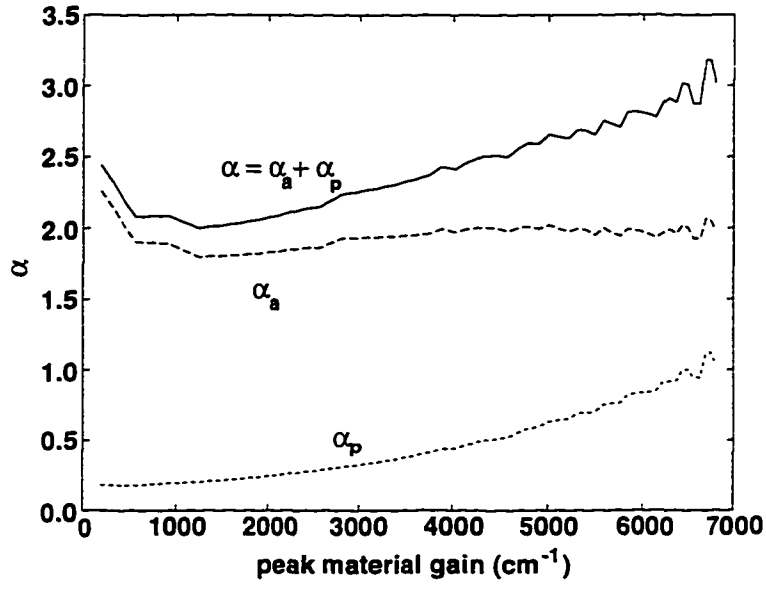
(a)



(b)

Figure 3.2: Linewidth enhancement factor versus radiative carrier density for a 50 Å$In_xGa_{1-x}As$ well (on GaAs) system at (a) 300K and (b) 77K.

Reproduced with permission of the copyright owner. Further reproduction prohibited without permission.



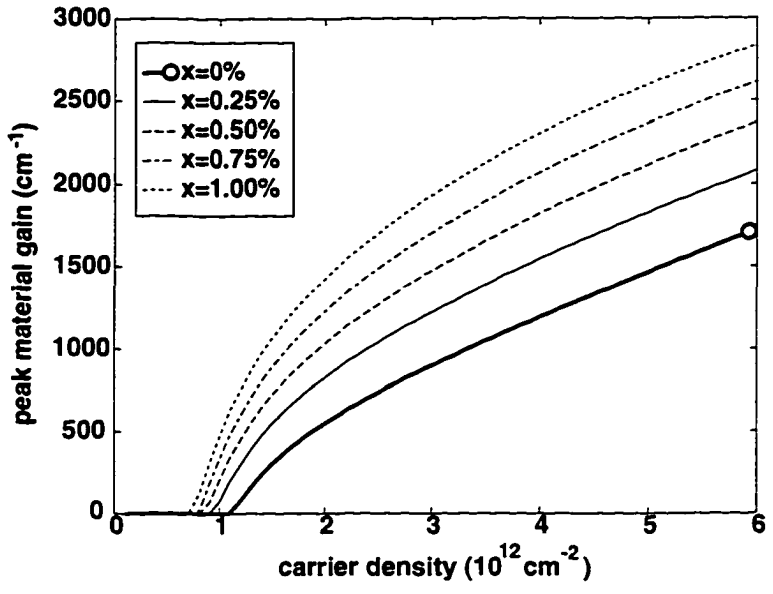
(c)

Figure 3.2: (c) Linewidth enhancement factor versus peak material gain for a 50 Å $In_{0.1}Ga_{0.9}As$ QW on GaAs, showing the different contributions to α.

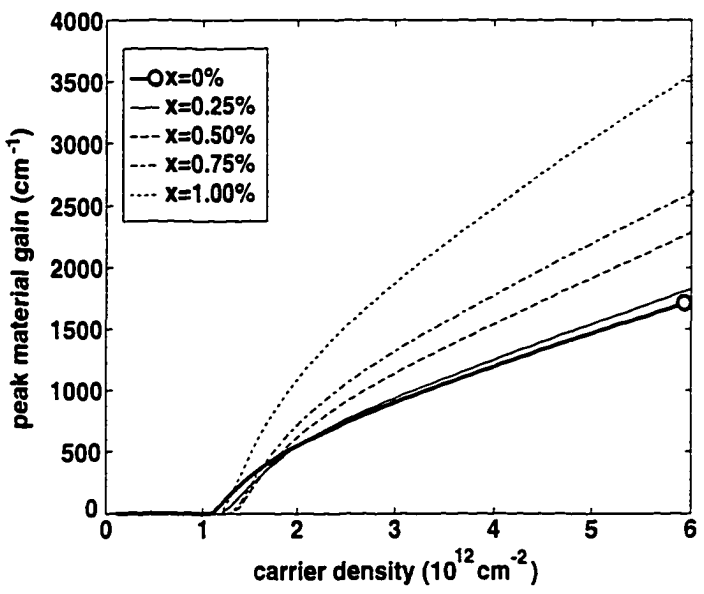
at for typical gain per well values in a MQW laser ($\sim$ 1000 cm^{-1}. The linewidth enhancement factor is significantly lower for tensile strain values $\epsilon > 0.25\%$; for these compositions the output is calculated to be TM-mode. As shown in Fig. 3.5, carrier movement in the well along the transverse direction will be limited by the confinement; hence the plasma effect due to the carrier density residing in the well is assumed to be negligible.

The calculations indicate that increasing strain not only provides better gain but also a lower linewidth enhancement factor. It is advantageous for high-speed optical communication systems to use MQW lasers due to their enhanced differential gain, which in turn lowers the threshold carrier density per well. Given that the strained systems exhibit lower values of α at low carrier densities, when temperature is a consideration, MQW strained systems again are the optimal route to pursue.

Reproduced with permission of the copyright owner. Further reproduction prohibited without permission.



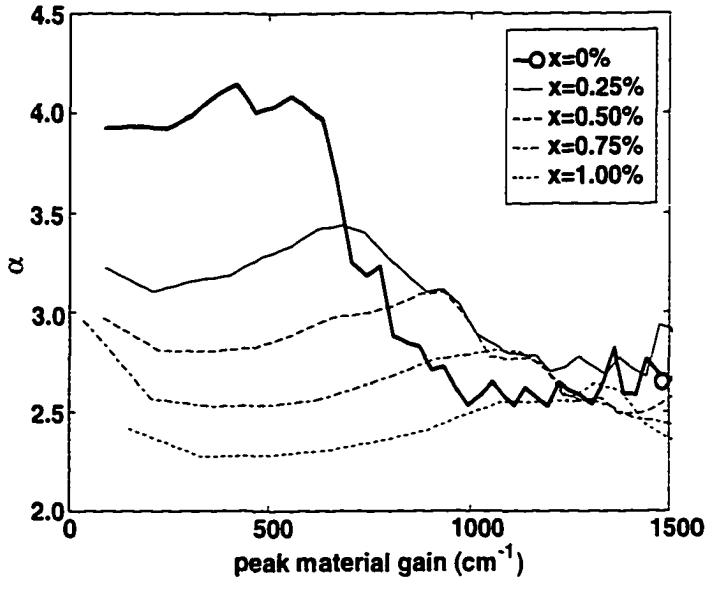
(a)



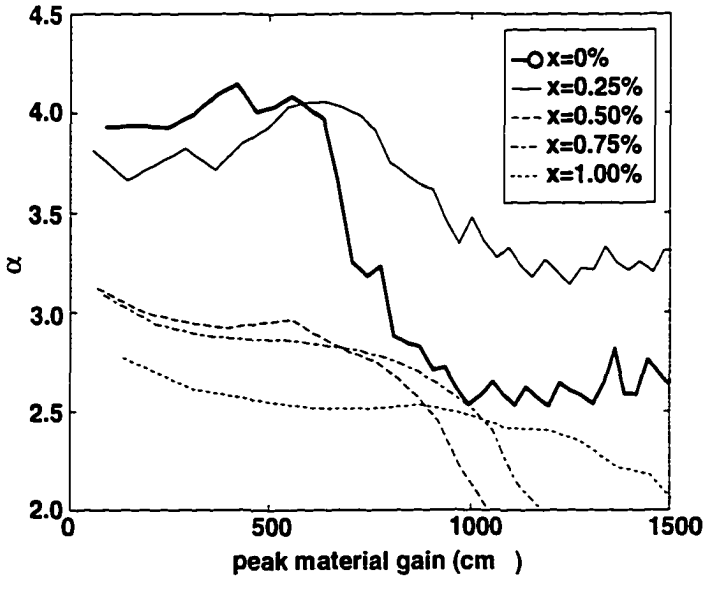
(b)

Figure 3.3: Peak material gain versus radiative carrier density for a 50 Å $In_{1-x}Ga_xAs_yP_{1-y}$ well (on InP) with (a) compressive strain and (b) tensile strain.

Reproduced with permission of the copyright owner. Further reproduction prohibited without permission.



(a)



(b)

Figure 3.4: Linewidth enhancement factor versus radiative carrier density for a 50 Å $In_{1-x}Ga_xAs_yP_{1-y}$ well (on InP) (a) compressive strain and (b) tensile strain.

Reproduced with permission of the copyright owner. Further reproduction prohibited without permission.

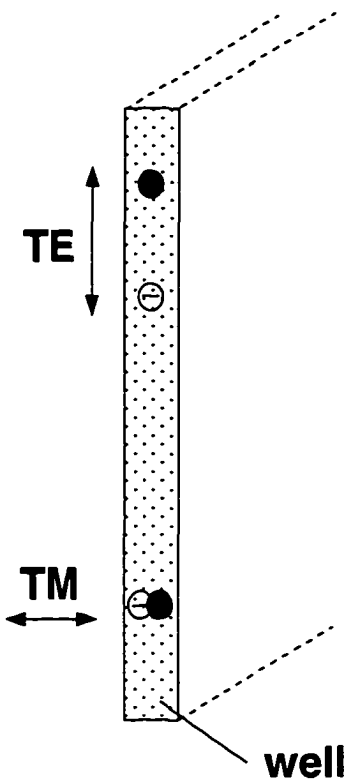


Figure 3.5: Carriers confined in the wells do not contribute to the plasma effect for the TM polarization as they are not free to move in the along in the transverse direction. After [37].

Reproduced with permission of the copyright owner. Further reproduction prohibited without permission.

0.2 μm	$In_{0.53}Ga_{0.47}As$	p^+ (2.0×10^{18})
1.7 μm	InP	p (2.0×10^{18})
400 Å	InGaAsP (λ = 1.1 μm)	undoped
1600 Å	InGaAsP (λ = 1.2 μm)	undoped
500 Å	$In_{1-x}Ga_x As$ - 50 Å (4 wells) InGaAsP (λ = 1.2 μm) - 100 Å	undoped
1600 Å	InGaAsP (λ = 1.2 μm)	undoped
400 Å	InGaAsP (λ = 1.1 μm)	undoped
1.3 μm	InP	n (8.0×10^{18})
	n^+ InP Substrate	

Figure 3.6: MQW-SCH strained layer laser structure used for the devices under study in this chapter. From [41].

3.3 Experimental Results

Based on the the results of the previous section, at low levels of injection, the effect of strain is to reduce the linewidth enhancement factor. In addition, α decreases as temperature decreases. The effect of strain on α has been previously observed experimentally [36]-[39]. However, the effect of both temperature and strain on α has not been reported.

Broad area MQW $In_xGa_{1-x}As$/InP lasers, fabricated and reported on previously by Dr. Doyle Nichols [41], were chosen for experimental study. The device structure is given in Fig. 3.6. The values of In composition chosen for the experiment were x = 48% (tensile strain), x = 53% (lattice-matched), and $x \subset \{58\%, x = 63\%\}$ (compressive strain). The quantum wells are 50 Å wide with 100 Å unstrained InGaAsP barriers (λ= 1.2 μm) Devices were tested at 278K, 293K, and 308K.

Reproduced with permission of the copyright owner. Further reproduction prohibited without permission.

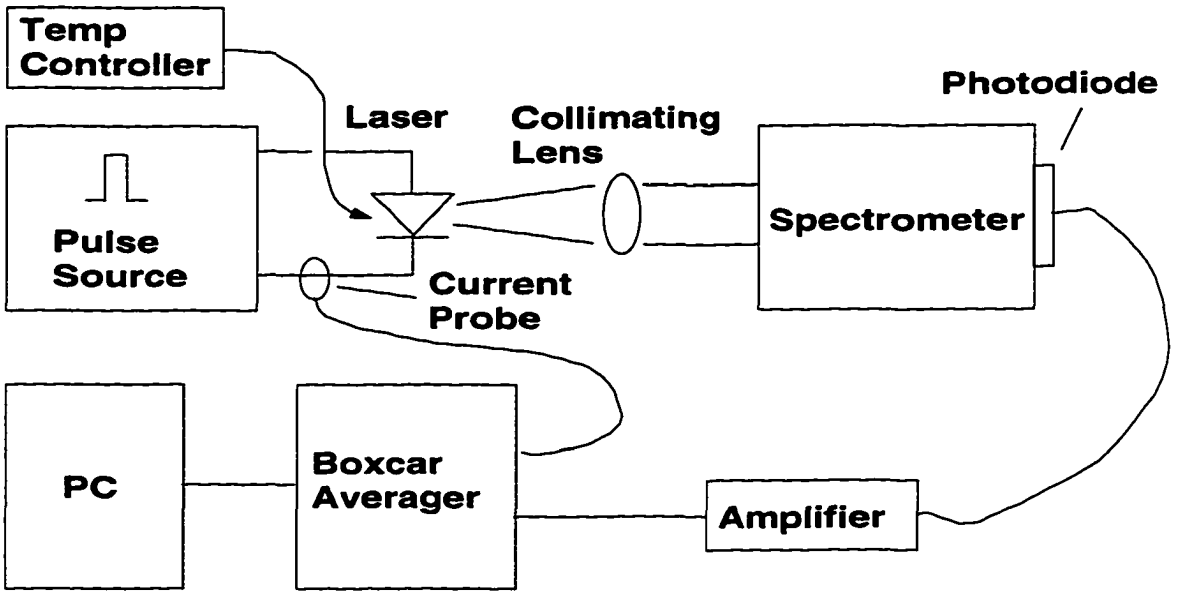


Figure 3.7: The experimental setup used for measuring linewidth enhancement factor.

The experimental setup is shown in Fig. (3.7). The laser is biased using a high voltage short-pulse voltage source (Avtech AVR-C) with a duty cycle of 0.1% for a 0.2 ms period. The output light is collimated by a lens which has low loss at 1.55 μm (FPO F-L10B), and is focused onto the entrance slit of a 0.75 m spectrometer (Spex 1702/04). Light exiting the spectrometer grating is detected by a 1-mm diameter Judson thermoelectrically cooled photodiode, whose output goes to a Judson transimpedance amplifier with a gain of 10^6. The amplifier output is connected to an SRS boxcar averager, where data is sampled and recorded on the computer.

The temperature range is set with a temperature controller (Marlow Industries SE-5000). The range of temperatures used in this study is one that the controller could reliably cool the device heatsink down with stability. (It is worth noting that cooling a device to 5C in an air ambient will cause condensation and therefore result in a halt of laser operation, unless the dew point is very low.) Temperature stability is extremely important since a temperature-induced wavelength shift of the output

Reproduced with permission of the copyright owner. Further reproduction prohibited without permission.

% In	J_{th} ($\frac{A}{cm^2}$) T=5K	T=20K	T=35K	T_0 (K)
48	940	1320	2040	38.66
53	800	1195	1930	34.09
58	500	750	1170	35.5
63	486	680	1080	37.6

Table 3.2: Measured threshold current density J_{th} versus and characterstic temperature T_0 versus device temperature for the compositions used in this study

light results in significant error in the calculation of α.

In Table 3.2 the measured threshold densitiess are given. Using the relation

$$J = J_0 e^{\frac{T}{T_0}} \tag{3.8}$$

the characteristic temperature T_0 can be determined. A higher value of T_0 denotes a weaker dependence on the operating temperature and is more desirable for high-temperature applications. Although the measured values of characteristic temperature are slightly below typical values of InGaAs/InP devices (50K) [44], the significant change in threshold current with temperature affords the opportunity to study the shift in α with temperature due to the expected shift in the index of refraction from the number of free carriers present.

Experimentally, α can be obtained from measurement using Eq. (3.5),

$$\alpha = \frac{4\pi}{\lambda} \frac{dn/dN}{dg/dN} \tag{3.9}$$

The change in the mode refractive index dn is determined from the wavelength shift $d\lambda$ of the Fabry-Perot mode, and is given by

$$dn = \frac{\lambda}{2L\Delta\lambda} d\lambda \tag{3.10}$$

Reproduced with permission of the copyright owner. Further reproduction prohibited without permission.

where $\Delta\lambda$ is the Fabry-Perot mode spacing, L is the cavity length and $d\lambda$ is the shift in wavelength when current is varied by an amount dI.

The net modal gain G is obtained using the Hakki-Paoli method [45],

$$G = \frac{1}{L}\ln\left(\frac{\rho^{\frac{1}{2}} - 1}{\rho^{\frac{1}{2}} + 1}\right), \tag{3.11}$$

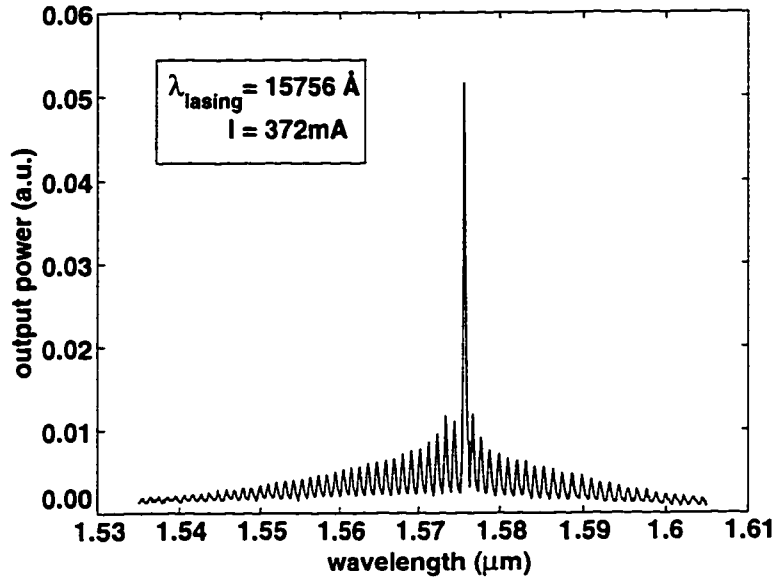
where ρ is the intensity ratio of a peak to its adjacent valley in the emission spectra. Substituting Eq. (3.6) and Eq. (3.7) into Eq. (3.5) yields [42],[43]

$$\alpha = \frac{2\pi}{L\Delta\lambda}\frac{d\lambda}{dG}. \tag{3.12}$$

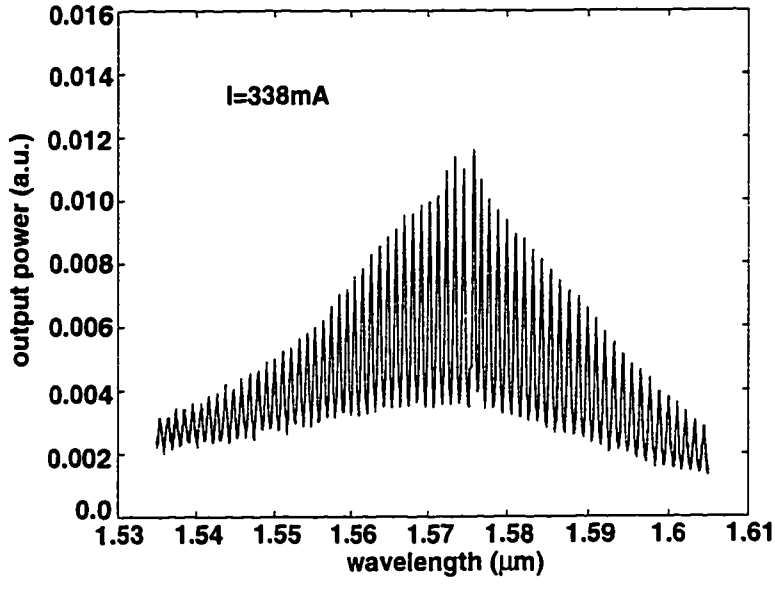
Figure 3.8 shows typical output spectra (for 63% In concentration at 20 C) and the subsequent calculation of α. In Fig. 3.8(a) is shown the output spectrum just above threshold where only a single mode dominates, and Fig. 3.8(b) is the output spectrum just below threshold. Figure 3.8(c) plots the spectra at two currents below threshold, along with the wavelength shift $d\lambda$ and Fabry-Perot shift $\Delta\lambda$. From this, $\rho(\lambda)$ is calculated for each current and the net modal gain minus loss $G(\lambda)$ are plotted in Fig. 3.8(d) (which have been smoothed to remove irregularities). In this particular instance, a value of $\alpha(\lambda_l) = 1.7$ was obtained ($\lambda_l = 15756$ Å).

In Fig. 3.9 is shown results of the measured dependence of $\alpha(\lambda_l)$ versus the strain compositions and temperatures in this study. The measured data agrees qualitatively with theoretical predictions made in the previous secition. Examining Eq. (3.12), the linewidth enhancement factor is expected to decrease as the differential gain increases. As demonstrated by previous calculations, both increase in strain and decrease in temperature result in an increase of the differential gain. In addition, previous studies on these devices [41] have shown a monotonic increase in differential gain with compressive strain over this composition range. This behavior is exhibited in Fig. 3.9 as α monotonically decreases with compressive strain.

Reproduced with permission of the copyright owner. Further reproduction prohibited without permission.



(a)



(b)

Figure 3.8: The spectrum for the 4 QW $In_{0.63}Ga_{0.37}As/InP$ laser at T=20C (a) slightly above threshold and (b) slightly below threshold.

Reproduced with permission of the copyright owner. Further reproduction prohibited without permission.

It is important to estimate the uncertainty in the measurement to ensure that the data obtained is not obscured by error. In Fig. 3.10 is shown the errorbars for the calculation of α where $x = 58\%$. Here the sources of error are considered to be temperature fluctuations (arbitrary wavelength shifts) and spectrometer resolution. The error bars are calculated using Gaussian quadrature, of which the main component is the error due to the uncertainty in spectrometer resolution (0.05 Å).

With an increase in compressive strain $\epsilon \geq 0\%$, the variation of the linewidth enhancement factor with temperature decreases as strain increases, which can be deduced from the improvement in characteristic temperature associated with increased strain. The minimum wavelength shift with temperature $\frac{d\lambda}{dT}$ for these devices was found to be at $x = 48\%$ [47], shown in Fig. 3.11, and is the reason the variation of α with T is smaller at that particular compostion. Although $\frac{d\lambda}{dT}$ is larger in the rest of the compositions, the increase in differential gain offsets it enough to reduce α.

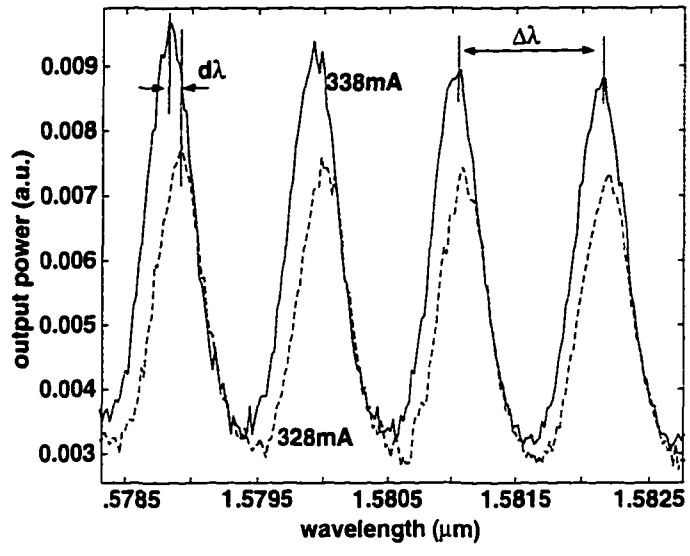
Calculations show minimal change of α with T for this temperature range, because the calculated free carrier component of α is expected to change little over this temperature range. However, such a large change in J_{th} with T implies that a highly temperature-dependent recombination mechanism is occuring. Auger recombination, considered to be a main non-radiative recombination mechanism in InP-based lasers due to the small bandgap of InP, may be the reason behind this temperature dependence of J_{th}. The large wavelength shift with temperature is due to a large modulation of the refractive index. This implies that a significant temperature-dependent free carrier absorption mechanism is occuring.

Reproduced with permission of the copyright owner. Further reproduction prohibited without permission.

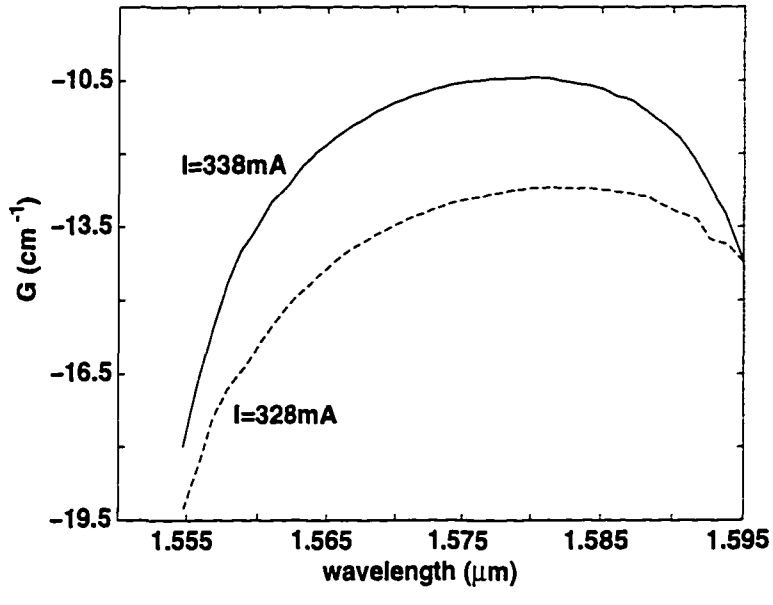
3.4 Conclusions

Theoretical calculations for GaAs- and InP-based MQW lasers predict that the linewidth enhancement factor will decrease with increased strain and reduced temperature, due to the improvement in the differential gain. Temperature-dependent measurements, done for the first time, and strain-dependent measurements are done simultaneously to obtain the behavior of the linewidth enhancement factor on strain and temperature for InP-based MQW lasers. Measurements agree qualitatively with the theoretical prediction of the behavior of α. Deviation from the theoretical prediction is expected to be due to a large free-carrier absorption mechanism in these devices.

Reproduced with permission of the copyright owner. Further reproduction prohibited without permission.



(c)



(d)

Figure 3.8: (c) spectra for the 4 QW $In_{0.63}Ga_{0.37}As/InP$ laser at two currents below threshold and (d) $G(\lambda)$.

Reproduced with permission of the copyright owner. Further reproduction prohibited without permission.

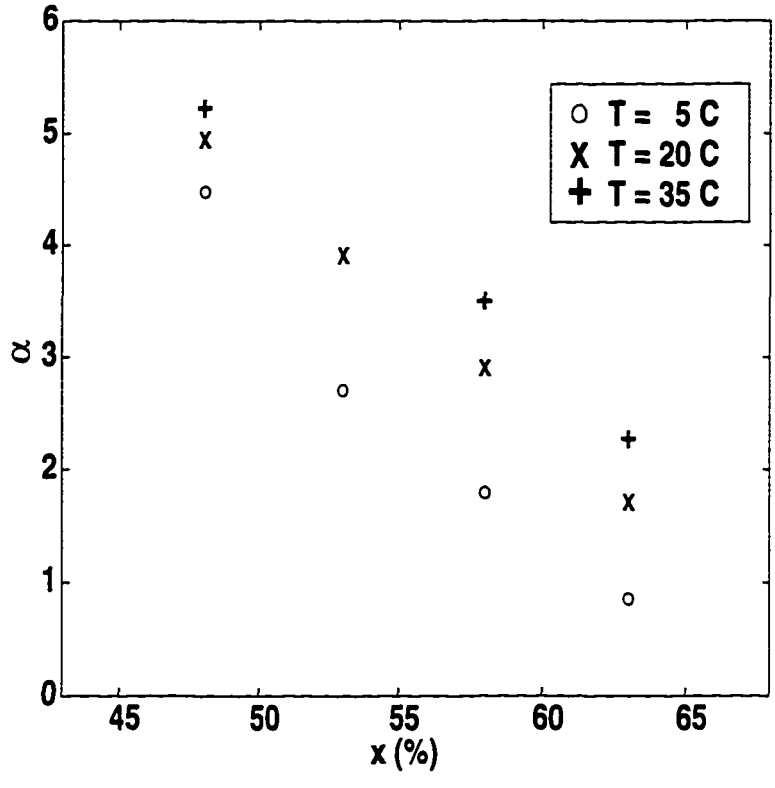


Figure 3.9: Measured linewidth enhancement factor versus composition for the devices, at different temperatures, for the devices used in this study.

Reproduced with permission of the copyright owner. Further reproduction prohibited without permission.

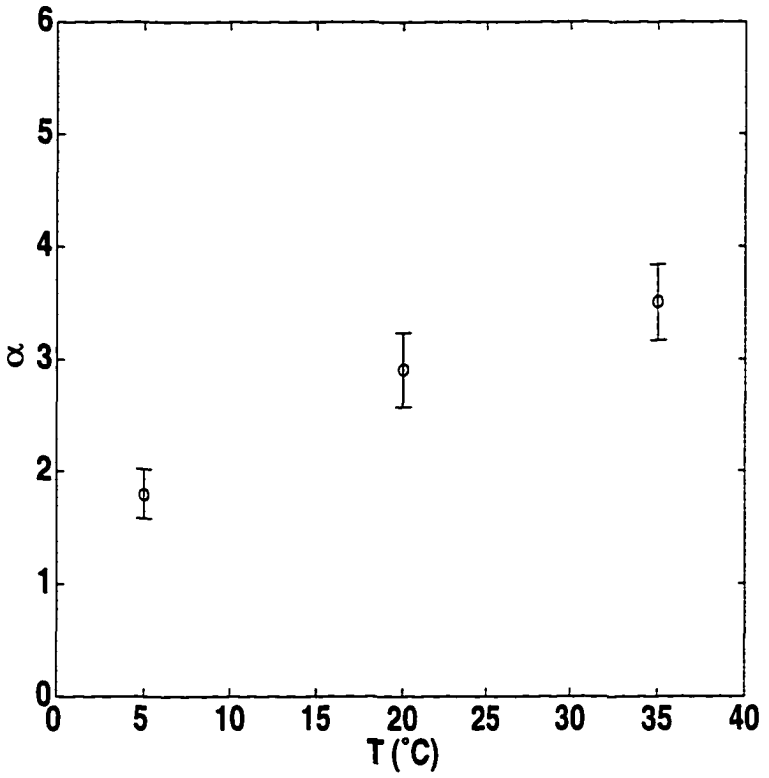


Figure 3.10: Measured linewidth enhancement factor versus temperature for the 4QW $In_{.58}Ga_{.42}As/InP$ laser. The plot indicates the error due to temperature fluctuations and spectrometer resolution.

Reproduced with permission of the copyright owner. Further reproduction prohibited without permission.

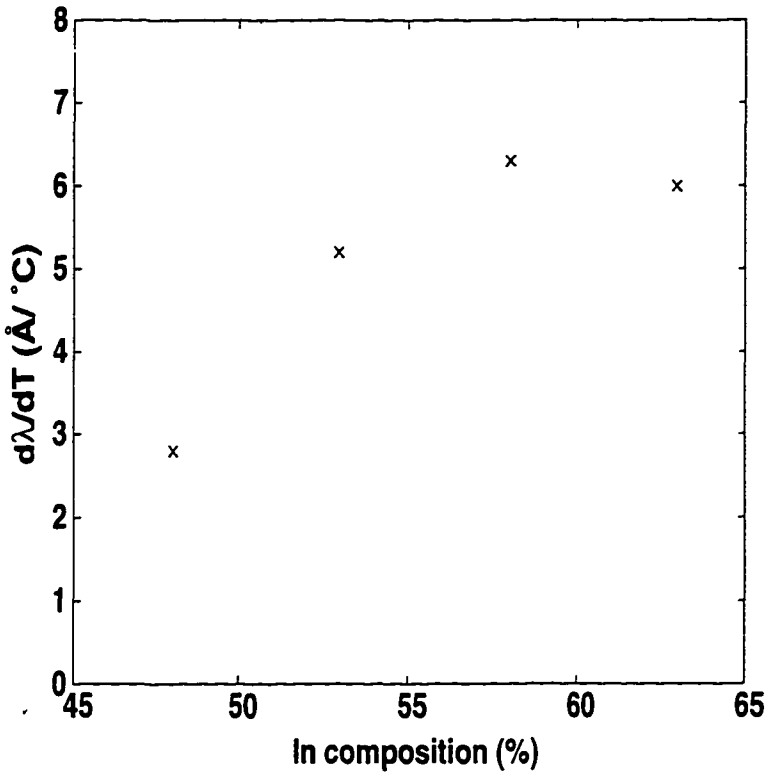


Figure 3.11: A plot of $\frac{d\lambda}{dT}$ with In composition for the devices studied. From [47].

Reproduced with permission of the copyright owner. Further reproduction prohibited without permission.

CHAPTER IV

EFFECTS OF NON-UNIFORM CHARGE INJECTION ON GAIN, THRESHOLD CURRENT, AND LINEWIDTH ENHANCEMENT FACTOR FOR InP-BASED AND GaAs-BASED MULTIPLE QUANTUM WELL LASERS

4.1 Introduction

Multiple quantum well and strained MQW lasers show improvements over conventional double heterostructure lasers in threshold current, modulation bandwidth, and linewidth enhancement factor due to higher gain, differential gain, and confinement factor values. In the design of long wavelength lasers (say operating at 1.55 μm), Auger recombination is quite important at room temperature. Due to the strong carrier density dependence of Auger recombination rate, it is important that the carrier density in the active region, n_{th}, at lasing be as small as possible. This can be accomplished by using an active region which has a large number of quantum wells. The large number of wells allows a larger optical confinement factor for the laser so that the gain per well needed to overcome losses becomes small. This in turn reduces n_{th}. As a result MQW-based active regions are widely used in InP-based 1.55μm systems.

Reproduced with permission of the copyright owner. Further reproduction prohibited without permission.

Recently, very high performance 1.55 μm lasers have been demonstrated using an active region with 8 wells. For lasers designed for longer wavelengths, the optimum well number may be even higher. An important issue that has to be addressed in such lasers is the following: since the laser operates in the forward bias mode where electrons are injected from the n-side and holes from the p-side, it is expected that the injection density will be non-uniform in the active region when the well number is large. How important are the effects of non-uniform injection? In this chapter this concern is addressed. The effects of non-uniform charge injection on gain, spontaneous emission rate, threshold current density, and linewidth enhancement factor are examined.

The organization of this chapter is as follows. First, in section 3.2 the structure and formalism used for theoretical study is described. In Section 3.3 theoretical results are then given, based on the model for non-uniform injection presented. Conclusions follow in section 3.4.

4.2 Formalism

In this section discussed the laser structure used in the studies will be discussed, the phemonelogical model used to simulate non-uniform injection will be presented, and the formalism used to examine the effect of non-uniform injection on laser performance will be described. Note that this section does not address the question of how non-uniform injection occurs or what its dependence on the structure chosen, temperature, biasing, etc., is. The studies are confined to answering the question: If non-uniform injection occurs, important is it for the laser operation?

The structure under study is a zero-net strain 8 well 1.55 μm InGaAsP-InP MQW laser, with 80 Å wells and 100 Å barriers, using 0.38% compressive strain in the wells

Reproduced with permission of the copyright owner. Further reproduction prohibited without permission.

and 0.303% tensile strain in the barriers [48]. A schematic for the active region is shown in Fig. 4.1(a). In steady-state it is assumed that the injected electron and hole densities follow exponential profiles which mirror each other with respect to the n- and p-injection sides. In this phenomenological model used the carrier densities are represented by a form

$$n_i = N\exp^{\frac{L(i-1)}{L_d}} \tag{4.1}$$

where n_i is the number of injected carriers in the i^{th} well, N is the number of injected carriers (n or p) in the first well on the n- or p-injection side, L is the distance between from the beginning of one well to the next, and L_d is a decay length. For uniform injection L_d is infinity.

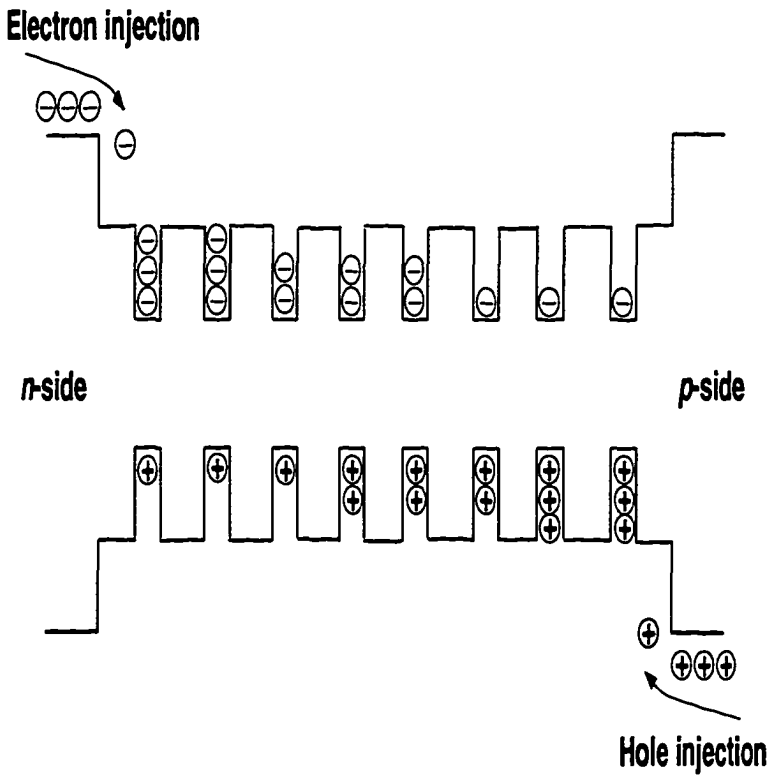
In each case of uniform or non-uniform injection, gain and spontaneous emission rates for each individual well are obtained by first calculating the bandstructure using a 4×4 $\mathbf{k} \cdot \mathbf{p}$ Hamiltonian [50] to describe the confined valence band states; the conduction band is described using the parabolic approximation with an electron of effective mass m^*[51],[25]. The effect of strain due to lattice mismatch is included [25]. After calculating both electron and hole density of states functions, for each well the subband-to-subband optical gain and spontaneous emission rate was obtained [52]:

$$\begin{aligned} g_{nm}(n_i, p_i, E) &= \frac{4\pi^2 e^2 \hbar}{n_0 c m_0^2 W E} \frac{1}{(2\pi)^2} \int d\mathbf{k} \sum_{\sigma} |\hat{\epsilon} \times \mathbf{P}^{\sigma}_{nm}(\mathbf{k})|^2 \\ &\quad \times \delta(E^e_n(\mathbf{k}) - E^h_m(\mathbf{k}) - E) \cdot [f^e(E^e_n(\mathbf{k})) + f^h(E^h_m(\mathbf{k})) - 1] \end{aligned} \tag{4.2}$$

$$\begin{aligned} R_{sp}(n_i, p_i) &= \int dE \frac{4e^2 n_0 E}{3 m_0^2 c^3 \hbar^2} \frac{1}{(2\pi)^2} \sum_{nm} \int d\mathbf{k} \sum_{\sigma} |\mathbf{P}^{\sigma}_{nm}(\mathbf{k})|^2 \\ &\quad \times \delta(E^e_n(\mathbf{k}) - E^h_m(\mathbf{k}) - E) \cdot [f^e(E^e_n(\mathbf{k}))][f^h(E^h_m(\mathbf{k}))] \end{aligned} \tag{4.3}$$

where $g_{nm}(n_i, p_i, E)$ is the optical gain at photon energy E from the i^{th} well with electron density n_i and hole density p_i from the n^{th} electron subband and m^{th} hole

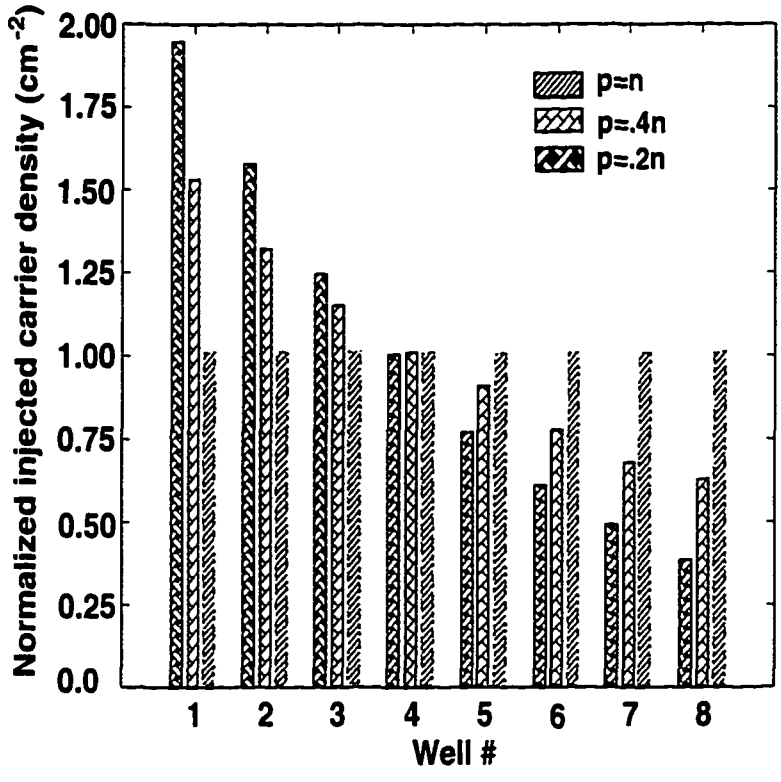
Reproduced with permission of the copyright owner. Further reproduction prohibited without permission.



(a)

Figure 4.1: (a) Visualization of non-uniform charge injection into a MQW structure from the n-injection side.

Reproduced with permission of the copyright owner. Further reproduction prohibited without permission.



(b)

Figure 4.1: (b) Normalized injected electron density distribution for an 8-well MQW laser for the uniform and non-uniform charge injection cases considered in this study.

subband, $R_{sp}(n_i, p_i)$ is the spontaneous emission rate from the i^{th} well, e is the electron charge, n_0 is the refractive index of the active region, c is the vacuum speed of light, m_0 is the free electron mass, W is the active region width, $\hat{\epsilon}$ is the polarization of the light, $\mathbf{P}^{\sigma}_{nm}$ is the optical matrix element, and $f^e(E^e_n(\mathrm{k})$ and $f(E^h_m(\mathrm{k})$ are the distribution functions for electrons and holes in the n^{th} and m^{th} subbands with momentum $\mathbf{k}$ and energies $E^e_n(\mathrm{k})$ and $E^h_m(\mathrm{k})$, respectively. To get the total gain and spontaneous emission rates for a particular case, it follows that

$$g_{tot}(n_{tot}, E) = \sum_{i=1}^{8} g(n_i, p_i, E), \tag{4.4}$$

Reproduced with permission of the copyright owner. Further reproduction prohibited without permission.

$$R_{sp_{tot}}(n_{tot}) = \sum_{i=1}^{8} R_{sp_i}(n_i, p_i), \tag{4.5}$$

where $g_{tot}(n_{tot}, E)$ is the total gain from all wells at total carrier density n_{tot}, $g(n_i, p_i, E)$ is the gain from the i^{th} well after summing over all subbands and convolving with a Lorentzian to account for collision broadening due to carrier phonon and carrier-carrier scattering, and $R_{sp_{tot}}$ is the total spontaneous emission rate from all wells. (Note that Eqs. (4.2)-(4.5) are similar to the relevant equations in Section 2.3, the difference being that the contribution from each well has been explicitly included here.)

The threshold current density is approximated as [54]

$$J_{th} = e[An_{th} + R_{sp}(n_{th})] + J_A(n_{th}), \tag{4.6}$$

where n_{th} is the total three-dimensional threshold carrier density, $R_{sp}(n_{th})$ is the total spontaneous emission rate at threshold, A is the Shockley-Read-Hall non-radiative recombination coefficient, and $J_A(n_{th})$ is the Auger recombination current density at threshold It is assumed at threshold stimulated emission is negligible compared to spontaneous emission. In InP-based devices the CHHS process dominates the Auger recombination rate. Hence, Auger recombination takes the form

$$J_A = eC_A \sum_{i=1}^{8} n_{th_i} p_{th_i}^2, \tag{4.7}$$

where C_A is the Auger recombination coefficient, and n_{th_i} and p_{th_i} are the corresponding 3-dimensional electron and hole densities, respectively.

4.3 Theoretical Results

The decay length, L_d, is used as a variable in the study to introduce a nonuniform charge distribution. In this study, the decay length value is chosen such that the

Reproduced with permission of the copyright owner. Further reproduction prohibited without permission.

number of holes in the n-injection side well (or the number of electrons in the p-injection side well) is 20% (L_d = 783 Å) of, 40% (L_d = 1375 Å) of, or equal to ($L_d = \infty$) the number of electrons in the n-injection side well. Figure 4.1(b) carrier distribution profile from the n-injection side. The exponential profile appears to be a simple, yet good, approximation when compared to more rigorous simulations involving the carrier transport equations and laser rate equations [49],[56].

Under non-uniform injection, in some wells the electron density is larger than the hole density while in others the hole density is larger than the electron density. Since the hole effective mass is much larger (in this material system) than the electron effective mass, an increase in the number of holes in a well will have a larger effect on the Fermi hole distribution function than an equal increase in the number of electrons, due to the positioning of the (hole or electron) quasi-Fermi energy level via the density-of-states function. Therefore, under non-uniform injection, it is expected for a given total carrier density the p-injection side well contributes significantly more to the total peak gain than the n-injection side wells. In Fig. 4.2, the gain-energy curves are shown for the uniform injection case and for a non-uniform injection case (L_d = 783 Å). In the non-uniform case the gain-energy relation is shown for the well closest to the n-injection side (where $p = .2n$) and for the well closest to the p-injection side ($n = .2p$). The criteria for positive gain,

$$E_{fn} - E_{fp} > E, \tag{4.8}$$

is satisfied for greater photon energies at the n-injection side well than at the p-injection side well with L_d = 783 Å, since the electron density-of-states is smaller. This is also shown in Fig. 4.2.

Using Eq. (4.4, the total peak gain versus total carrier density is calculated from

Reproduced with permission of the copyright owner. Further reproduction prohibited without permission.

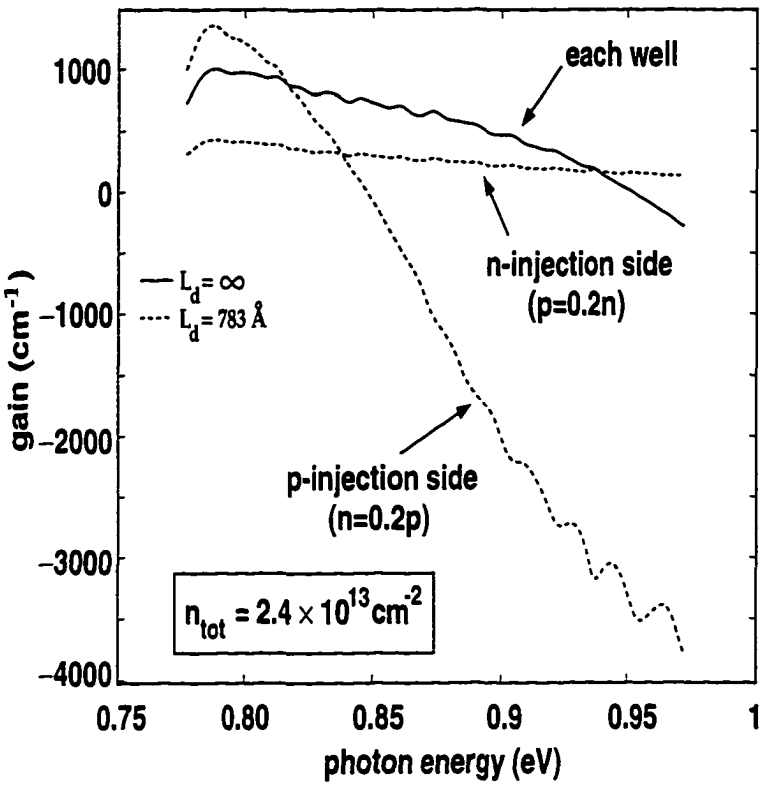


Figure 4.2: Single well gain spectrum of the well closest to the n-injection side and the well closest to the p-injection side for $L_d = 783$ Å, and single well gain spectrum of well under uniform injection. The slight irregularities in the gain curves are a consequence of the numerical procedure and have no noticeable effect on the quoted results.

Reproduced with permission of the copyright owner. Further reproduction prohibited without permission.

all wells for the distributions plotted in Fig. 4.1(b). The results are shown in Fig. 4.3. It is seen that the total peak gain decreases as decay length decreases, although the variation in total peak gain between the different decay lengths is only $\sim 10\%$. This can be explained via the phenomenological model. Following the discussion of the preceding paragraph, gain at the lasing energy E_l of the i^{th} well is expected to be primarily dependent on the hole density of the i^{th} well. The formalism shows

$$g(n_i, p_i, E_l, L_d \neq 0) + g(n_{8-i+1}, p_{8-i+1}, E_l, L_d \neq 0) < 2g(L_d = 0). \qquad (4.9)$$

i.e., at E_l the gain from any well i and its complementary well $8 - i + 1$ (since the electron and hole distributions mirror each other) under non-uniform injection is less than the gain from any 2 wells under uniform injection. Hence, the total peak gain under uniform injection is always larger. It is expected the difference between the uniform injection and non-uniform injection cases to remain small even if the electron and hole distributions do not mirror each other (from their respective injection sides), as $L_d = 783$ Å incorporates a large degree of nonuniformity.

Equation (4.5) gives the total spontaneous emission rates for the different decay lengths. These results are plotted in Fig. 4.4. The spontaneous emission rate is found to be larger under uniform injection than non-uniform injection, which follows from the discussion given in the preceding paragraphs. Although it is found that the total peak gain under uniform injection is larger, this result implies a small difference in threshold current density for different decay lengths.

From Eqs. (4.6)-(4.7) the threshold current density can be calculated. Typical values are assumed for A and C of 10^8 s^{-1} and 10^{-28} cm^6/s, respectively. For the structure presented in Section II $\Gamma_w = .0144$. Figure 4.5 shows the threshold current density, J_{th}, versus the active region gain, $\Gamma_w g_{tot}$, for both $L_d = \infty$ and $L_d = 783$

Reproduced with permission of the copyright owner. Further reproduction prohibited without permission.

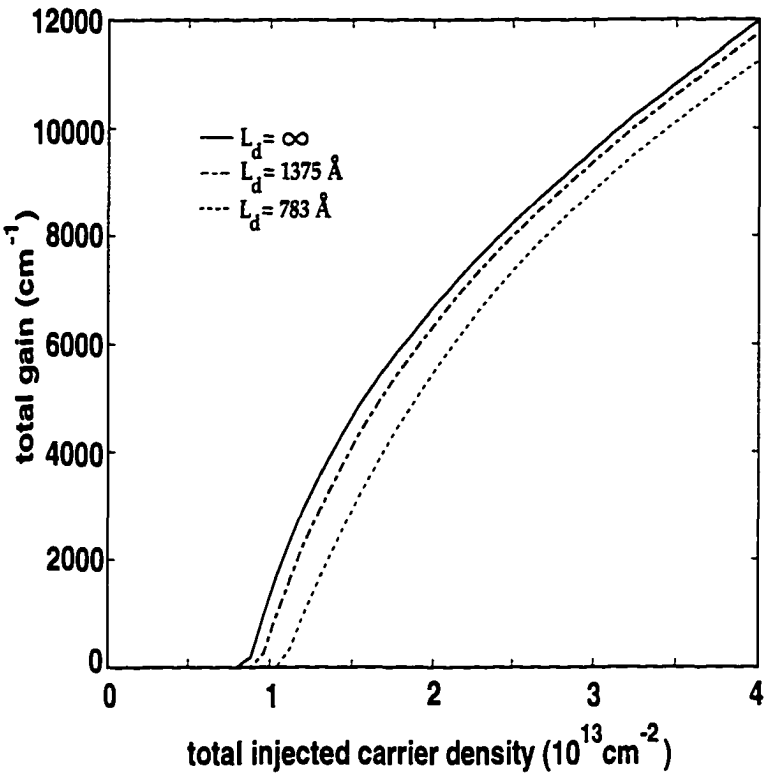


Figure 4.3: Total peak gain versus total injected carrier density for an 8-well quantum well laser for the uniform and non-uniform charge injection cases considered in this study.

Reproduced with permission of the copyright owner. Further reproduction prohibited without permission.

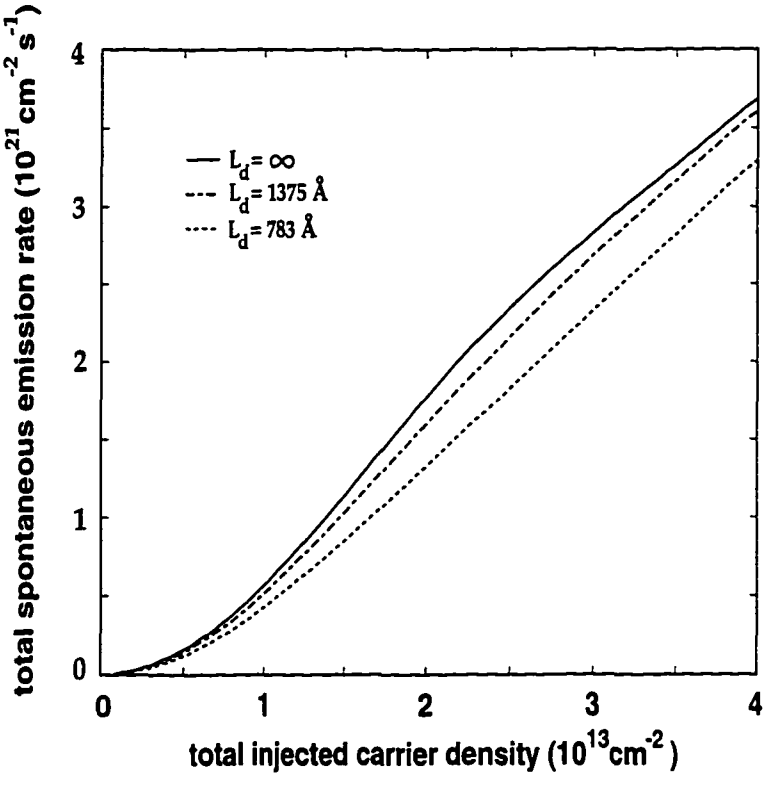


Figure 4.4: Total spontaneous emission rate versus total injected carrier density for an 8-well quantum well for the uniform and non-uniform charge injection cases considered in this study.

Reproduced with permission of the copyright owner. Further reproduction prohibited without permission.

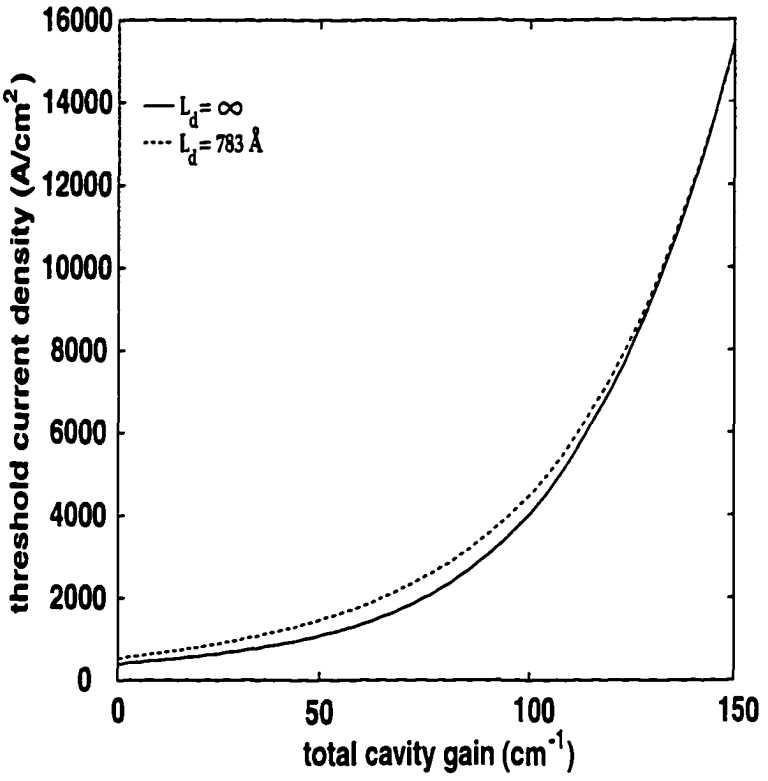


Figure 4.5: Threshold current density vs total active region gain for an 8-well quantum well structure for the $L_d = 783$ Å and uniform injection cases.

Å. The difference in J_{th} between non-uniform and uniform injection is small, with uniform injection having slightly lower threshold current density. At lower levels of injection, with n_{tot} slightly greater than the transparency carrier density, it is found that under uniform injection J_{th} will be smaller, because the gain under uniform injection is greater while the spontaneous emission rates are approximately the same, with Auger recombination not as significant as at high levels of injection. At higher levels of injection, however, J_{th} becomes nearly the same for the two cases, due to the influence of (1) the $n_i p_i^2$ term in Eq. (4.7) which effectively lowers the Auger rate for non-uniform injection, and (2) the increase in the uniform injection spontaneous emission rate.

Figure 4.6 shows the dependence of the linewidth enhancement factor, α, on total

Reproduced with permission of the copyright owner. Further reproduction prohibited without permission.

carrier density, n_{tot} for the distributions shown in Fig. 4.1. From Chapter III, the anomalous dispersion component of the linewidth enhancement factor is written as

$$\alpha_a = \frac{d\chi_R}{d\chi_I} \tag{4.10}$$

where

$$\frac{d\chi_I(n_{tot}, E_l}{dn_{tot}} = \int_0^\infty dE \frac{dg_{tot}(n_{tot}, E)}{dn_{tot}} \frac{\hbar/T_2}{(E - E_l)^2 + (\hbar/T_2)^2}, \tag{4.11}$$

and

$$\frac{d\chi_R(n_{tot}, E_l}{dn_{tot}} = \int_0^\infty dE \frac{dg_{tot}(n_{tot}, E)}{dn_{tot}} \frac{(E - E_l}{(E - E_l)^2 + (\hbar/T_2)^2}. \tag{4.12}$$

It is seen that at low injection that α increases as L_d increases, while at higher levels of injection α increases as L_d decreases. Since the calculations show the lasing energy (shown in Fig. 4.7), E_l, shifts only very slightly with increasing carrier density (for the range considered in this study). the change in linewidth enhancement factor must result from a change in the differential gain spectrum.

Figure 4.7 shows differential gain spectrums for $n_{tot} = 1.8\times10^{13}$ cm^{-2} (α larger for uniform injection) and $n_{tot} = 3.8\times10^{13}$ cm^{-2} (α smaller for uniform injection). At lower carrier densities the area under the uniform injection differential gain spectrum is greater than that of the non-uniform injection; thus, under uniform injection, α is greater. By the same reasoning, at higher injection levels under uniform injection α is less.

4.4 Conclusions

In this study a phenomenological model is used to represent non-uniform injection in a MQW laser. The effects of non-uniform charge injection on gain, threshold current density, and linewidth enhancement factor have been investigated. Non-uniform charge injection is seen to produce slightly smaller gain due to the reduction

Reproduced with permission of the copyright owner. Further reproduction prohibited without permission.

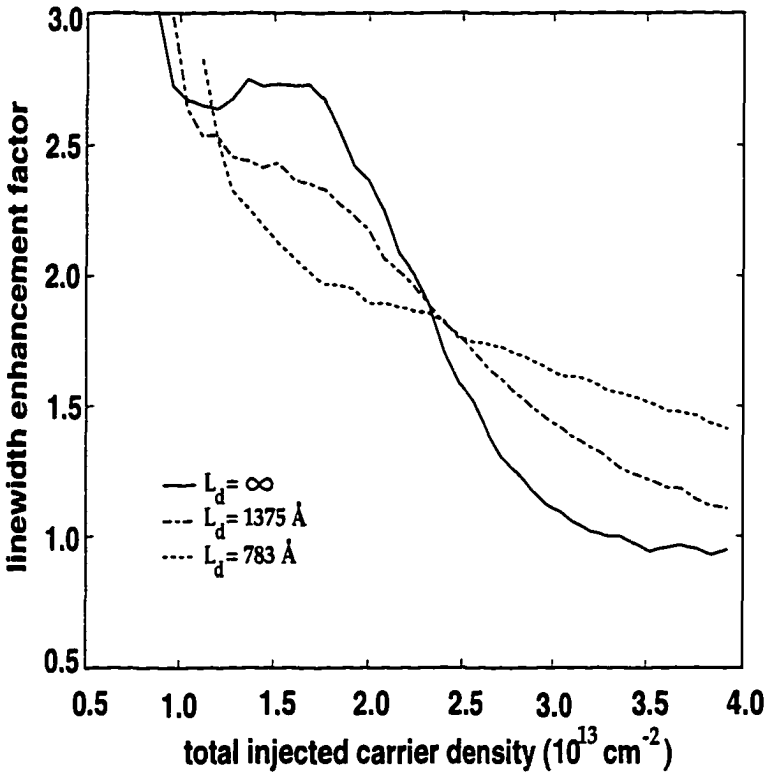


Figure 4.6: Linewidth enhancement factor versus total injected carrier density for an 8-well quantum well structure for the uniform and non-uniform charge injection cases considered in this study.

Reproduced with permission of the copyright owner. Further reproduction prohibited without permission.

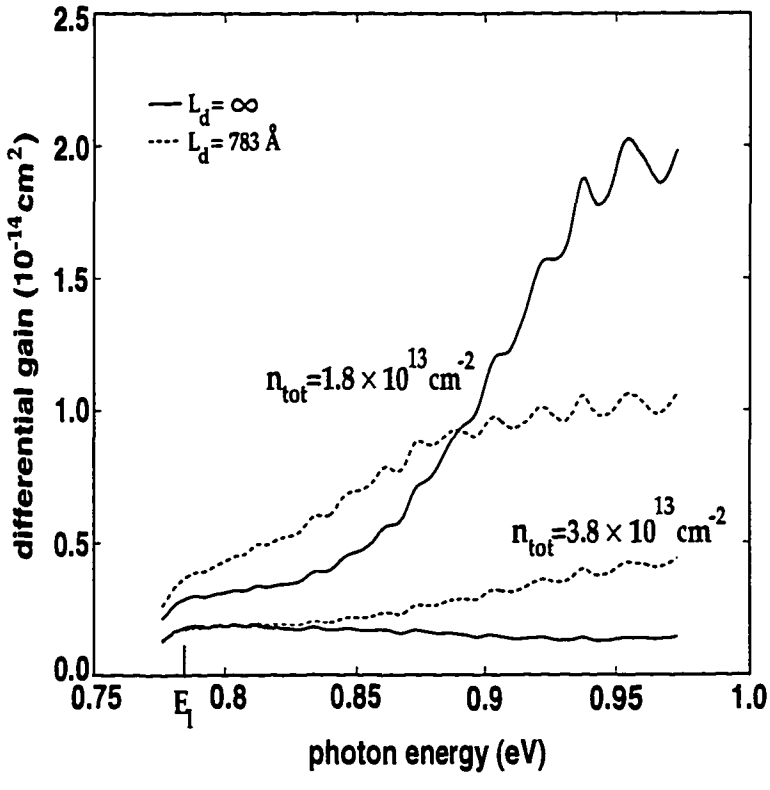


Figure 4.7: Total differential gain spectrum for an 8-well quantum well structure for the L_d = 783 Å and uniform injection cases, at two different injected carrier densities. The slight irregularities in the differential gain curves are a consequence of the numerical procedure and have no noticeable effect on the quoted results.

Reproduced with permission of the copyright owner. Further reproduction prohibited without permission.

in hole density far away from the p-injection side. This reduction in gain causes a moderate increase in threshold current density. The linewidth enhancement factor is seen to be smaller under uniform injection assuming large losses, which is typical of InP-based systems. However, although uniform injection is seen to provide the most favorable results using typical parameters, highly non-uniform injection results do not seem to significantly differ from those obtained assuming uniform injection. Since in long wavelength lasers, there are significant benefits of using a large number of quantum wells, these studies show that concerns of non-uniform injection are not serious.

Reproduced with permission of the copyright owner. Further reproduction prohibited without permission.

CHAPTER V

CARRIER DYNAMICS INVESTIGATIONS USING LARGE PULSE MODULATION

5.1 Introduction

It is well known that at present the state of the art in semiconductor lasers is such that the full bandwidth of the optical fiber network is not exploited. There are many reasons for this situation including: i) immaturity of coherent transmission/detection technology; ii) limitation of large signal direct modulation of lasers to ~10 GHz; and iii) limitations on the control of emission frequency and linewidth of semiconductor lasers. To fully exploit the bandwidth available in optical fibers, a number of approaches have been pursued, including frequency division multiplexing, wavelength division multiplexing, and high speed laser transmitters. Due to the relatively immature state of coherent transmission and detection, present optical systems need transmitters in which the on/off ratio of the optical signal is large. As a result, even though small signal modulation of >20 GHz has been demonstrated for 1.55 μm lasers [71], practical communication systems where the ON/OFF ratio is large, are limited to approxmately 10 Gb/s. In contrast, in electronic technologies, maximum frequencies of up to 350 GHz have been demonstrated in three-terminal compound semiconductor devices.

Reproduced with permission of the copyright owner. Further reproduction prohibited without permission.

The semiconductor laser is an opto-electronic device in which the limits of direct modulation are controlled by both extrinsic issues (parasitics) as well as intrinsic limits. The intrinsic limits depend upon how fast the electron and hole *occupational probabilities can be modulated at energies corresponding to the lasing energy.* This is limited by carrier thermalization times, electron-hole recombination times, and photon lifetimes. In the case of large signal modulation where the laser is modulated from a value below threshold to a value above threshold, relaxation oscillations limit modulation bandwidth to values determined by the electron-hole recombination times by spontaneous recombination. Since the spontaneous recombination time is $\sim$ 1 ns, the large signal modulation frequency is limited to less than 10 GHz. However, it is well known that the relaxation oscillations can be clipped off using gain switching. Optical pulses, (produced by optical pumping of the laser cavity) of less than 5 ps width have been demonstrated [60].

Although gain switching can produce short optical pulses a laser that has been gain switched needs $\sim$100 ps to recover. Therefore, it is not possible to use gain switching of a single laser to produce a stream of say 20 ps pulses separated by 20 ps. However, an optical transmitter based on a properly multiplexed *multi-laser system* could be capable of very high speed large signal modulation.

An architecture that incorporates a multi-laser system was presented in Chapter I, Fig. 1.3. The envisaged system consists of N lasers as shown. The output of the lasers is coupled into the same outgoing fiber. The incoming electrical data stream is demultiplexed so each laser has a *short operation time and a long recovery time.* The system considered thus depends upon *both space and time division multiplexing.* An incoming electrical data stream is multiplexed electronically across an array of lasers so that a single datum pulse causes gain switching of a particular laser. The

Reproduced with permission of the copyright owner. Further reproduction prohibited without permission.

next pulse is used to gain switch the next laser and so on. As a result, each laser is gain switched at a rate of B/N where B is the data rate of the incoming signal. Since N can be made to be ~30, each laser has a fairly long recovery time before it is gain switched again.

Gain switching of the laser can also give insight into the carrier dynamics of laser operation. Ordinarily a large input current, say 500 mA, would not be used to drive a 200 μm device since such a large current could destroy the device. However, short input pulses can be used to inject large carrier densities since the total charge injected ($\Delta Q = I(t)\Delta t$) is small.

Investigation of these topics is the focus of this chapter. First, the theoretical method is outlined for the electronic and photonic characteristics for the quantum well lasers is discussed. Following this, experimental data on gain switching is presented. Results from from the gain switching experiments on different laser structures are analyzed using the formalism to examine differences between theory and experiment. A conclusion section ends the chapter.

5.2 Formalism

The formalism to describe the gain switching phenomena is two-fold. First, the electronic properties of the device must be described using the appropriate formalism. Second, the interaction between the carriers and optical field must also be properly addressed. The former can be handled by the method outlined in Chapter II. Therefore, in this section will be presented the formalism used to understand the optical output of a gain switched laser. This includes examination of the phase noise of the output pulse. Recall the description used for the photon field of the laser

Reproduced with permission of the copyright owner. Further reproduction prohibited without permission.

output. The photon field is described through the Maxwell equation

$$\nabla^2\mathcal{E} - \frac{\sigma}{\epsilon_0 c^2}\frac{\partial \mathcal{E}}{\partial t} - \frac{1}{c^2}\frac{\partial^2 \mathcal{E}}{\partial t^2} = \frac{1}{\epsilon_0 c^2}\frac{\partial^2 \mathcal{P}}{\partial t^2} \tag{5.1}$$

where $\mathcal{E}$, $\mathcal{P}$, σ, ϵ_0, and c are the electric field vector, induced polarization vector, conductivity, dielectric permittivity, and vacuum speed of light, respectively. To simplify the problem, it is assumed that the material response, governed by the intraband scattering processes, is relatively fast (<0.1 ps) compared to the photon lifetime and the carrier recombination time. The wave equation then simplifies to

$$\nabla^2\mathcal{E} - \frac{1}{c^2}\frac{\partial^2(\epsilon\mathcal{E})}{\partial t^2} = 0 \tag{5.2}$$

where the loss term has been included in the imaginary part of the dielectric permittivity.

Assuming that the laser structure has been designed to support one lateral and transverse mode, we may write

$$\mathcal{E}(r,t) = \frac{1}{2}\hat{x}\Psi(x)\Phi(y)sin(kz)E'(t)e^{-i\omega_0 t} + c.c. \tag{5.3}$$

where Ψ, Φ, k, and ω_0 are the lateral profile, transverse profile, wavenumber, and wave frequency, respectively. The time-dependent part may be recast as

$$E'(t) = \frac{1}{2}S^{\frac{1}{2}}(t)e^{-i(\omega_0 t+\phi(t))} + c.c., \tag{5.4}$$

where $E'(t)$ has been separated into magnitude and phase terms, with S and ϕ being the photon density and the phase, respectively.

The gain switching dynamics of a multi-quantum well laser can be understood by solving the rate equations for carrier density, photon density, and phase. In considering carrier dynamics, the source for carriers is assumed to be injected current density. For a multi-quantum well laser with N wells, under uniform injection each

Reproduced with permission of the copyright owner. Further reproduction prohibited without permission.

well has $\frac{1}{N}$ the total number of carriers. Carriers are lost in the active region due to nonradiative (Shockley-Read-Hall, Auger) and radiative (spontaneous and stimulated emission) recombination. Similar to Eq. (2.40) in Chapter II. The rate of change in carrier density, for a single well, can be expressed as [61]

$$\frac{dn}{dt} = \frac{J(t)}{qN} - \frac{J_{nr}(n)}{qN} - R_{sp}(n) - \Gamma R_{st}(n) + F_n(t) \tag{5.5}$$

where $n = n(t)$, $J(t)$, q, N, J_{nr},R_{sp},ΓR_{st}, and $F_n(t)$ are the carrier density, injected current density, electron charge, active region width, number of wells, optical confinement factor, stimulated emission rate per well, and Langevin forcing function representing shot noise, respectively. The non-radiative recombination current density is considered here to be a combination of the Auger recombination rate and the Shockley-Read-Hall recombination rates:

$$J_{nr}(n) = q\left[\frac{n}{\tau_{SRH}} + C_A W\left(\frac{n}{W}\right)^3\right] \tag{5.6}$$

where $\tau_{SRH}$is the Shockley-Read-Hall carrier lifetime, C_A is the Auger recombination coefficient, and W is the well width. The stimulated emission rate is written in the gain compression-limited form [62]

$$\Gamma R_{st}(n) = \Gamma v_g \sum_{\hat{\epsilon},i} \frac{g_{\hat{\epsilon},i}(n) S_{\hat{\epsilon},i}(t)}{1 + \epsilon S_{\hat{\epsilon},i}(t)} \tag{5.7}$$

where ϵ is the gain compression factor, $g_{\hat{\epsilon},i}(n)$ is the gain at carrier density n for the i^{th} mode exhibiting positive gain for polarization $\hat{\epsilon}$, $S_{\hat{\epsilon},i}(t)$ is the photon density at time t, Γ is the optical confinement factor, and v_g is the group velocity of the i^{th} mode.

Considering photon dynamics, the sources of photons in the active region include being the fraction of photons (from N wells) created from stimulated emission into

Reproduced with permission of the copyright owner. Further reproduction prohibited without permission.

the active region and the fraction of photons from radiative spontaneous recombination emitted into the lasing mode. Photons are lost through cavity absorption and by photons escaping through the cavity mirrors. As in Eq. (2.41), rate of change in photon density can then be expressed as [61]

$$\frac{dS_{\hat{e},i}(t)}{dt} = N\Gamma R_{st} - \alpha_c v_g S_{\hat{e},i}(t) + N\beta R_{sp}(n) + F_S(t) \tag{5.8}$$

where α_c, v_g, and β are the total cavity plus mirror losses, photon group velocity of the i^{th} mode in the active region, and spontaneous emission factor, respectively.

Phase fluctuations, showing a peak near the vicinity of laser threshold (and then decreasing rapidly as injected current increases), originate from the quantum mechanical nature of the lasing process [61]. Such fluctuations are responsible for the broadening of each mode, and the line width. Two mechanisms contribute to the phase noise: spontaneous emission, and carrier population fluctuations. In spontaneous emission, each randomly emitted photon contributes a change to the optical phase by a random amount. A change in carrier population affects gain, which in turn affects refractive index, and therefore changes phase. This change in the phase is responsible for the chirp of the laser. From Appendix A, the rate equation for the phase is expressed as

$$\frac{d\phi}{dt} = \frac{\alpha}{2S}\frac{dS}{dt}, \tag{5.9}$$

where α denotes the linewidth enhancement factor.

The shot noise term $F_n(t)$ and the spontaneous emission noise term $F_S(t)$ are Langevin noise sources added to the rate equations within the semiclassical treatment [63]. The shot noise term may be neglected in order to isolate the dependence of the power spectrum on quantum noise due to spontaneous emission events. The noise term $F_S(t)$ is taken to be a Gaussian random variable whose correlation time is much

Reproduced with permission of the copyright owner. Further reproduction prohibited without permission.

shorter than the photon lifetime. It can be shown that the autocorrelation is [64].[65]

$$< F_S(t)F_S(t') >= 2\beta R_{sp}(< n(t) >) < S(t) > \delta(t-t') \qquad (5.10)$$

where triangular brackets denote ensemble averages.

5.3 Experiment

In this study four 3 μm ridge waveguide lasers were used in gain switching experiments: 1) a 400 μm long 8 QW InP-based SCH structure [57], 2) a 400 μm long 8 QW InP-based Tunneling-Injection (TIL) structure [71], 3) a 200 μm long 6 QW GaAs-based TIL [5], [70], and 4) a 200 μm long 4 layer GaAs-based multi-layer quantum dot (MLQD) laser [72]. Of interest in these studies is to examine if the demonstrably improved differential gain and injection efficiency [71] of the InP-based TIL structure over the SCH structure leads to an improvement in the output pulse characteristics, and if the higher differential gain and shorter carrier lifetime of the GaAs-based QD structure [72] leads to further improvement over a TIL structure.

The setup in Fig. 5.1 was used to gain switch the laser and measure the resulting output. Here, a DC bias source (Model 505 Laser Diode Driver) is connected to the output of a comb generator (HEROTEK GC100-214) through a 50 GHz bias tee. The comb generator produces the input voltage pulse (a Gaussian pulse approximately with approximately 11V amplitude and 120 ps FWHM) used to gain switch the laser, and is driven by a 27 dBm 100MHz sine wave input (HP 83650 sweep oscillator), which also induces $\sim$ 15 dBm of feedthrough as well. The output of the bias tee is then fed via a 40GHz ground-signal-ground probe to the laser. The laser output is coupled into a fiber, through which the light is detected by a wide bandwidth photodetector (40GHz Nu Focus 1011). The detector output is amplified using a

Reproduced with permission of the copyright owner. Further reproduction prohibited without permission.

wide bandwidth amplifier (0.1 - 26 GHz MITEQ), and the amplified signal is then displayed on a high speed digital sampling oscilloscope (50 GHz Tektronix 11801B).

Each device used in this experiment had no impedance matching circuitry placed in series with it to reduce the reflected input power. Fortunately, a small signal analysis can be used to determine the input drive current of the device, as the high amplitude narrow Gaussian pulse in the time-domain transforms to a wide Gaussian with low amplitude in the frequency domain.

In determining the time-dependent current delivered the impedance of each laser was first measured as a function of bias current and frequency via the analysis of the one-port s_{11} parameter, obtained from an 8510 Network analyzer. The impedance, $Z(\omega)$, can be written

$$Z(\omega) = \frac{1 + s_{11}(\omega)}{1 - s_{11}(\omega)} Z_0, \tag{5.11}$$

where the transmission line impedance, Z_0, equals 50 Ω. The drive current due to the Gaussian input, $I(t)$, is then obtained by taking the inverse Fourier transform of $I(\omega)$, or

$$I(t) = \frac{2}{\pi}\int_0^\infty I(\omega)e^{j\omega t}d\omega = \frac{2}{\pi}\int_0^\infty V(\omega)\frac{2}{Z_0 + Z(\omega)}e^{j\omega t}d\omega. \tag{5.12}$$

Here $Z^*(-\omega) = Z(\omega)$ since $I(t)$ is real. Alternatively $I(t)$ can be found by calculating the current sourced by $V(t)$ where the load is an equivalent circuit whose response matches $Z(\omega)$, as shown in Fig. 5.2. In Fig. 5.2, R_s represents the bulk series resistance, while r_d and c_d are small signal equivalent circuit elements representing the resitance and capacitance due to minority carriers, respectively. In general, the elegance of the former method eliminates the need for fitting an arbitrary equivalent circuit to the device, but lacks the physical insight of the latter method.

In Fig. 5.4 is shown (a) stream of input pulses and (b) a single input pulse into the device. Each input pulse is approximately 10.5 V in amplitude and 120 ps wide.

Reproduced with permission of the copyright owner. Further reproduction prohibited without permission.

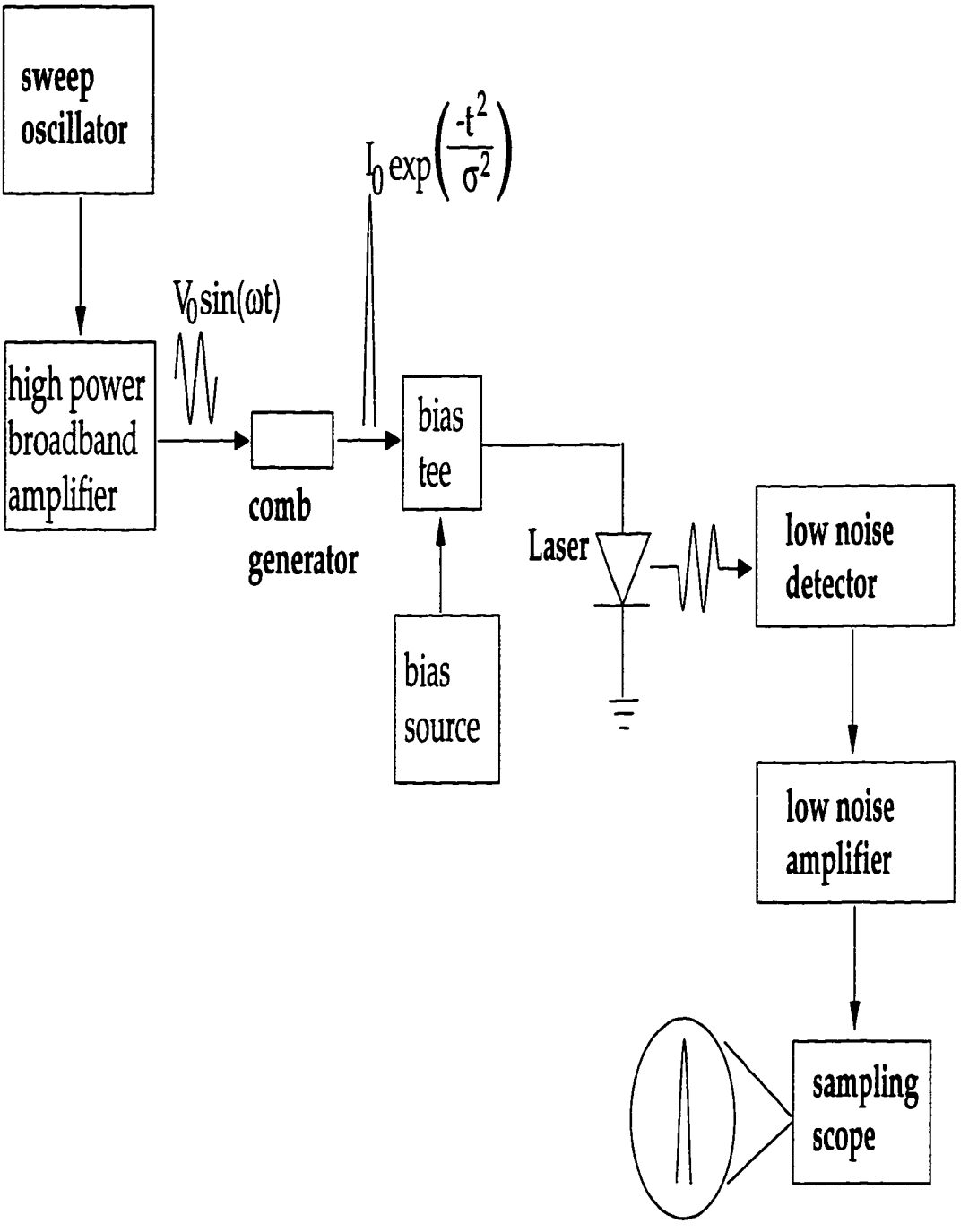


Figure 5.1: Experimental set-up for gain switching.

Reproduced with permission of the copyright owner. Further reproduction prohibited without permission.

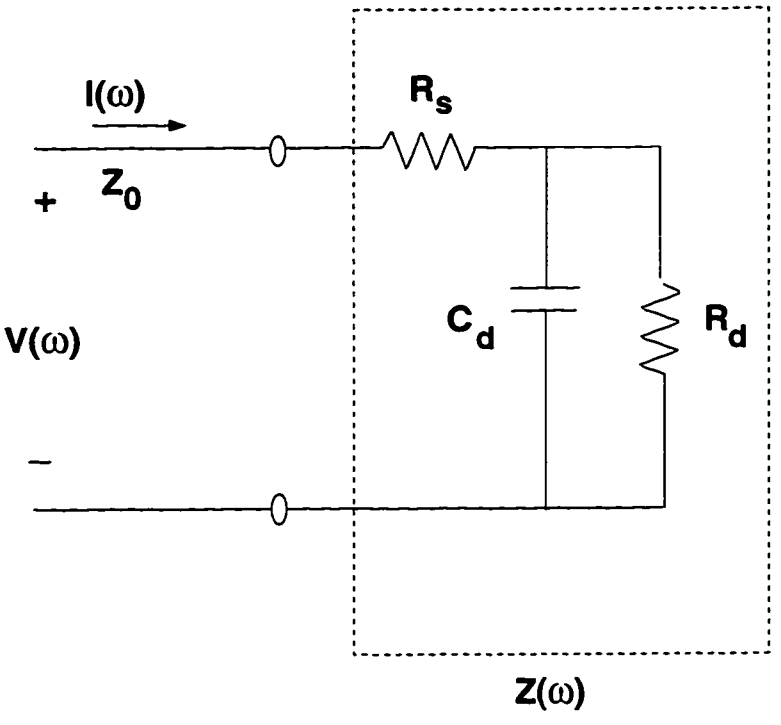


Figure 5.2: Equivalent circuit model used to fit $Z(\omega)$.

Reproduced with permission of the copyright owner. Further reproduction prohibited without permission.

Device	τ_{fwhm} (ps)	bias current (mA)	threshold current (mA)
InP SCH	55	22.5	25.0
InP TIL	35	17	22.5
GaAs TIL	45	7.0	10.0
GaAs MLQD	35	0.0	10.0

Table 5.1: Measured FWHM output at optimal bias currents for the different devices used in this study.

In Fig. 5.3 is the impedance magnitude of the 8 QW InP TIL laser at a bias of 17 mA (I_{th} ~22.5 mA). Using Eq. (5.12), the corresponding input Gaussian pulse is 325mA. Figure 5.5 gives the corresponding output pulse for an input pulse of the input pulse given in Fig. 5.4(b). The pulse is seen to be 35 ps wide. Table 5.1 gives the best measured output pulse widths for the different devices, along with the bias currents at which the laser was biased at during the measurement.

5.4 Discussion

5.4.1 Analysis of output pulses

The formalism presented can be used to examine whether the output FWHM values measured agree with theoretical prediction. Using the fourth-order Runge-Kutta method, the given rate equations are solved for the QW-based devices, while the approximation $g(n) = \frac{dg}{dn}(n - n_{tr})$, n_{tr} being the transparency current density. is used for the MLQD structure with the measured value of $\frac{dg}{dn} \sim 2 \times 10^{-14}$ [71]. For QW-based devices, terms such as $g(n)$, $R_{sp}(n)$, and α are solved starting from the quantum well bandstructure following the formalism of Chapter II. Finally, uniform injection into the wells is assumed.

In Fig. 5.7 is shown the calculated output pulse for the InP TIL laser, the

Reproduced with permission of the copyright owner. Further reproduction prohibited without permission.

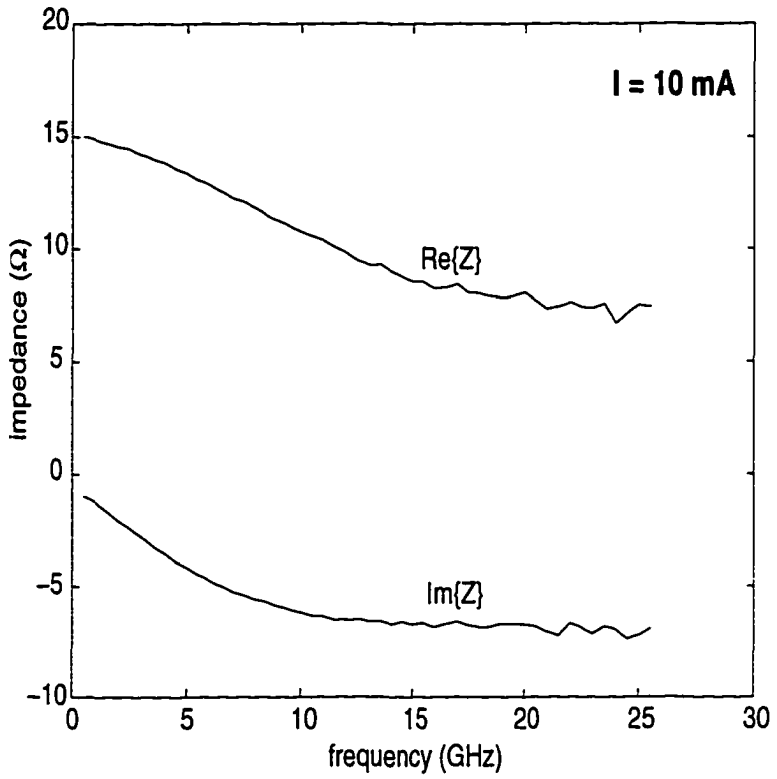
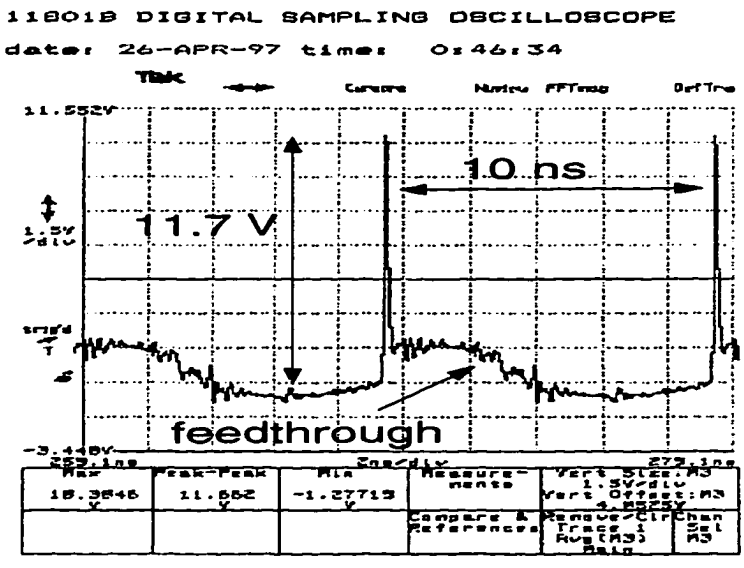
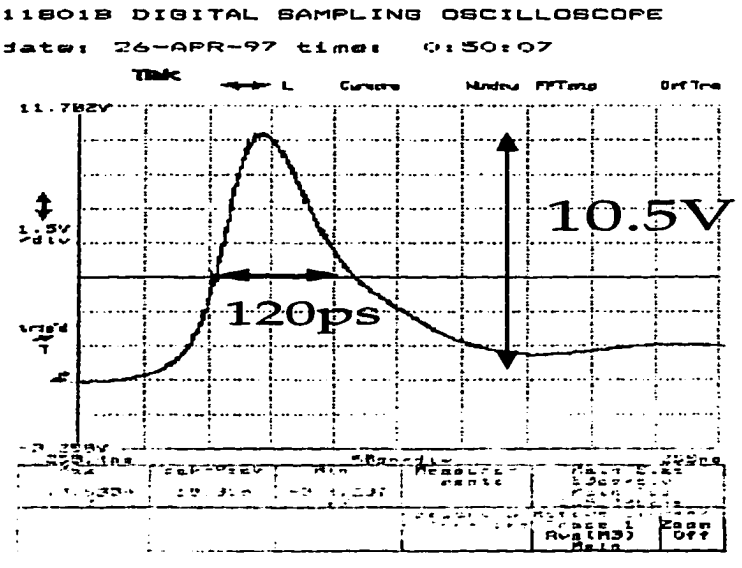


Figure 5.3: Real and parts of the complex impedance of the diode in the small signal regime. The current $I_{bias} = 10$ mA.

Reproduced with permission of the copyright owner. Further reproduction prohibited without permission.



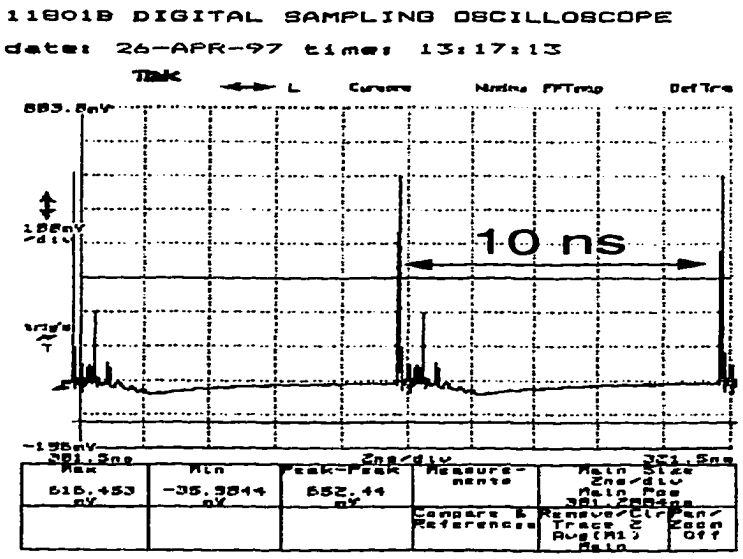
(a)



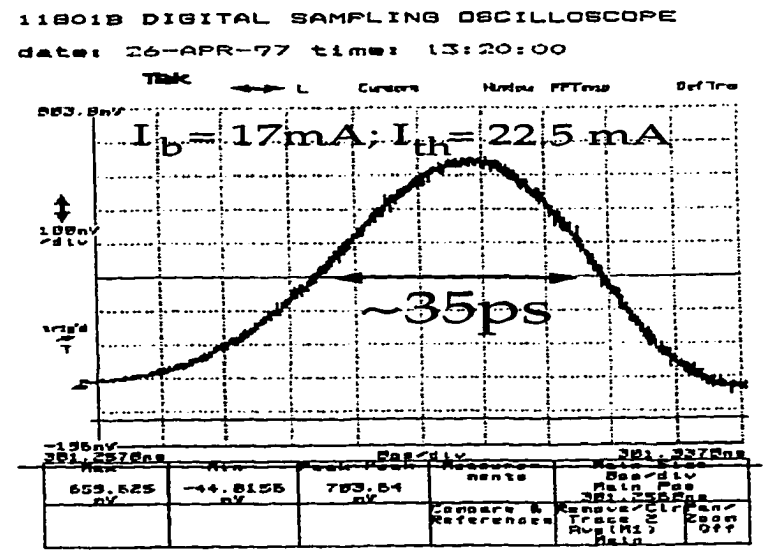
(b)

Figure 5.4: The input signal from the comb generator: (a) The input pulse train separated by 10ns, and (b) a single input from the comb generator.

Reproduced with permission of the copyright owner. Further reproduction prohibited without permission.



(a)



(b)

Figure 5.5: The output pulses from the 8 QW InP TIL laser: (a) The output pulse train separated by 10ns, and (b) a single output from the comb generator. Relaxation frequencies in (a) are due to the feedthrough.

Reproduced with permission of the copyright owner. Further reproduction prohibited without permission.

Parameter	Value	Meaning
τ	0.3 ns [71]	carrier lifetime at threshold
η_i	0.75	internal quantum efficiency
L	400 μm	cavity length
W	80 Å	well width
I_{th}	22.5 mA	threshold current
C_A	10^{-30}	Auger coefficient
β	10^{-5}	spontaneous emission factor
Γ_w	0.0145 [57]	optical confinement factor
ϵ	5×10^{-17} [71]	gain compression factor

Table 5.2: Relevant parameters used in large signal modulation calculations for the 8 QW InP-based TIL.

structure of which is given in Fig. 5.6 (the structures for the other devices can be seen in the cited references). The output is obtained using the multimode formalism. Calculated parameters such as $g(n)$ and $R_{sp}(n)$ are then slightly adjusted to agree with the experimentally measured parameters I_{th} and τ (given in Table 5.2). The theoretical output pulse is seen to have a single relaxation oscillation of $\sim$ 8 ps, and then follows the input pulse for its duration. Subsequent theoretical calculations for the other devices yield similar results. Clearly, something is unaccounted for.

The lack of agreement was unable to be resolved upon variation of the static parameters of Table 5.2. A possibility is that the gain compression coefficient may change with a large number of carriers introduced by the pulse, as ϵ has been attributed to carrier heating in Monte Carlo studies [73]. It is likely that in order to better characterize the response, unlike the static fit that was used, a dynamic value of ϵ needs to be incorporated. It is also possible that some parasitic effects in the

Reproduced with permission of the copyright owner. Further reproduction prohibited without permission.

1000 Å	$In_{0.53}Ga_{0.47}As$	p+ (1×10^{19} cm^{-3})
500 Å	$In_{0.53}Ga_{0.47}As$ linearly graded to InP	p (2×10^{18} cm^{-3})
1 μm	InP	p (2×10^{18} cm^{-3})
2000 Å	InP	p (5×10^{17} cm^{-3})
500 Å	$In_{0.80}Ga_{0.20}As_{0.43}P_{0.57}$	undoped
8 X		undoped
70 Å	$In_{0.48}Ga_{0.515}As_{0.83}P_{0.17}$ (0.9% tensile strain)	
80 Å	$In_{0.76}Ga_{0.24}As_{0.83}P_{0.17}$ (1% compressive strain)	
30 Å	InP	undoped
1000 Å	$In_{0.7}Ga_{0.3}As_{0.63}P_{0.37}$	undoped
2000 Å	InP	n (5×10^{17} cm^{-3})
1 μm	InP	n (2×10^{18} cm^{-3})
500 Å	InP linearly graded to $In_{0.53}Ga_{0.47}As$	n (2×10^{18} cm^{-3})
5000 Å	$In_{0.53}Ga_{0.47}As$	n+ (1×10^{19} cm^{-3})
	SI InP Substrate	

Figure 5.6: Layer structure for the 8 QW InP-based TIL laser.

Reproduced with permission of the copyright owner. Further reproduction prohibited without permission.

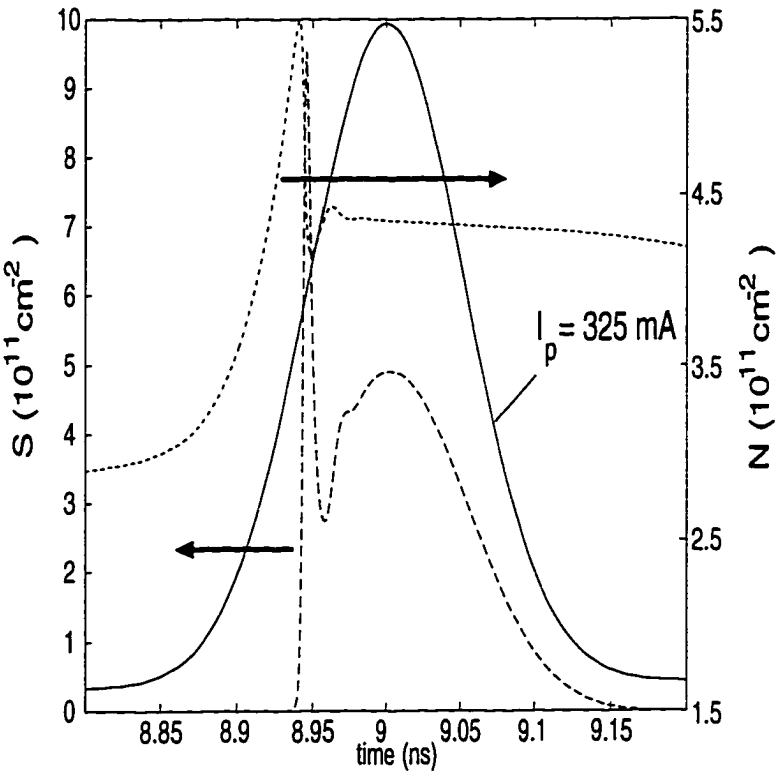


Figure 5.7: Calculated output for the InP-based TIL laser, where the input bias current is the solid line, carrier density N is the dotted line, and the photon density S is the dashed line. The width of the output optical pulse S is ~ 8 ps.

Reproduced with permission of the copyright owner. Further reproduction prohibited without permission.

device are occuring due the large input pulse; these need to be accounted for.

5.4.2 MLQD performance

Of significance is that the MLQD laser produced both the shortest output optical pulsewidth, and needed 0 mA DC bias (apart from the comb generator feedthrough) in order to accomplish gain switching. The reduced DC bias stems from the high differential gain and lower transparency carrier density expected from the superior density of states in QD systems. The short output optical pulse is likely due to the very short electron lifetime (.15 ns), evidence that the transparency carrier density itself is close to the threshold carrier density.

Another interesting observation made on the MLQD devices is that a "state-filling" effect was observed: applying additional DC bias did not result in an increase in the output optical pulse intensity. In principle, each dot only has two states. Since only a finite number of dots exist (and lase), when all of the dots are full, any additional carriers cannot contribute to the stimulated emission process.

5.4.3 Jitter

Investigating whether the jitter plays a role is important since jitter can adversely affect the timing in a data transmission system. Because the mean values of the Gaussian random variables are zero, the ensemble averages can be obtained by solving the rate equations without the noise terms. Random variables are then simulated using a Monte Carlo method [66]. Theoretically, for the structures in the study, the jitter is calculated to be less than 1 ps. Experimentally, jitter on the order of 5 ps was observed, but was deduced to be coming from the trigger output of the sweep oscillator. Since the jitter is uncorrelated, it was eliminated from the output trace using an averaging function of the oscilloscope.

Reproduced with permission of the copyright owner. Further reproduction prohibited without permission.

5.4.4 Chirp

The output chirp, $\frac{1}{2\pi}\frac{d\phi}{dt}$, is of importance since the chirp determines the dispersion of the pulse as it propagates through the fiber in the gain-switched system. From Eq. (5.9), the rate equation for ϕ is dependent on both the time derivative of S and the linewidth enhancement factor α. Since in the gain-switching system S changes quickly when the current pulse is applied, it is critical to minimize α. In Chapter III it was suggested that since the QD possesses both high differential gain and carrier confinement along all axes, it will therefore minimize the anomalous and plasma dispersion components of α, and would therefore be most suitable for the gain-switching system.

5.5 Conclusions

Gain switching experiments were done on GaAs-based and InP-based SCH, TI, and MLQD lasers. In examining the output width of the optical pulse, the limiting factor in the operation speed of the multi-laser array system presented, performance improved from the SCH to the TI structure due to the improved differential gain and injection efficiency in TI structures. Further improvement was seen in MLQD lasers, due to their extremely high differential gain.

The MLQD structures also exhibited "low input power" behavior, in that only a small DC bias (the comb generator feedthrough) was needed to bias the device. Projecting that the MLQD lasers will have the additional advantage of low linewidth enhancement factor, the MLQD is seen as possibly the best transmitter in such a multi-laser scheme.

Theoretical analysis was not seen to be in agreement with experimental results, possibly resulting from parasitics, or the necessity to incorporate a dynamic gain

Reproduced with permission of the copyright owner. Further reproduction prohibited without permission.

compression coefficient, and needs to be investigated further.

Reproduced with permission of the copyright owner. Further reproduction prohibited without permission.

CHAPTER VI

WAVE PROPAGATION FORMALISM

6.1 Motivation

In the previous several chapters certain device characteristics have been emphasized and analyzed. These characteristics have been examined through study of optoelectronic properties of the material. From that viewpoint, the linewidth enhancement factor, (Chapter III), nonuniform injection (Chapter IV), and carrier dynamics (Chapter V) have been investigated, and through bandstructure engineering improvements in these parameters can be accomplished.

In addition to bandstructure issues that determine the electronic characteristics of lasers, one has to consider the guiding aspect which controls the photonics of the device. In a laser, the waveguide formed by the carrier injection region and inner cladding layers determine the optical mode profile of the photon field propagating in the waveguide. Such factors determined by the distribution of the photon field include the optical confinement factor and the near- and far-field patterns of the emitted light. Additionally, the interfaces at the ends of the Fabry-Perot cavity determine mirror losses and thus influence the lasing threshold. From this, two things are clear. Firstly, the structure of laser cavity itself is of importance and therefore careful consideration must be made for its optimal design. Secondly, as

Reproduced with permission of the copyright owner. Further reproduction prohibited without permission.

opposed to a calculation based on purely bandstructural means, the design of the cavity may be approached from the viewpoint of the propagating photon field.

A wide variety of theoretical techniques have been formulated in order to characterize the optical wave propagation in guiding structures, for which a simple analytical formulation cannot be found [74]. In particular, techniques such as the effective-index [75], weighted-index [76]. and variational lead to quick and intuitive results. For more complicated structures, numerical approaches such as the beam-propagation method [77] and spectral-index method [78] have been used. However, instances arise where the desired information exceeds what can be obtained by knowing only the propagating constant or mode profile of a complex structure. One might be interested in the behavior of the field at the end of a waveguide; an example of this may be a waveguide-to-optical fiber connection. Another example may be nonuniformites in the refractive index profile of the guide along the propagating direction of the field.

In order to study such problems, a formulation different from the ones previously mentioned must be invoked. In this chapter, a theoretical formalism is presented for finite-difference time domain (FDTD) models which can be used to investigate structures where arbitrary changes in the refractive index along the propagating direction exist. In the first section, the application of the FDTD theory to the Maxwell equations which govern optical mode propagation is given, and the slowly-varying envelope approximation is invoked to ease computational demands. Following this, the algorithms used in this study in calculations for structures in two-dimensions and three-dimensions are illustrated, followed by an example of the simulator's use. The goal, then, is to develop a simulator which can handle an arbitrary structure, yet can obtain results from use on a single workstation in a reasonably short amount

Reproduced with permission of the copyright owner. Further reproduction prohibited without permission.

of time. In Appendix C a method for a simulator which could be introduced for supercomputing (or multi-node) application is presented.

6.2 Background

The uncoupled Maxwell equation for the electric field, assuming a nondispersive, magnetically isotropic media with an absence of currents, can be written as

$$\nabla \times \nabla \times \mathbf{E}(\mathbf{r},t) = -\mu_0 \epsilon(\mathbf{r}) \mathbf{E}(\mathbf{r},t) \tag{6.1}$$

where $\mathbf{E}(\mathbf{r},t)$ is the time and spatially dependent electric field vector. μ_0 is the free space magnetic susceptibility, and $\epsilon(\mathbf{r})$ is the spatially varying dielectric permittivity. Assuming the absence of surface charges, i.e. $\nabla \cdot \ (\epsilon(\mathbf{r})\mathbf{E}(\mathbf{r},t)) = 0$, and using the vector identity $\nabla \times \nabla \times \mathbf{F} = \nabla(\nabla \cdot \mathbf{F}) - \nabla^2 \mathbf{F}$, Eq. (6.1) can be rewritten

$$\nabla^2 \mathbf{E}(\mathbf{r},t) + \nabla(\mathbf{E}(\mathbf{r},t) \cdot \nabla \ln \epsilon(\mathbf{r})) = \mu_0 \epsilon(\mathbf{r}) \frac{\partial^2 \mathbf{E}(\mathbf{r},t)}{\partial t^2}. \tag{6.2}$$

Above threshold in a single-mode semiconductor laser, the dominant electric field mode can be described by a narrow-band electromagnetic wave:

$$\mathbf{E}(\mathbf{r},t) = \mathcal{E}(\mathbf{r},t) e^{-i\omega_0 t}. \tag{6.3}$$

Assuming that the modulation frequency of the carrier is much smaller than the carrier frequency, the slowly-varying envelope approximation,

$$\left| \frac{\partial^2 \mathcal{E}}{\partial t^2} \right| << \omega_0 \left| \frac{\partial \mathcal{E}}{\partial t} \right|, \tag{6.4}$$

allows us to rewrite Eq. (2.2) as [79]

$$\frac{\partial \mathcal{E}(\mathbf{r},t)}{\partial t} = \frac{i\omega_0}{2} \left[\mathcal{E}(\mathbf{r},t) + \frac{1}{\omega_0^2 \mu_0 \epsilon(\mathbf{r})} \Big(\nabla[(\mathcal{E}(\mathbf{r},t) \cdot \nabla \ln \epsilon(\mathbf{r})] + \nabla^2 \mathcal{E}(\mathbf{r},t) \Big) \right]. \tag{6.5}$$

The form of Eq. (6.5) is known as a parabolic equation. In solving the time-dependent parabolic equation one generally resorts to either explicit-difference or

Reproduced with permission of the copyright owner. Further reproduction prohibited without permission.

implicit-difference methods. In general, explicit difference methods are generally unstable in the Von-Neumann sense (see Appendix B) as the error generated per time step may not be bounded as $t \rightarrow \infty$. Implicit methods, on the other hand, can be formulated such that the Von Neumann stability criterion is not violated. Therefore, the discussions that follow will center on using implicit difference approximations for solving Eq. (6.5).

As stated previously, the formalism (based on Eq. (6.5) in two and three dimensions is given. Since it is easier to conceptualize the two dimensional case, the formalism for two dimensions will be shown first, and then the implementation for three dimensions will be considered.

6.3 Studies in Two Dimensions

Many common three dimensional structures lend themselves nicely to studies in which only two dimensions need to be considered to provide accurate results. Two types of structures in this set are cylindical waveguides and slab waveguides. In the cylindrical waveguide, the azimuthal angle (ϕ) is considered invariant. In the slab waveguide, one transverse dimension is eliminated by assuming the change in the field along that direction is negligible in comparison with the other two dimensions. In this section the formalism for the cartesian 2-D system, attractive for its simple implementation and applicability in many devices, is given.

6.3.1 Formalism

Using the typical convention, the permeabililty is written as $\epsilon(\mathbf{r}) = \epsilon_0 n^2(\mathbf{r})$. Within the region of our interest it is assumed the index of refraction varies in only two dimensions, that is, $n(\mathbf{r}) = n(x, z)$. Further, it is assumed that the electric field varies slowly along the y-direction, i.e. $\partial \mathcal{E}/\partial y \sim 0$. After some algebraic

Reproduced with permission of the copyright owner. Further reproduction prohibited without permission.

manipulation, the equation for the TE mode, $\mathcal{E}_y$, can be written as

$$\frac{\partial}{\partial t}\mathcal{E}_y(x,z,t) = \frac{i\omega_0}{2}\Big[\mathcal{E}_y(x,z,t) + \frac{1}{\omega_0^2\mu_0\epsilon_0 n^2(x,z)}\Big(\frac{\partial^2}{\partial x^2} + \frac{\partial^2}{\partial z^2}\Big)\mathcal{E}_y(x,z,t)\Big]. \qquad (6.6)$$

Through Eq. (6.6) the propagation of a TE-polarized mode an arbitrary 2-D structure can be studied.

In a slab-waveguide structure, TE-polarized modes typically exhibit higher reflectivity than TM-polarized ones [80], and are therefore primarily supported in a semiconductor laser. With this in mind, this study is limited to observing propagation of TE-polarized waveguide modes. If $\mathcal{E}_y$ can be expressed as a linear combination of plane waves of the form $\exp(i\beta z - \omega t)$, β being a propagation constant, by assuming translational invariance in the z-direction, the wave equation can be separated in the longitudinal (z) and transverse (x) directions,

$$\mathcal{E}_y(x,z,t) = \chi(z,t)\phi(x). \qquad (6.7)$$

The expression is valid provided $\mathcal{E}_y(x, z = z_0, t = 0)$ is far away from the interfaces at the end of a uniform waveguide region [81], where z_0 is the initial starting point of the electromagnetic wave.

Since $\phi(x)$ is the transverse component of the electric field at $t = 0$, it can be found by solving the eigenvalue equation, obtained from Eq. (6.6) using the constraint that $\frac{\partial \mathcal{E}(x,z=z_0,t=0)}{\partial t} = 0$:

$$\frac{\partial^2\phi_0(x)}{\partial^2 x} + \omega_0^2\mu_0\epsilon_0 n^2(x)\phi_0(x) = \beta_0^2\phi_0(x). \qquad (6.8)$$

Here $\phi_0(x)$ and β_0 are the fundamental eigenmode and propagation constant associated with ω_0.

The Gaussian pulse is ideally suited for studying wave packet propagation since such a pulse maintains its shape propagating in the waveguide at some group velocity

Reproduced with permission of the copyright owner. Further reproduction prohibited without permission.

$\frac{c}{n_{eff}}$,n_{eff} being the effective index of refraction of the guide. A two-dimensional wave packet can then be constructed from a continuum of forward propagating plane waves centered around the eigenmode β_0 and the transverse mode profile ϕ_0

$$\mathcal{E}_y(x,z,t=0) = \phi_0(x)\int \exp\left(\frac{-(\beta-\beta_0)^2}{2(\Delta\beta)^2}\right)\exp(i\beta z)d\beta, \tag{6.9}$$

where $\Delta\beta$ is the spread in propagation constant β values. The wave packet then is a solution of the wave equation in the waveguide with a uniform index of refraction profile along the longitudinal axis.

A typical situation may be as follows. Consider a Fabry-Perot semiconductor laser cavity where the ends of the cavity are defined by a semiconductor/air interface. After some time t_r the wave packet is assumed to have reached the end of the waveguide. After a further time $t_r + \delta t$ a fraction of the wave packet will be transmitted into air and the remaining fraction of the wave packet will be reflected back into the guide (and cladding). The information desired in this situation is the wavepacket reflectivity. The formalism just presented can handle this problem. The next step is development for efficient computation.

6.3.2 Implementation

Finite difference numerical techniques are well known and well established in the microwave domain [82], and, more recently, in the optical domain [79],[83]. Since finite difference techniques are simple to implement and can be coded efficiently, a finite difference technique is chosen to implement the formalism developed in the previous section.

Initially the finite difference time-domain technique is defined on a rectilinear grid with sides parallel to the r- and t-axes. Each grid point is then given as ($r = m\Delta r, t = n\Delta t$). Discretizing the time variable, and assuming $\mathcal{E}$ is analytic for all

Reproduced with permission of the copyright owner. Further reproduction prohibited without permission.

time, the MacLaurin expansion of $\mathcal{E}$ can be written as [84]

$$\begin{aligned}\mathcal{E}(\mathbf{r},(n+1)\Delta t) &= \mathcal{E}^{n+1}(\mathbf{r}) \\ &= \left[1+\Delta t\frac{\partial}{\partial t}+\frac{(\Delta t)^2}{2}\frac{\partial^2}{\partial t^2}+\cdots\right]\mathcal{E}^n(\mathbf{r}). \qquad (6.10)\end{aligned}$$

This can be formally rewritten as

$$\mathcal{E}^{n+1}(\mathbf{r}) = \exp\left(\Delta t\frac{\partial}{\partial t}\right)\mathcal{E}^n(\mathbf{r}). \qquad (6.11)$$

Implicit differentiation techniques, despite an increase in computational difficulty in in many instances, are considered to be superior when compared to explicit formula in ensuring stability and convergence [85], [86]. The implicit formula involves more than one grid point at the advanced time level $t = (n+1)\Delta t$. Using the Pade' approximation [86], Eq. (6.11) can be rewritten

$$\left[1-\frac{\Delta t}{2}\frac{\partial}{\partial t}\right]\mathcal{E}^{n+1}(\mathbf{r}) = \left[1+\frac{\Delta t}{2}\frac{\partial}{\partial t}\right]\mathcal{E}^n(\mathbf{r}), \qquad (6.12)$$

which is of local truncation error $O(\Delta r^3+\Delta t^3)$. Referring back to Eq. (6.6), and calling the right side of the equation as $D(\mathbf{r})$, $D(\mathbf{r})$ is substituted for the time derivative into Eq. (6.12) and thus

$$\left[I-\frac{\Delta t}{2}D(\mathbf{r})\right]\mathcal{E}^{n+1}(\mathbf{r}) = \left[I+\frac{\Delta t}{2}D(\mathbf{r})\right]\mathcal{E}^n(\mathbf{r}), \qquad (6.13)$$

where I is the identity operator. Eq. (6.13) has been written in a matrix form because of finite difference implementation we consider.

The simplest and most brute-force methods in solving the matrix equation of Eq. (6.13) are the iterative Jacobi and Gauss-Seidel methods, and will be discussed in Section 6.4. A more elegant method, which is also computationally much faster, is the locally one-dimensional (LOD) scheme [86],[87]. In the LOD scheme, Eq. (6.6)

Reproduced with permission of the copyright owner. Further reproduction prohibited without permission.

is rewritten as a pair of equations

$$\frac{1}{2}\frac{\partial}{\partial t}\mathcal{E}_y(x,z,t) = \frac{i\omega_0}{2}\Big[\mathcal{E}_y(x,z,t) + \Big(\frac{1}{\omega_0^2\mu_0\epsilon_0 n^2(x,z)}\Big)\frac{\partial^2}{\partial x^2}\mathcal{E}_y(x,z,t)\Big], \quad (6.14)$$

$$\frac{1}{2}\frac{\partial}{\partial t}\mathcal{E}_y(x,z,t) = \frac{i\omega_0}{2}\Big[\mathcal{E}_y(x,z,t) + \Big(\frac{1}{\omega_0^2\mu_0\epsilon_0 n^2(x,z)}\Big)\frac{\partial^2}{\partial z^2}\mathcal{E}_y(x,z,t)\Big]. \quad (6.15)$$

In advancing a calculation from $t = n\Delta t$ step to $t = (n+1)\Delta t$, the assumption is Eq. (6.14) holds from $t = n\Delta t$ to $t = (n+\frac{1}{2})\Delta t$, and, Eq. (6.15) helds from $t = (n+\frac{1}{2})\Delta t$ to $t = (n+1)\Delta t$.

In a FDTD calculation it is desired that the method provides stability; that is, that is, the error remains bounded for all time. A Von Neumann stability analysis of Eqs. (6.14) and (6.15) (see Appendix B) shows that the LOD scheme represented is *not* uncondtionally stable. However, by making the substitution $U(x,z,t) = \mathcal{E}_y(x,z,t)e^{-\frac{i\omega_0 t}{2}}$, Eqs. (6.5), (6.14), and (6.15) transform to

$$\frac{\partial}{\partial t}U(x,z,t) = \frac{i}{2\omega_0\mu_0\epsilon_0 n^2(x,z)}\Big(\frac{\partial^2}{\partial x^2} + \frac{\partial^2}{\partial z^2}\Big)U(x,z,t), \quad (6.16)$$

$$\frac{1}{2}\frac{\partial}{\partial t}U(x,z,t) = \frac{i}{2\omega_0\mu_0\epsilon_0 n^2(x,z)}\frac{\partial^2}{\partial x^2}U(x,z,t). \quad (6.17)$$

$$\frac{1}{2}\frac{\partial}{\partial t}U(x,z,t) = \frac{i}{2\omega_0\mu_0\epsilon_0 n^2(x,z)}\frac{\partial^2}{\partial z^2}U(x,z,t) \quad (6.18)$$

Eqs. (6.17) and (6.18), with the Von Neumann stability analysis applied locally (ie. where $n(x,z)$ is constant), is unconditionally stable (see Appendix A).

The forms of Eq. (6.17) and Eq. (6.18) allows for the use of a tri-diagonal matrix in solving Eq. (6.13) for $\mathcal{U}^{n+1}(\mathbf{r})$. Efficient routines for solving tri-diagonal systems are readily available; a standard solver from the LINPACK family of numerical algorithms is chosen.

6.3.3 Improvements for Fast Computation

In addition to the stability improvement presented above for this LOD scheme, a number of other optimizations were made in order to elicit faster computatation.

Reproduced with permission of the copyright owner. Further reproduction prohibited without permission.

Briefly described in the next sections are a few important ones.

6.3.3.1 Variable Finite-Differences

The finite-difference expansions of the derivatives $\partial f/\partial z$ and $\partial^2 f/\partial x^2$, for a function f to second order are

$$\frac{\partial f}{\partial x} \rightarrow \frac{f(x+\Delta x) - f(x-\Delta x)}{2\Delta x}, \tag{6.19}$$

$$\frac{\partial^2 f}{\partial x^2} \rightarrow \frac{f(x+\Delta x) - 2f(x) + f(x-\Delta x)}{(\Delta x)^2}. \tag{6.20}$$

Here Δx is the spacing between mesh points along the x-direction. Although computationally simple, an equal mesh spacing compromises the flexibility of the simulator. For example, assume that the region of interaction of a propagating wave is narrow compared with the total width of a structure or desired simulation region, as may be the case with a narrow guiding region in a laser structure. In this example, for accurate calculations a small mesh spacing in the interaction region is desirable. However, if the simulation region itself is large, a small mesh pitch results in a large number of meshpoints, which in turn results in large memory requirements and a reduction in computation speed. This situation can be avoided if the mesh pitch is variable, i.e. the mesh spacing remains small within the primary region of interaction and increases in size as the distance increases from this narrow region. In this case, the finite-difference expansions of the derivatives are

$$\frac{\partial f}{\partial x} \rightarrow \frac{k}{h(h+k)} f(x+h) - \frac{h}{k(k+h)} f(x-k) - \frac{k-h}{hk} f(x) \tag{6.21}$$

$$\frac{\partial^2 f}{\partial x^2} \rightarrow \frac{2kf(x+h)}{k+h} + \frac{2hf(x-k)}{k+h} - \frac{f(x)}{hk}, \tag{6.22}$$

where h represents the distance $x_1 = x + h$ and k represents the distance $x_2 = x - k$ so that $f(x_1) = f(x+h)$ and $f(x_2) = f(x-k)$.

Reproduced with permission of the copyright owner. Further reproduction prohibited without permission.

Figure 6.1 shows a visual structure. In a structure such as that in Fig. 6.1. the core region's small transverse dimension demands a small mesh spacing in that region. If the mesh pitch is small, a prohibitively large number of points are needed to discretize the refractive index profile of the entire simulation region. However, if the spacing between mesh points can be varied, the number of mesh points need to discretize the transverse dimension can be reduced markedly. In Fig. 6.1 the structure is assumed symmetric about a 0.1μm core, with a 2.0μm inner clad and a 2.0μm outer clad, terminated by a 0.5μm absorbing boundary. The mesh pitch Δ is chosen as 0.01μm, to provide enough mesh points in the region of interest (the core). If a constant mesh spacing is chosen, 910 points will be needed to discretize the guide along the transverse direction. However, if a variable mesh spacing is implemented, such as in the example given in Fig. 6.1, only 218 points are necessary, a considerable reduction. Noted here is that the mesh pitch never changes at the boundary between two differing layers (i.e. refractive indices). Instead, the mesh pitch only changes within a dielectric layer. This is done to satisfy the Von Neumann stability criterion when applied locally (within a single dielectric layer).

6.3.3.2 Symmetry Considerations

In many cases a waveguide structure may be under study where the structure exhibits symmetry. In Fig. 6.2(a) an example of a symmetric waveguide is shown and in Fig. 6.2(b) is the initial wavepacket injected into the waveguide.

Due to the symmetry of the waveguide one expects a likewise symmetrical behavior of the propagating wavepacket about the center of the guide. Such a symmetry is mathematically represented simply as

$$\left.\frac{\partial \mathcal{E}}{\partial x}\right|_{x=x_{center}} = 0. \tag{6.23}$$

Reproduced with permission of the copyright owner. Further reproduction prohibited without permission.

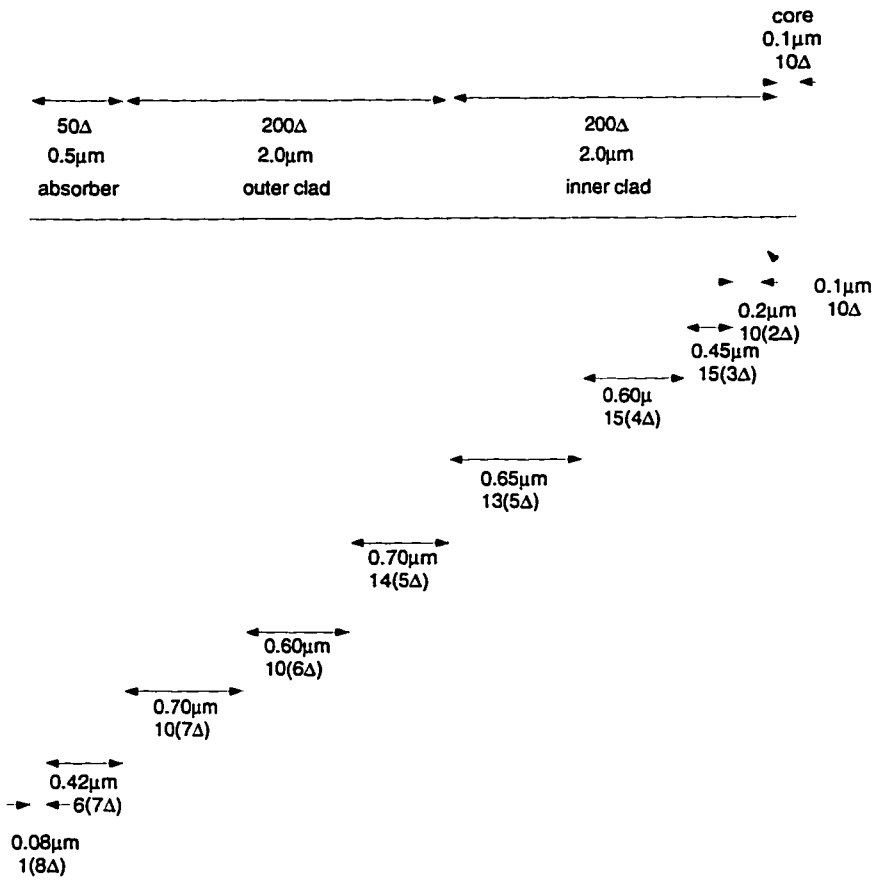
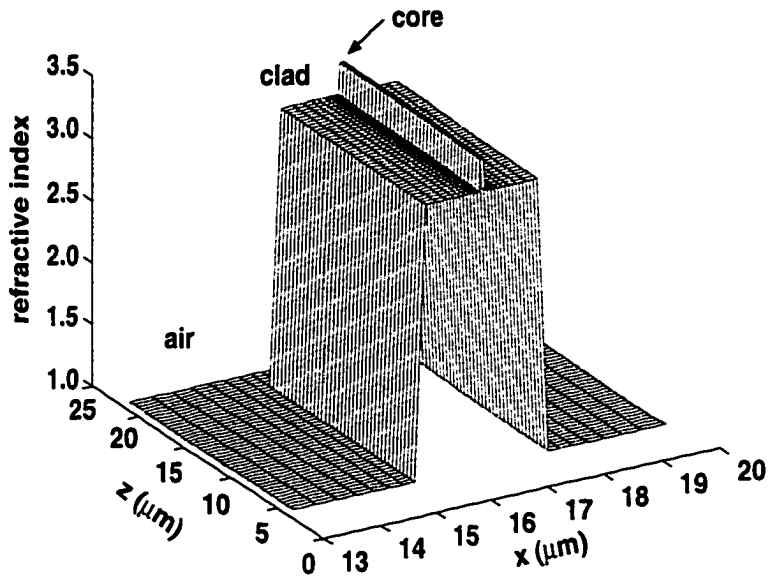
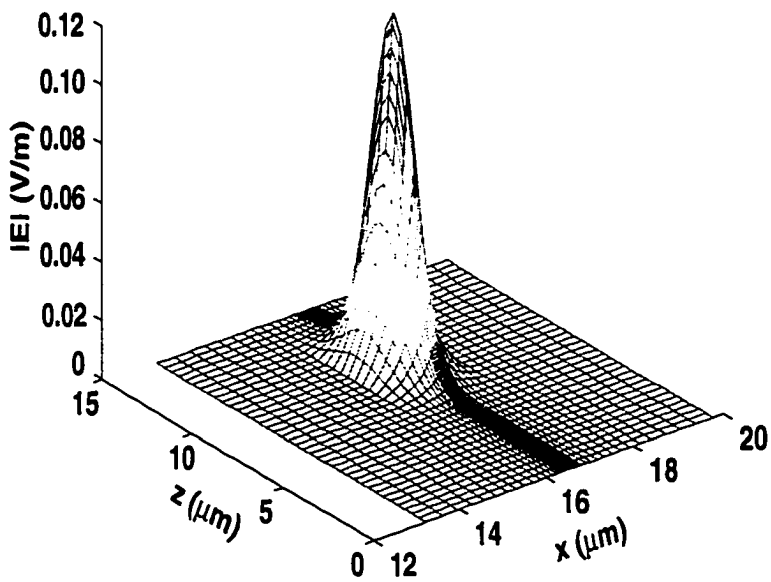


Figure 6.1: Constant and variable mesh spacings for a symmetric waveguide about a core of 0.1 μm.

Reproduced with permission of the copyright owner. Further reproduction prohibited without permission.



(a)



(b)

Figure 6.2: (a) A symmetric waveguide and (b) the initial wavepacket injected into the waveguide.

Reproduced with permission of the copyright owner. Further reproduction prohibited without permission.

This is known as a Neumann condition [86] and is often found in heat-transfer problems where there exists zero temperature change across a boundary. Equation (6.23) states about the symmetry axis $x = x_{center}$, $\mathcal{E}(x_{center} - \Delta x) = \mathcal{E}(x_{center} + \Delta x)$. Obviously, imposition of the condition results in a tremendous memory savings, as only $\frac{1}{2}$ of the actual simulation region need be examined without a loss of information.

Implementation of the Neumann condition here is straightforward. For the finite-difference expansion as given in Eq. (6.20), at the boundary $x = x_{center}$, the expansion for $\partial^2 f/\partial x^2$ becomes

$$\frac{\partial^2 f}{\partial x^2} = \frac{2f(x_{center} - \Delta x) - 2f(x_{center})}{(\Delta x)^2}. \tag{6.24}$$

6.3.3.3 Boundary Termination

In the real world the physical region upon which the simulation model is based upon extends far beyond the limits of the boundaries present in the actual simulation. Obviously, limitations due to finite memory and computation speed forces one to consider how to truncate the simulation region without unphysical effects occurring.

The simulation region is defined such that a Dirichlet condition [86] is imposed at the boundaries. That is,

$$\mathcal{E}(0, z) = \mathcal{E}(x_{max}, z) = \mathcal{E}(x, 0) = \mathcal{E}(x, z_{max}) = 0. \tag{6.25}$$

This implies the wavepacket amplitude $|\mathcal{E}|$ must be such that the Dirichlet condition does not introduce a large error as time increases. In other words, one would like to keep the wavepacket as far from the boundaries as possible.

Of course, keeping the wavepacket far from the simulation edges is a challenge using a small simulation region. A major concern is that any portion of the wavepacket encountering a boundary is entirely reflected back into the simulation region. Such a

Reproduced with permission of the copyright owner. Further reproduction prohibited without permission.

scenario is undesirable, say, when calculating the reflectivity of semiconductor/air interface, in which one does not want the transmitted portion of the incident wavepacket to be reflected back into the semiconductor waveguide by the simulation region.

One method used to counteract this dilemma is to use an absorbing boundary [88]. This involves adding an appropriate imaginary amount n_i to the now complex refractive index $n_r + in_i$ of an area of dielectric nearest to the boundary. The greater n_i is, the faster an impinging wave will be absorbed. However, if n_i is made too large, the reflection coefficient at a dielectric/absorber boundary becomes undesirably large, since $R = n_i^2/(4n_r^2 + n_i^2)$. Figure 6.3(a) plots the reflectivity at an absorber/dielectric interface as a function of n_i assuming $n_r = 1.0$ (air). Figure 6.3(b) shows the fraction of wave energy ($\sim e^{-\frac{4\pi n_i}{\lambda}d}$) remaining after the wave has penetrated into the absorber a distance $d = 1\mu m$. During a simulation the actual value for n_i, then, depends on the constraints presented by the simulation edges.

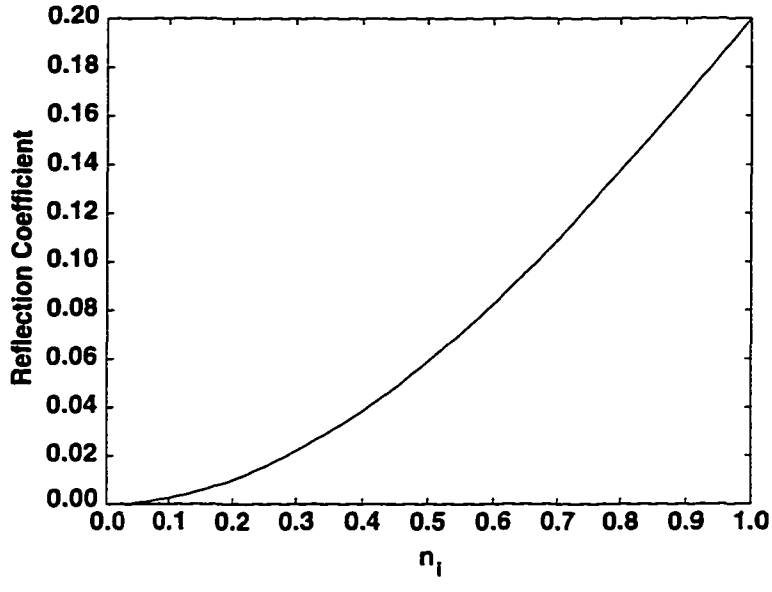
The absorbing boundary described in the previous paragraph used a constant value of n_i in the absorbing dielectric. There may be instances where the rate of absorption, given the thickness of the fictitious absorber, is not fast enough using a constant n_i. In these cases a material whose absorption coefficient increases with penetration distance can be implemented. An example of such a formulation may be

$$n_i(x + m\Delta x) = 1.1^m n_i(x) \tag{6.26}$$

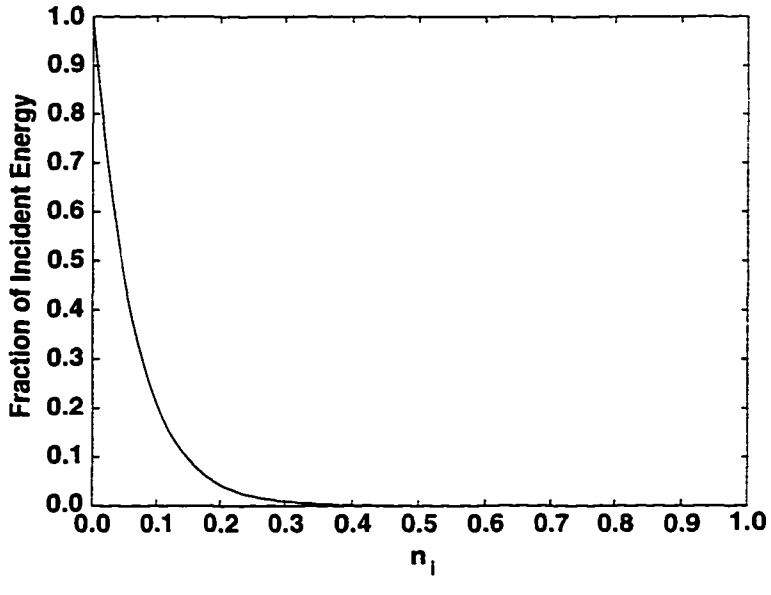
where each succeeding mesh point is spaced Δx away from the preceding one. In this example, the absorption increases by approximately 10% every mesh point, yet the reflection coefficient R_{cons} between consective mesh points remains small, as $R_{cons} = 0.01n_i^2/(4n_r^2 + 4.41n_i^2)$.

Finally, for completeness, it should be noted there exists a class of absorbers ex-

Reproduced with permission of the copyright owner. Further reproduction prohibited without permission.



(a)



(b)

Figure 6.3: (a) Reflection coefficient and (b) fraction of absorbed energy of an incident wavepacket at an air/absorber interface ($n_r = 1.0$) as a function of n_i.

Reproduced with permission of the copyright owner. Further reproduction prohibited without permission.

hibiting characteristics known as perfectly absorbing boundary conditions [88],[89],[90]. These rely on manipulating the equations for Faraday's law and Ampere's law so that a relation for ϵ can be derived resulting in a nearly perfect absorption (a reduction in wave amplitude $\sim 10^6$) at the boundaries. Application of this type of absorber to the present formulation is not as straightforward simply introducing a complex refractive index. Interested readers may refer to the works cited earlier.

6.3.4 Application

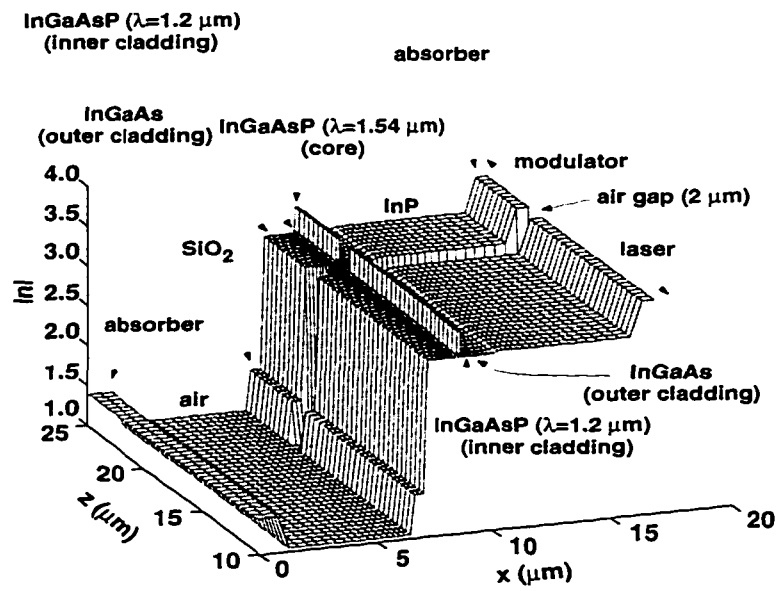
The two-dimensional simulator described was used in the study of an 1.54μm integrated laser-modulator made with one-step reactive ion etching [93],[94]. Such devices are often used in optoelectronic integrated circuits because of compactness, low loss, and low cost. Since these types of integrated circuits can incorporate several complex waveguide structures, it is useful to be able to obtain information about the spatial and dynamic behaviors of the propagating waves in the waveguides. In this case, the technique was used to simulate the propagation of an optical wave launched in the laser and to determine the reflectivity of the facets of the laser-modulator coupling region. The technique can not only be used in predicting the reflectivity of the coupling region but can also be used in characterizing the roughness of the etch as well [81].

The laser heterostructure is given in Fig. 6.4(a), and in Fig. 6.4(b) is the refractive index profile for the laser-modulator. The coupling gap in this device is designed to be $\sim 2\mu$m, so that the Bragg condition can be fulfilled for the near-1.5μm wavelength. Scanning electron micrographs examining the fabricated device and the coupling region of the etched laser-modulator (fabricated by the author's colleague Ya-hsing Yuan) are given in Fig. 6.3.4 [93].

Reproduced with permission of the copyright owner. Further reproduction prohibited without permission.

0.1 μm	In0.53Ga0.47As	p^+ (3×10^{19} cm^{-3})
0.1 μm	InGaAsP	p ($2\times10^{18}cm^{-3}$)
0.9 μm	InP	p ($2\times10^{18}cm^{-3}$)
0.2 μm	InP	p ($2\times10^{17}cm^{-3}$)
500 Å	InGaAsP (λ=1.2 μm)	i
8 Period MQW's	InGaAsP Well, (L_w=80 Å, λ_{PL}=1.54 μm, ε=+0.38%)	i
	InGaAsP Barrier, (L_b=100 Å, λ_g=1.2 μm, ε=-0.303%)	i
500 Å	InGaAsP (λ=1.2 μm)	i
1.1 μm	InP	n ($5\times10^{17}cm^{-3}$)
0.1 μm	InGaAsP	n ($5\times10^{17}cm^{-3}$)
0.2 μm	$In_{0.53}Ga_{0.47}As$	n^+ ($5\times10^{18}cm^{-3}$)
	S. I. InP (100) Substrate	

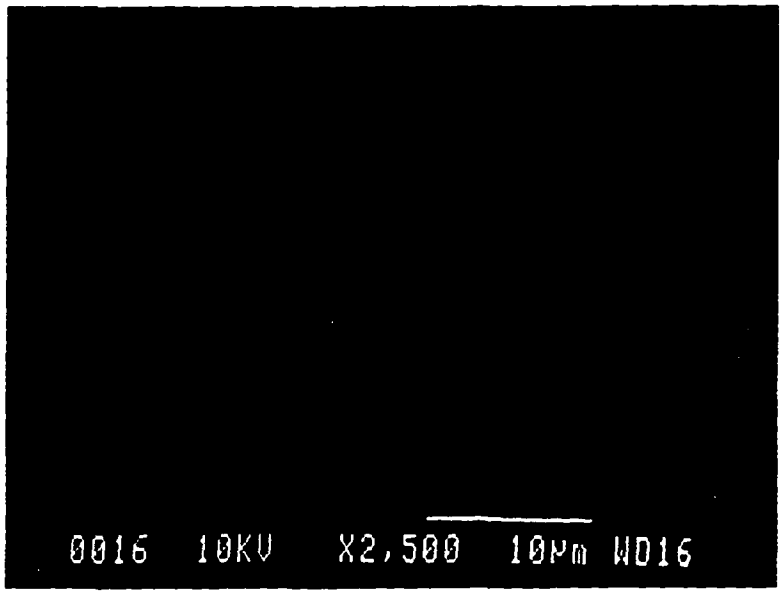
(a)



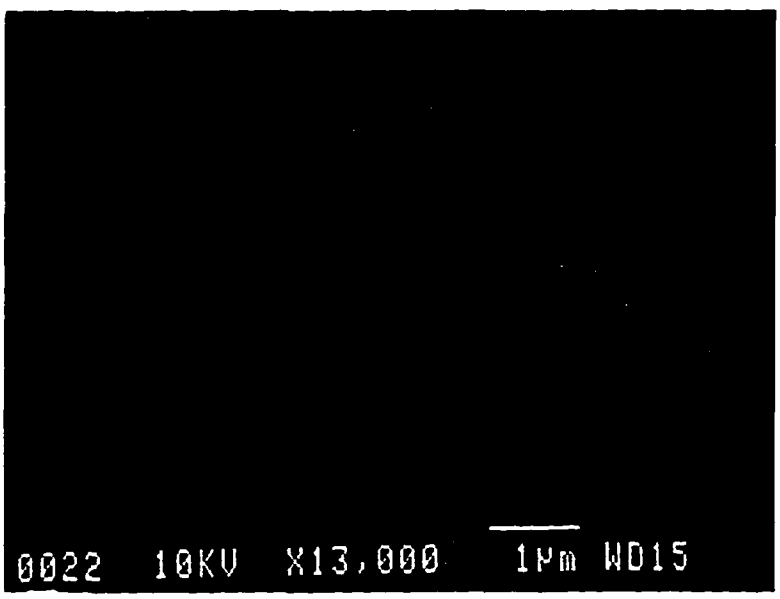
(b)

Figure 6.4: (a) Layer structure and (b) refractive index profile of the 1.54μm laser-modulator.

Reproduced with permission of the copyright owner. Further reproduction prohibited without permission.



(a)



(b)

Figure 6.5: Scanning electron micrographs of (a) the fabricated laser-modulator and (b) the coupling region.

Reproduced with permission of the copyright owner. Further reproduction prohibited without permission.

The properties of the etched facets are first examined by the simulator. The injected wavepacket, shown in Fig 6.6(a), launched in the laser section of the integrated structure, assumed to have the slab waveguide configuration. After some time the wavepacket has reached the end of the guide, at which point the some of the wavepacket energy is reflected and the rest is transmitted into the air gap. From the transmitted energy, a part is reflected at the second etched surface and the remainder propagates within the second guide. This is shown in Fig. 6.6(b). The scattering loss is assumed to be small, while the etched walls are assumed to be perfectly abrupt. After sufficient time has elapsed the final reflected wave in the first guide is clearly seen in Fig. 6.6(c).

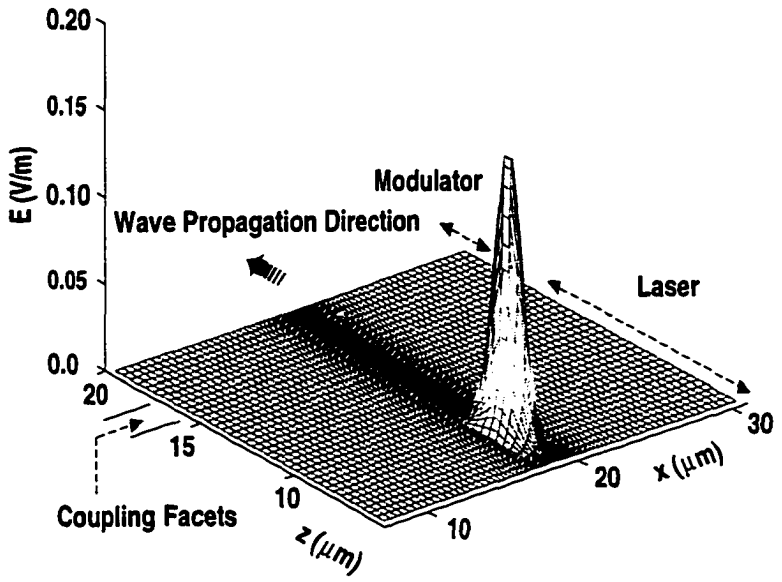
The effective reflectivity of the coupling region is a function of the air gap distance, and moves from maximum to minimum as the gap distance changes by a quarter-wavelength. From the simulation results the reflectivity versus gap distance is plotted in Fig. 6.7 Such information is important in characterizing the etch since fine variation in the gap distance is generally not controllable by optical lithography and RIE etching processes. From SEM examinations, the gap size d_g is estimated as $d_1 < d_g < d_2$, where d_1=2.05μm and d_2=2.15μm. The effective reflectivity for this range in gap distance is calculated to be between 0.45 and 0.55, and is represented as the dashed portion of the effective reflectivity curve in Fig. 6.7.

From experimental data, the reflectivity of the etched mirrors can be obtained via [96],[97]

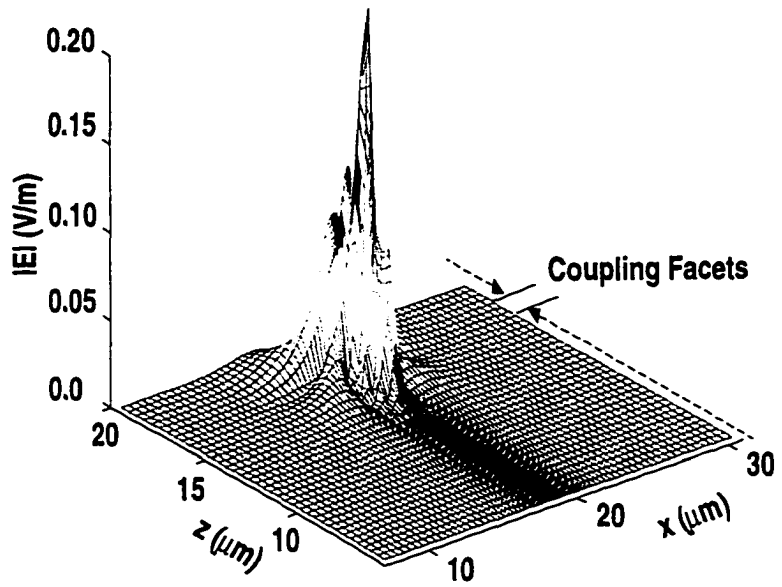
$$J_{th} = \frac{J_0}{\eta_{in}} exp\{\frac{1}{\Gamma\beta J_0}[\alpha_{in} + \frac{1}{2l} ln(\frac{1}{R_{cleave} R_{etch}})]\} \tag{6.27}$$

where J_0 is the transparency current density, η_{in} is the internal quantum efficiency, α_{in} is the cavity loss, Γ is the confinement factor, β is the gain coefficient near the transparency current density, l is laser cavity length, R_{cleave} is taken as 0.32, and

Reproduced with permission of the copyright owner. Further reproduction prohibited without permission.



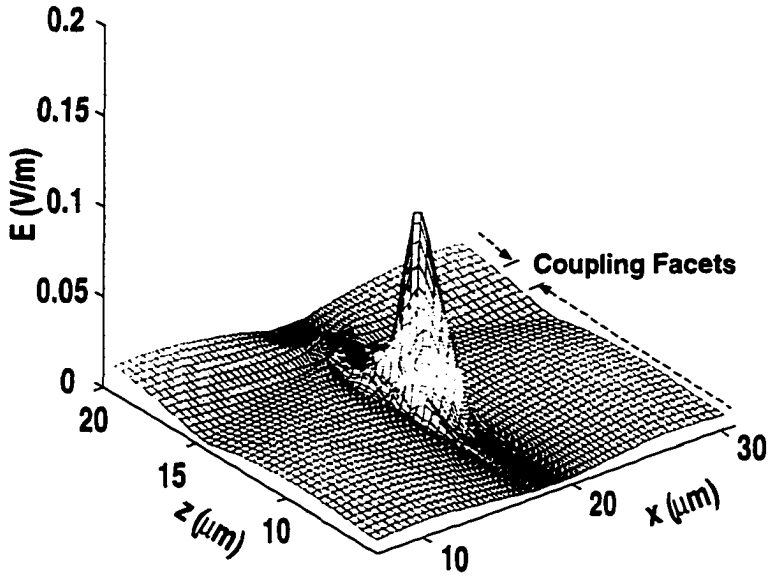
(a)



(b)

Figure 6.6: Wavepacket propagation in the laser cavity of the integrated laser-modulator: (a) initial wavepacket injected into the laser cavity, (b) profile of wavepacket at the coupling facets.

Reproduced with permission of the copyright owner. Further reproduction prohibited without permission.



(c)

Figure 6.6: Wavepacket propagation in the laser cavity of the integrated laser-modulator: (c) steady-state mode profile of the wavepacket in the laser cavity after reflection.

R_{etch} is the effective reflectivity of the etched and coupled facets. Figure 6.8 shows a plot of threshold current density versus inverse cavity length measured for a ridge waveguide laser with one cleaved and one etched facet in the integrated structure. From the slope of the latter dependence, the effective reflectivity is estimated to be in the range 0.5 – 0.55, which is very close to the value obtained from the simulation described above.

The reflectivity of a single etched facet can be derived from coupled cavity waveguide theory [61] by virtue of the equation

$$R_{etch} = r - \frac{r(1-r^2)t_g}{1-r^2t_g} \tag{6.28}$$

where t_g, which accounts for the phase shift and the loss experienced by the optical

Reproduced with permission of the copyright owner. Further reproduction prohibited without permission.

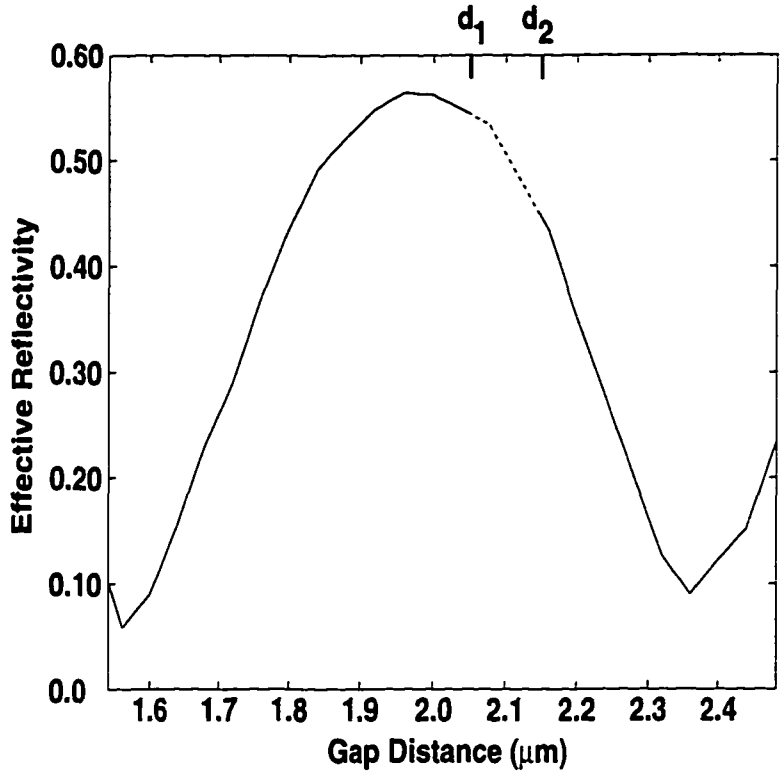


Figure 6.7: Effective reflectivity versus gap distance for the laser-modulator. The dashed portion of the curve indicates the effective reflectivity for the estimated value of d_g.

field during a round trip in the air gap, is given by

$$t_g = exp(2ik_0L_g)exp(-\alpha_gL_g) \tag{6.29}$$

Here the etched gap reflectivity is taken from simulation as 0.5, r is the reflectivity of the electric field at the single etched facet, k_0 is the wave number in the air gap, L_g is the air gap length, and α_g is the loss in the air gap. Again, in this equation, it is assumed that there is no reflected wave from the other end of the coupled waveguide. In addition, it is assumed there is no loss in the air gap, i.e. α_g=0. By substitution of the appropriate values of these parameters in the Eq. 6.29, the reflectivity of the etched facet is calculated as $R_{etch} = r^2 \simeq 0.3$. This is very close to the value of 0.32 assumed for the semiconductor/air cleaved facet and is further evidence of the

Reproduced with permission of the copyright owner. Further reproduction prohibited without permission.

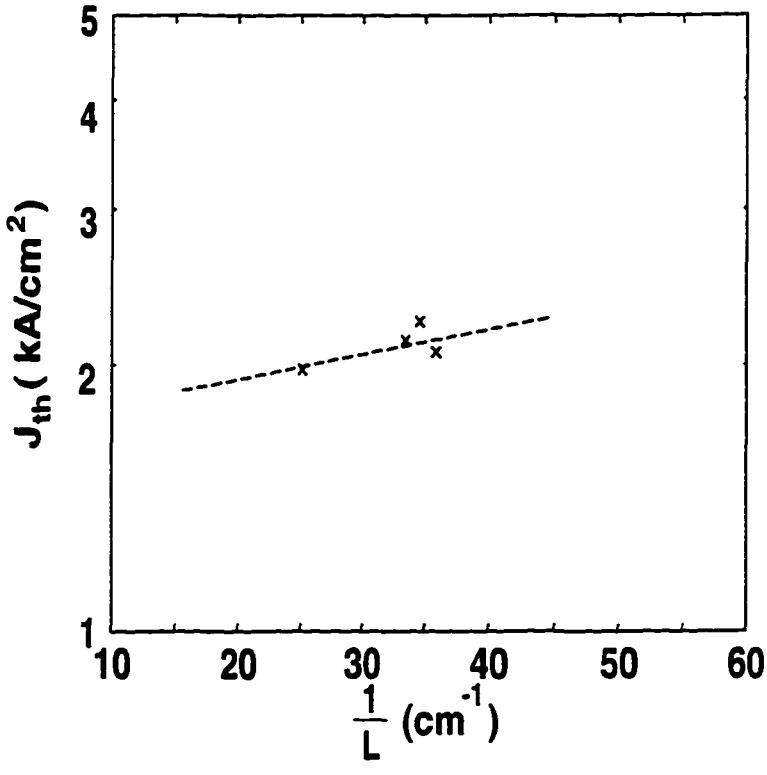


Figure 6.8: Threshold current density versus inverse cavity length characteristics for the 1.54μm integrated laser-modulator.

high-quality interface produced by RIE.

To summarize this section, a simulator which can simulate the propagation of an electromagnetic wave in two dimensions has been described and implemented. The simulator has been applied toward the design of an integrated laser-modulator. Experimentally measured reflectivity of the coupling region agrees well with the experimental data, and therefore indicates that the simulator can be used in future analysis and development of novel structures. In Chapter VII the use of the 2D simulator toward the design of a distributed Bragg reflector stack for an edge-emitting laser will be investigated.

Reproduced with permission of the copyright owner. Further reproduction prohibited without permission.

6.4 Studies in Three Dimensions

It is evident from Section 6.3 that a variety of problems can be addressed with in a two-dimensional context. However, for geometries in which one transverse dimension cannot be conveniently excluded from analysis, such as in microcavity structures, waveguide structures with submicron guiding regions, and ring cavities a simulator which can incorporate both transverse directions is desirable. Using the formalism of Section 6.3 as a basis, the development of such a three-dimensional simulator is described in the next sections.

6.4.1 Formalism

It is convenient to begin by expanding Eq. (6.5) explicitly in terms of the vectors $\mathcal{E}_x$,$\mathcal{E}_y$,and $\mathcal{E}_z$. The equation for the x-polarization is

$$\begin{aligned}\frac{\partial \mathcal{E}_x}{\partial t} &= \frac{i\omega_0}{2}\mathcal{E}_x + \frac{i}{2\omega_0\mu\epsilon}\Big(\frac{\partial \mathcal{E}_x}{\partial x}\frac{\partial \ln\epsilon}{\partial x} + \mathcal{E}_x\frac{\partial^2 \ln\epsilon}{\partial x^2} + \frac{\partial \mathcal{E}_y}{\partial x}\frac{\partial \ln\epsilon}{\partial y} + \\ &\quad \mathcal{E}_y\frac{\partial^2 \ln\epsilon}{\partial x\partial y} + \frac{\partial \mathcal{E}_z}{\partial x}\frac{\partial \ln\epsilon}{\partial z} + \mathcal{E}_z\frac{\partial^2 \ln\epsilon}{\partial x\partial z} + \frac{\partial^2 \mathcal{E}_x}{\partial x^2} + \frac{\partial^2 \mathcal{E}_x}{\partial y^2} + \frac{\partial^2 \mathcal{E}_x}{\partial z^2}\Big), \quad (6.30)\end{aligned}$$

and the parabolic equations for $\mathcal{E}_y$ and $\mathcal{E}_z$ are similar. It is seen that energy is exchanged between polarizations due to coupling terms arising from changes in the refractive index, such as at the core/clad boundary in a waveguide.

Although the problem is conceptually straightforward, it is challenging due to the necessity of solving for $\mathcal{E}_x$,$\mathcal{E}_y$, and $\mathcal{E}_z$ simultaneously. Writing Eq. (6.13) as a matrix equation in a basic form

$$P_+(\mathbf{r})\mathcal{E}^{n+1} = P_-(\mathbf{r})\mathcal{E}^n, \quad (6.31)$$

where n represents the n^{th} timestep, and P_+ and P_- are given as

$$P_+ = \Big[I - \frac{\Delta t}{2}D(\mathbf{r})\Big] \quad (6.32)$$

Reproduced with permission of the copyright owner. Further reproduction prohibited without permission.

$$P_- = \left[I + \frac{\Delta t}{2} D(\mathbf{r})\right] \tag{6.33}$$

and will be referred to as the propagators. Because the coupling only occurs at refractive index boundaries, P_+ and P_- are sparse. The obvious solution to the Eq. (6.31) then is

$$\mathcal{E}^{n+1} = (P_+^{-1} P_-)^n \mathcal{E}^1. \tag{6.34}$$

Unfortunately, in general the inverse of a sparse matrix is a dense matrix, and cannot be solved in any particularly efficient manner.

An approach often used in solving large sets of simultaneous equations is an iterative method. The sparse nature of the P_- matrix allows $P_-\mathcal{E}^m$ to be a low cost computation. The vector $\mathcal{E}^{m+1}$ is then found using an iterative technique. Iterative techniques implemented are usually optimized for each particular problem. In the next sections characteristics of the iterative method implemented in this study for solving problems of interest will be detailed.

6.4.2 Implementation

6.4.2.1 Iterative Methods

In solving the problem at hand, which can be written in a general form $Ax = b$, the most basic approach is the Jacobi iterative [85]. Here x is solved for using m successive approximations

$$x^m = -D^{-1} T x^m + D^{-1} b, \tag{6.35}$$

where D and T are the diagonal and off-diagonal terms of the matrix $A = D + T$. An improvement on the Jacobi iterative is the Gauss-Seidel iterative, in which it is assumed using the computed approximations $x_1^m \ldots x_{i-1}^m$ will lead to faster convergence to x_i^m than using $x_1^{m-1} \ldots x_{i-1}^{m-1}$. In this manner, the successive approximation is

$$x^m = (I - L)^{-1} U x^{m-1} + (I - L)^{-1} b. \tag{6.36}$$

Reproduced with permission of the copyright owner. Further reproduction prohibited without permission.

where I, L , and U represent the identity matrix, lower triangle matrix, and upper triangle matrix from $A = I - L - U$. The convergence of the Jacobi and Gauss-Seidel methods is guaranteed when A is diagonally dominant,

$$|a_{ii}| > \sum_{j=1, j\neq 0}^{n} |a_{ij}| \tag{6.37}$$

In addition, if A is diagonally dominant, the error after k^{th} approximation satisfies

$$|x^k - x| \sim \rho((I - L)^{-1}U)^k |x^0 - x| \tag{6.38}$$

where $\rho(A)$ is the spectral radius of A.

Equation (6.38) implies that as the spectral radius of A decreases, the error after k iterations decreases. The question then arises as to how to minimize the number of iterations necessary for convergence within some desired tolerance. Successive over-relaxation, in the spirit of the first-order perturbation theory described in Chapter II, is one method often implemented to improve convergence speed.

6.4.2.2 Successive Overrelaxation

Starting with Eq. (6.36), a variable x'_{i+1} is introduced, such that

$$x'_{i+1} = Lx_{i+1} + Ux_i + b, \tag{6.39}$$

where

$$x_{i+1} = \omega x'_{i+1} + (1 - \omega)x_i, \tag{6.40}$$

where ω is known as the relaxation factor. Three distinct cases arise: overrelaxation ($\omega > 1$), Gauss-Seidel ($\omega = 1$), and underrelaxation ($\omega < 1$). Elimination of x'_{i+1} above leads to

$$x_{i+1} = (I - \omega L)^{-1}[\omega U + (1 - \omega)I)x_i + \omega(I - \omega L)^{-1}b. \tag{6.41}$$

Reproduced with permission of the copyright owner. Further reproduction prohibited without permission.

Similar to Eq. (6.38), the convergence of the successive overrelaxation method is guaranteed if and only if

$$\rho(I-\omega L)^{-1}[\omega U+(1-\omega)I]<1 \tag{6.42}$$

Since the convergence and rate of convergence depend on the arbitrary parameter ω, it is necessary to find an optimal overrelaxation factor ω_0. If

$$M_\omega=(I-\omega L)^{-1}[\omega U+(1-\omega)I) \tag{6.43}$$

and λ is an eigenvalue of $M_\omega w$, then $|M_\omega-\lambda I|=0$. It can be shown that ω_0 can be discovered by finding the maximum eigenvalue of L_ω, λ_0, and minimizing λ_0 with respect to ω_0 [85],[86]. The study of finding ω_0 is an involved one and is thoroughly examined in the literature [91],[92]. Therefore, a brief example on choosing ω_0 will be presented here. Given a symmetric, two-cyclic, and consistently ordered matrix A, the overrelaxation factor λ_0 can be found by the following procedure:

(i) calculate $\lambda_0=\rho(L+U)$ which satisfies $0<\lambda_0<1$,

(ii) obtain the optimum overrelaxation factor ω_0

$$\omega_0=\frac{2}{1+(1-\lambda_0^2)^{0.5}} \tag{6.44}$$

The solution to the 1-D heat conduction equation can illustrate this procedure. Given the heat conduction equation $\frac{\partial\psi}{\partial t}=\frac{\partial^2\psi}{\partial x^2}$, the implicit formulation from Section 6.3

Reproduced with permission of the copyright owner. Further reproduction prohibited without permission.

results in a propagator matrix

$$I-L-U=\begin{bmatrix} 1 & \frac{-r}{2(1+r)} & 0 & \dots & 0 & 0 \\ \frac{-r}{2(1+r)} & 1 & \frac{-r}{2(1+r)} & \dots & 0 & 0 \\ 0 & \frac{-r}{2(1+r)} & 1 & \dots & 0 & 0 \\ & & & \vdots & & \\ & & & \vdots & & \\ 0 & 0 & 0 & \dots & \frac{-r}{2(1+r)} & 1 \end{bmatrix}, \tag{6.45}$$

where $r=\frac{\Delta t)}{(\Delta x)^2}$ The eigenvalues of $(L+U)$ are given by [86]

$$\lambda=\frac{r}{1+r}\cos(\frac{p\pi}{N}), \tag{6.46}$$

where N is the order of the matrix and $p=1\dots 2N-1$, and the maximum eigenvalue is therefore

$$\lambda_{max}=\frac{r}{1+r}cos(\frac{\pi}{N}). \tag{6.47}$$

From this, the optimum overrelaxation factor is [86]

$$\omega_0=\frac{2}{1+[1-(\frac{r}{1+r})^2\cos^2(\frac{\pi}{N})]^{0.5}} \tag{6.48}$$

Of course, in the three-dimensional problem first formulated, the matrices P_+ and P_- are not symmetric and two-cyclic, since neither the mesh pitch nor the refractive index profile need be constant. Because of this, the determination of ω is found most often by empirical methods. Obviously, good initial guesses for optimal values of ω_0 speed up the search. In this study a good value for ω_0 was found by defining a parameter r' analogous to the parameter r above and examining Eq. (6.30), leading to

$$r'\sim\frac{i\Delta t}{2\omega_0\mu\epsilon_0\frac{1}{3}((\Delta x)^2+(\Delta y)^2+(\Delta z)^2)}. \tag{6.49}$$

Reproduced with permission of the copyright owner. Further reproduction prohibited without permission.

In a similar vein, Eq. (6.48) is now

$$\omega_0 = \frac{2}{1 + [1 - (\frac{1}{1+n^2(\mathbf{r})/r'})^2]^{0.5}}, \tag{6.50}$$

where $n((\mathbf{r}))$ is specifically included so that ω_0 is optimally chosen for each region. Although in choosing ω the cited references do not explicitly treat overrelaxation using complex analysis, a complex ω_0 did succeed in greatly reducing the number of iterations for successive time steps. It has been shown that the use of a complex Pade' coefficient lends stability in terms of the propagation of the power in a mode [101], which may be an added bonus to using a complex value of ω_0. In addition, the banded nature of the propagator matrices appears to itself well to this treatment.

6.4.2.3 Mesh Traversal

In the previous sections there has been no statement made about how the mesh is traversed. The simplest form of traversal is simply sweeping across the mesh from $\mathcal{E}_p(0,0,0)$ to $\mathcal{E}_p(x_{max}, y_{max}, z_{max})$ in a column-by-column form. However, traversal algorithms exist which, upon implementation, can greatly accelerate convergence. In this study, one a traversal algorithm known as the cyclic Chebyshev method [99] was used. Here the mesh is swept like a checkerboard, with all of the red squares being analyzed in the first iteration, all of the black ones on the second iteration, the red ones in the third iteration, etc. In the present analysis considered the x-y plane is assumed to be the checkerboard, while the z- axis is traversed in an even-odd manner. For the cyclic Chebyshev method, the optimal overrelaxation factor was modified to

$$\omega_0 = \frac{2}{1 + \sqrt{1 - r'/n^2(\mathbf{r})}}. \tag{6.51}$$

Reproduced with permission of the copyright owner. Further reproduction prohibited without permission.

6.4.2.4 Terminating Successive Approximations

A key point in the simulator algorithm us defining the criterion at which the simulator ends the successive approximations for x at the n^{th} time step and begins to solve x at timestep $n+1$. The simplest criterion is

$$|x^{m+1} - x^m| < \epsilon, \tag{6.52}$$

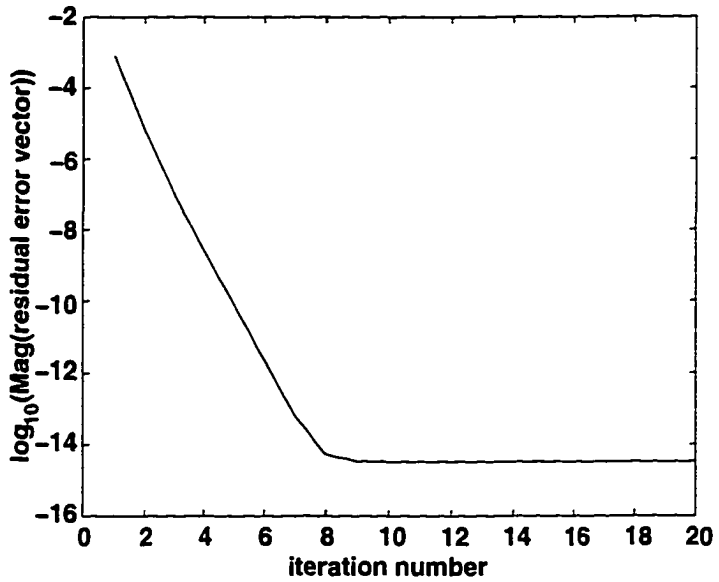
where ϵ is a tolerance. If the difference in x between two successive iterations is smaller than ϵ, the approximation for timestep n is terminated and timestep $n+1$ begins. However, in cases where large meshes are involved, applying the above procedure at every point in the mesh (as in the three-dimensional cube) becomes computationally unwieldy.

Another approach to choosing this stopping criterion is to examine the error in terms of a residual error vector [100]. The residual error vector, $\mathbf{e}$, is defined here as

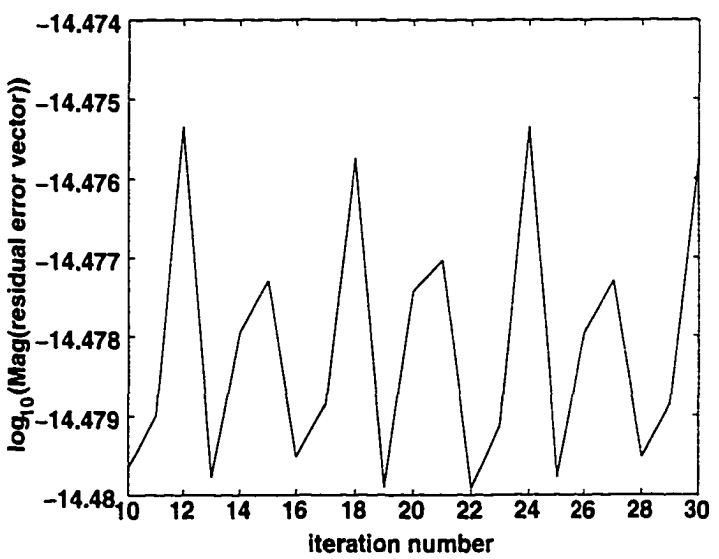
$$\mathbf{e}^{\mathbf{m}} = P_{-}\mathcal{E}^{n} - P_{+}\mathcal{E}^{n+1,m} \tag{6.53}$$

where $\mathcal{E}^{n+1,m}$ is the m^{th} iterative of $\mathcal{E}^{n+1}$, Then, when the length of the residual error vector (the Euclidean norm of $\mathbf{e}$) first reaches a minimum, the iterative process for timestep $n+1$ can be considered complete. Figure 6.9 shows a typical series of iterations for a given timestep. For the first several iterations (Fig. 6.9(a)) the error vector's magnitude decreases quickly, until iteration 10, at which point $|\mathbf{e}|$ has reached a minimum. Here the algorithm would terminate. Figure 6.9(b) is a plot of $\mathbf{e}$ if the algorithm is not terminated. After iteration 10, $\mathbf{e}$ simply oscillates, since there are no appreciable changes in the field values across the mesh.

Reproduced with permission of the copyright owner. Further reproduction prohibited without permission.



(a)



(b)

Figure 6.9: (a) Magnitude of residual error vector versus iteration number and (b) oscillations in residual error vector after convergence for a typical case.

Reproduced with permission of the copyright owner. Further reproduction prohibited without permission.

6.4.2.5 Symmetry Considerations

As in section 6.3, the use of symmetry is greatly beneficial in increasing computational efficiency. In Fig. 6.4is an example where symmetry exists in along both the x-z and y-z planes. The Neumann conditions imposed here are

$$\left.\frac{\partial \mathcal{E}_p(x,y,z)}{\partial x}\right|_{x=x_center} = 0, \tag{6.54}$$

$$\left.\frac{\partial \mathcal{E}_p(x,y,z)}{\partial y}\right|_{y=y_center} = 0. \tag{6.55}$$

Needed memory and computation time decrease by a factor of 4.

6.4.2.6 Simulation Region Size

Looking back at Eq. (6.13), the propagator matrices have been assumed constant; that is, the elements of P_+ and P_- are static. In addition, the propagator matrices must include the entire simulation region along the propagating direction. Such a requirement is computationally expensive, as the field amplitudes at points through which the wavepacket has already passed are in all likelihood negligible.

To address these issues, a simulator which can slide along the progating direction can be implemented, in which points where $\mathcal{E}(\mathbf{r})$ is greater than some tolerance ϵ are included in the simulation. Effectively, the non-neglible field values are zeroed out. The simulation window thus shifts along with the wavepacket. Obviously, the reduction in the simulation size increases the efficiency of the computation.

6.4.2.7 Timestep size

Finally, it is noted that changing the timestep Δt affects the rate of convergence at a given timestep. While a large Δt increases the distance the wavepacket will move for a single timestep, the number of iterations to reach the stopping criterion increases. Also, the wavepacket center will move at a speed $v_g < \frac{c}{n_r}$ unless either

Reproduced with permission of the copyright owner. Further reproduction prohibited without permission.

the mesh pitch is small (with reference to the propagating electric field wavelength) or the timestep is small, although this should not pose problems if the total energy within the simulation remains constant. In this light, the choices of Δt and mesh point spacing can be empirically determined.

6.4.3 Application

As stated before, three-dimensional simulations are necessary whenever the transverse dimension ignored in a two-dimensional analysis is non-negligible. However, at this time of this writing, the mesh discretization required for a complex microcavity simulation forces the simulation time to be exceedingly long. Therefore, a brief example using the simulator will be given here.

In this application, the reflectivity at the end of a semiconductor/air waveguide is desired. The visualization of the guide geometry is shown in Fig. 6.10(a). The 10 μm long waveguide is composed of a core 1 μm by 1 μm with $n_r = 3$ with cladding $n_r = 2$. At the end of the guide, $n_r = 2$, reducing the discontinuity in n_r at the waveguide end. This improves the speed of the iterative convergence when the packet hits the boundary.

Along the transverse directions the guide is discretized as a 17×17 point grid. The discretization is chosen since it is the same discretization that was used to obtain the solution of the initial eigenvalue problem (solved at $t = 0$, as in Eq. (6.8) for 2D cases), using general solver from the LINPACK software. It should be noted that a $17^2 \times 17^2$ grid ($\times 3^2$, to include the field polarizations) is solved in a reasonable time using the general LINPACK solver; a more accurate solution can be found using the implicit-shift or Lanczos methods [98]. It is important, in this case, that the discretization of the eigenvalue solution should closely match the discretization

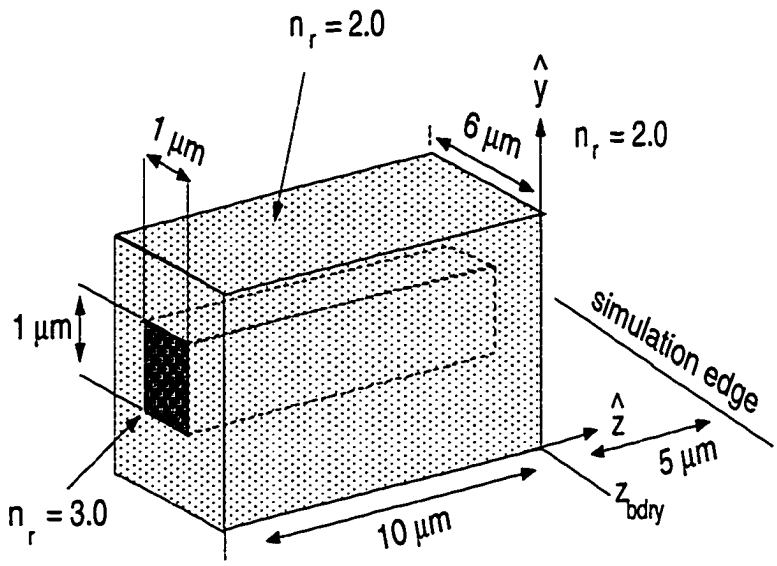
Reproduced with permission of the copyright owner. Further reproduction prohibited without permission.

of the guide. For instance, after solving the eigenvalue equation for the 17×17 discretization, a two-dimensional second order Taylor series was used to interpolate the fundamental eigenvector to obtain a 51×51 mesh. However, since the associated eigenvalue is, within numerical precision, more accurate for the 17×17 mesh, resulting perturbations caused the iterative process to proceed much more slowly. The eigenvector derived from the $t = 0$ condition for the transverse dimensions of the waveguide is shown in Fig. 6.10(b).

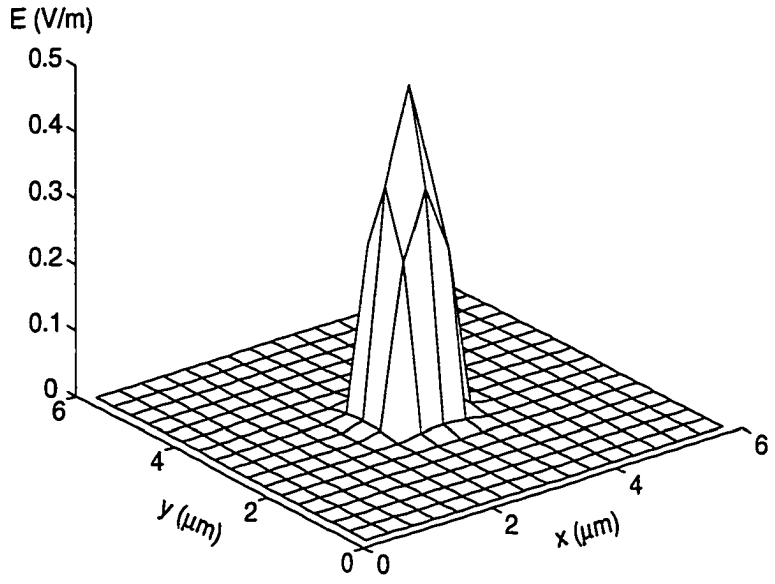
The initial wavepacket in the x-z plane at $y = 3\mu$m is shown in Fig. 6.11, for the x- and z-polarizations (in this geometry $\mathcal{E}_x = \mathcal{E}_y$). Since the initial field is only z-polarized, it is the only non-zero component. As the packet propagates to the end of the waveguide, the x- field component evolves through the term $\frac{\partial}{\partial z}(\mathcal{E}_z \frac{\partial \epsilon(\mathbf{r})}{\partial z})$, from Eq. (6.30), and this is seen in Fig. 6.12. The reflectivity of the cavity end is found from the simulation to be 10%, which differs from the value of 4% obtained from a plane-wave analysis assuming an infinite boundary, and is attributable to the geometry of the structure [82]. The importance of this example, however, is the demonstration of the polarization coupling, which is neglected in 2D simulations.

Although this particular example is simple and did not take an extraordinary long time (only $\sim$ 6 hours on a Sun UltraSparc2 using batch queueing), the time for simulations to complete that are more complex increases exponentially due to the number of iterations needed for convergence, number of mesh points used in the simulations, and associated memory limitations. The simulator itself is robust and flexible, and therefore is currently constrained by time. Hopefully, either single workstation speed will increase, or a algorithm speed-up (such as that suggested in Appendix C) will lead to computationally inexpensive solution for very involved problems.

Reproduced with permission of the copyright owner. Further reproduction prohibited without permission.



(a)



(b)

Figure 6.10: (a) The waveguide and (b) the associated fundamental eigenvector for the 3D simulation.

Reproduced with permission of the copyright owner. Further reproduction prohibited without permission.

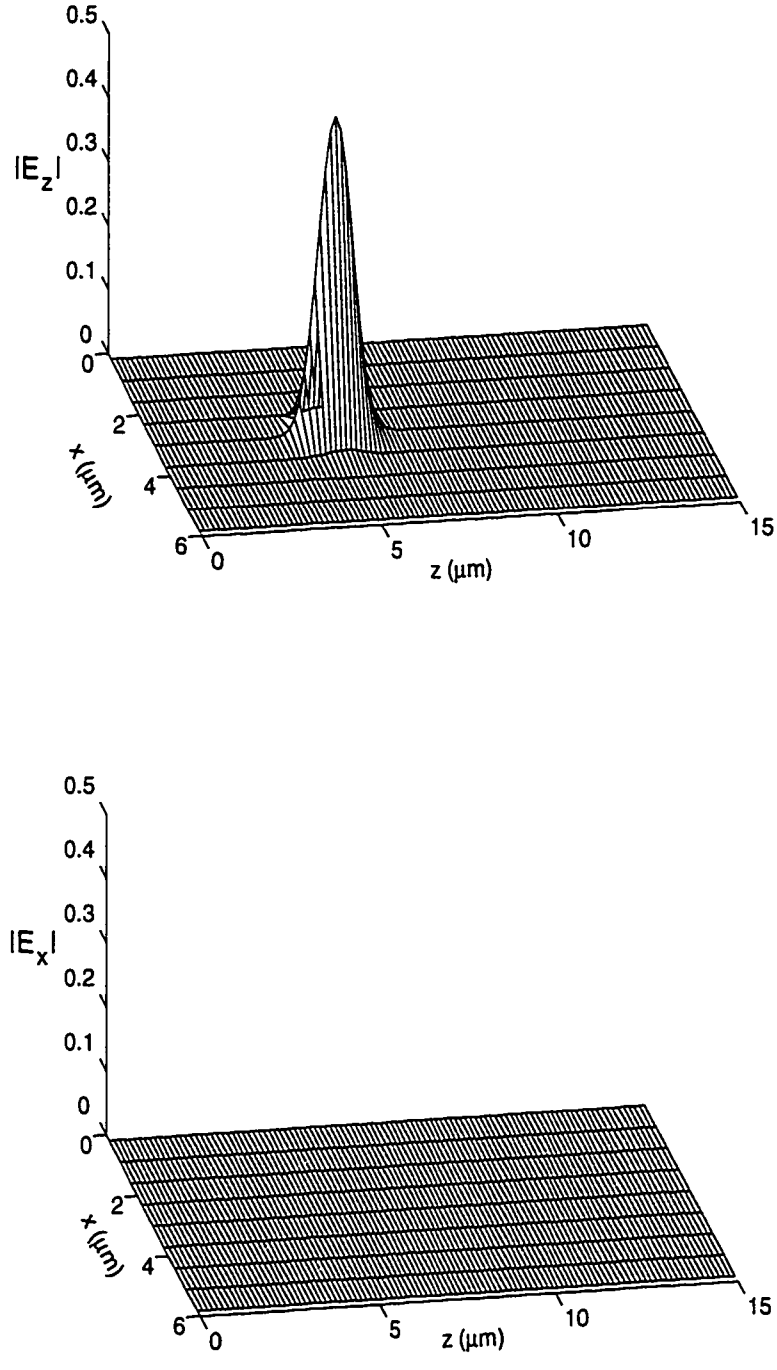


Figure 6.11: (a) The x- and z-components of the initial wavepacket, in the x-z plane at $y = 3\mu$m.

Reproduced with permission of the copyright owner. Further reproduction prohibited without permission.

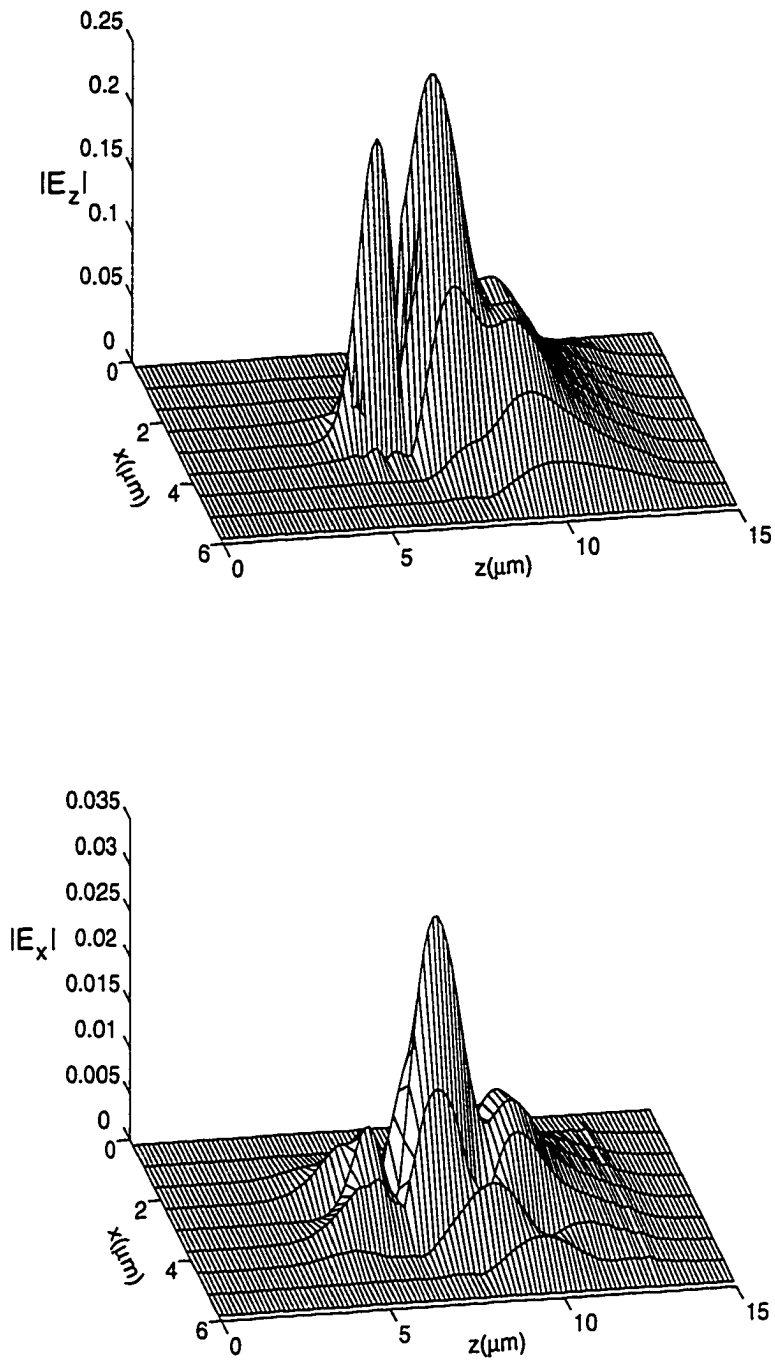


Figure 6.12: (a) The x- and z-components of the wavepacket upon reflection, in the x-z plane at $y = 3\mu$m.

Reproduced with permission of the copyright owner. Further reproduction prohibited without permission.

CHAPTER VII

DESIGN STUDIES FOR DISTRIBUTED BRAGG REFLECTORS FOR SHORT CAVITY EDGE EMITTING LASERS

7.1 Introduction

Conventional edge-emitting semiconductor lasers are fabricated through cleaving resulting in mirror reflectivities in the range $\sim$ 0.3–0.4. In edge-emitting distributed feedback (DFB) or distributed Bragg reflector (DBR) lasers, a Bragg reflector is placed in the path of the optical beam, but the device construction is such that a very small fraction ($\sim$1–2%) of the beam sees the Bragg action. As a result, while these structures offer better mode selectivity, the overall mirror relectivity remains low. The low mirror reflectivities preclude the use of very short cavity edge-emitting lasers since the mirror loss is too high.

Reduction in device size for edge-emitting semiconductor laser devices offers gains in two areas: 1) lower parasitic capacitances and 2) increased integrable component density per chip. In reducing parasitics the 3dB bandwidth increases. Since capacitance is proportional to area, via $C = \frac{\epsilon_0 A}{d}$, a reduction in device length would decrease the associated parasitic capacitance. However, for a simple slab waveguide semiconductor laser, losses increase prohibitively as the cavity length decreases. In

Reproduced with permission of the copyright owner. Further reproduction prohibited without permission.

order to offset this, the reflectivity of the etched mirror at each end of the cavity must be increased.

Generally, for a GaAs/air interface the reflection coefficient value is taken as ~ 32 %, a value obtained using assuming the dielectric boundary is infinite. It has been shown previously that in slab waveguide structures reflectivity values exceed those obtained using a standard transmission-line analysis (TLA) due to geometrical effects [80] However, assuming that the reflectivity at the slab waveguide interface with GaAs as the gain medium is as high as 40 % leaves little improvement in device size reduction without a dramatic increase in mirror loss. Thus, a method for increasing reflectivity at the cavity ends is called for.

Vertical cavity lasers employ distributed Bragg reflecting (DBR) stacks to increase the effective reflectivity of the cavity ends via growth of alternating dielectric layers to take advantage of standing wave patterns formed in such structures. In vertical cavity DBR structures, many periods are used since the refractive indices of the dielectrics in the stack are usually close in value. However in an edge-emitting semiconductor laser a period could be formed from the cavity material itself and an air gap created via etching. Current etching technologies allow one to produce such deep ($\sim$1.0μm) uniform etches in semiconductors. Due to the refractive index difference between air and semiconductor, it is expected that a small number of periods would have to be used to obtain high reflectivity. Additionally, the horizontal nature of the structure lends itself to implementation in monolithic circuits demanding high bandwidth components. Essentially the entire optical beam sees the DBR stack shown schematically in Fig. 7.1. In this paper we study several aspects of a horizontal semiconductor laser structure with a DBR grating placed at one end. In particular, the following questions are addressed:

Reproduced with permission of the copyright owner. Further reproduction prohibited without permission.

i) How many mirrors are needed in the external DBR stack to provide significant improvement in cavity reflectivity?

ii) What are the optimum placement positions of the mirrors?

iii) How sensitive is the mirror reflectivity to variations in the mirror placement and to the shape of the mirrors?

iv) What is the wavelength dependence of the reflectivity?

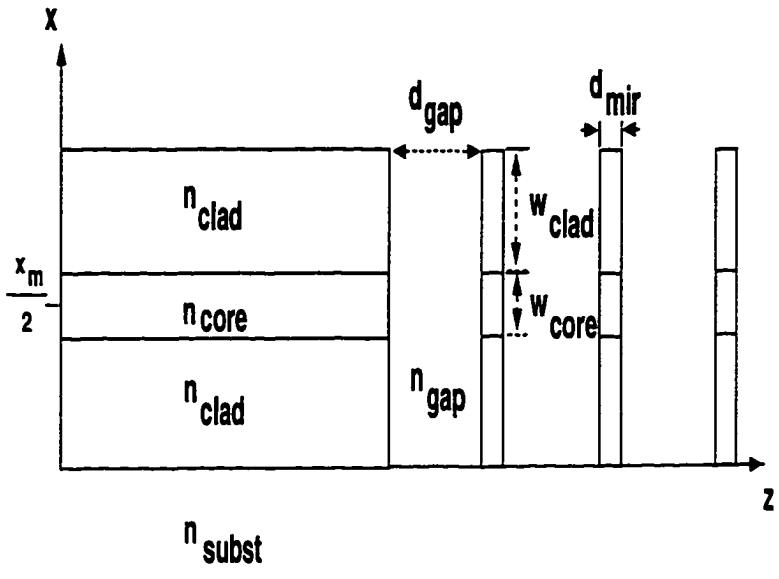
v) How does the reflectivity depend upon the index of the material used in filling the space between the mirrors?

First an extension of the formalism developed in Chapter 6 is presented. Following this, results obtained from simulations are given. The simulations include studies involving periodic and aperiodic spacings of abrupt-surface mirrors, periodic spacings of non-uniform surface mirrors, and reflectivity of an external DBR for varying wavelength. Finally, a comparison between calculation and experimentally measured data is given.

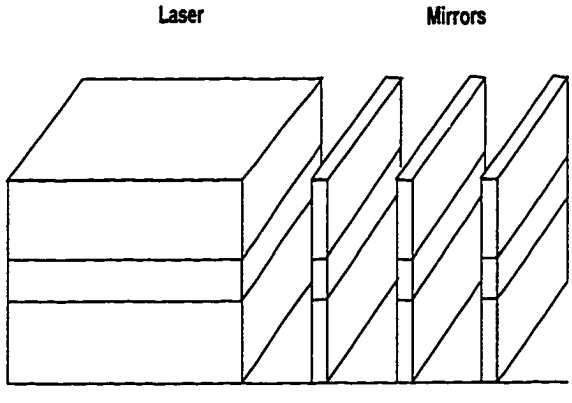
7.2 Formalism

As in Section 6.3, a wavepacket constructed about the fundamental mode β_0 is launched in the waveguide a sufficient distance from the ends of the guide.After some time t_r the wave packet is assumed to have reached the end of the waveguide and will encounter the mirror grating.After a further time $t_r + \delta t$ a fraction of the wave packet will be transmitted through the grating, a fraction of the wave packet will be reflected back into the guide (and cladding), and a negligible fraction of the wave packet will yet remain in the grating itself.To optimize reflectivity for a DBR-structure for a particular (vacuum) wavelength λ, at normal incidence, it is necessary to satisfy the

Reproduced with permission of the copyright owner. Further reproduction prohibited without permission.



(a)



(b)

Figure 7.1: A three-dimensional visualization of the basic structure for the model used in this study and (b) a two-dimensional projection of (a) with the corresponding parameters labeled.

Reproduced with permission of the copyright owner. Further reproduction prohibited without permission.

Bragg condition

$$2m\pi = 2(\beta_1 d_1 + \beta_2 d_2), \tag{7.1}$$

where β_1 and β_2 are the propagation constants of the wave packet in the dielectrics, with refractive indices n_1 and n_2 and of thicknesses d_1 and d_2, that compose one period of the DBR. From Eq. (7.1) it is seen that the Bragg condition will be sensitive to the propagation constant value, yet from the starting condition the wave packet has a large spread in β. Therefore, it is necessary to calculate the power reflected in the single mode β_0. This can be accomplished invoking Parseval's theorem [102] , and therefore, the reflectivity, R, of the DBR can be calculated as

$$\begin{aligned} R &= \frac{P(\beta_0, t = t_r + \delta t)}{P(\beta_0, t = 0)} \\ &= \frac{\left| \int_{-w/2}^{w/2} \int_{z_a}^{z_b} \mathcal{E}(x, z, t_r + \delta t) e^{i\beta_0 z} dz dx \right|^2}{\left| \int_{-w/2}^{w/2} \int_{z_a}^{z_b} \mathcal{E}(x, z, 0) e^{-i\beta_0 z} dz dx \right|^2}, \end{aligned} \tag{7.2}$$

where the waveguide core is defined $-w/2 < x < w/2$, $z_a < z < z_b$. Note that the sign of the exponential in the numerator of Eq. (2.11) is positive, because the reflected wave travels in the $-z$-direction.

7.3 Results

In this section results of the simulations are presented. First the basic characteristics of the simulator and simulaton geometry are described, and then results obtained for specific cases studied are discussed.

7.3.1 Simulation Characteristics

The basic structure used in our studies is shown in Fig. 7.1. The laser cavity is fabricated by growth in the x-direction, and the electric field propagation direction, is in the z-direction. As shown in Fig. 7.1, the structure is fabricated starting with a

Reproduced with permission of the copyright owner. Further reproduction prohibited without permission.

substrate with refractive index n_{subst} on which is grown a device with layers forming a cladding region with an effective cladding refractive index n_{clad} and an active region with an effective refractive index n_{core}. Spaced a distance d_{gap} from the end of the cavity are mirrors of the same layer structure as the laser, and are assumed to be formed by an appropriate deep etch. Each mirror has a thickness d_{mir}. The cladding layers have a width w_{clad} while the active region has a width w_{core}. Above the top cladding layer is air.

In this study the substrate is chosen to have a refractive index $n_{subst} = 1.0$. This is done to symmetrize the geometry of the simulation. Because the field profile studied in this simulation (the fundamental propagating TE mode) is symmetric along the growth direction, choosing $n_{subst} = 1.0$ allows the imposition of a Neumann boundary condition, $\frac{\partial E}{\partial x} = 0$ at the point $\frac{x_m}{2}$. By taking advantage of the symmetry in this manner, only $\frac{1}{2}$ of the memory cells that a full geometry simulation requires are needed without losing any information. This assertion holds assuming that a refractive index $n_{subst} > 1.0$ will not yield different results due to reflections of divergent waves off of the substrate into the mirror. Simulations have been carried out using an asymmetric geometry using with $n_{subst} = 3.0$ and $n_{air} = 1.0$ and the results appear to uphold this assumption.

To start the calculations it is it israssume that the dielectric gap between each mirror is in quarter-wavelength ($\frac{2k+1}{4}$) units of λ_0. Using Eq. (7.1) to solve for d_{mir} we assume the value of β_2 obtained from Eq. (6.8) will be the propagation constant of the electric field for each mirror. For $\lambda_0 = 0.98$ μm, $w_{core} = 0.10$ μm, $n_{core} = 3.49$, $w_{clad} = 1.0$ μm, and $n_{clad} = 3.23$, we obtain $\beta_2 = 2.096 \times 10^7$ m^{-1}, giving $d_{mir} = 0.38$ μm. These values of w_{core}, n_{core}, w_{clad}, n_{clad}, and d_{mir} will be constants in all of the following cases presented.

Reproduced with permission of the copyright owner. Further reproduction prohibited without permission.

Due to the submicron nature of the core, air gap, and mirror thickness, values for the spatial steps are chosen as $\Delta z = 0.02$ μm and, within the core region $\Delta x = 0.005$ μm. The value of Δx increases as the wave position along the x-direction moves further from the core, to a maximum value of $\Delta x = 0.12$ μm for the 1.2 μm farthest from the core at the simulation edge (along the x-direction). The value of Δx does not change across a dielectric interface, thus avoiding computational errors and locally-satisfying the Von Neumann stability condition. The simulation region is 40 μm along z and 32 μm along x, or 2000 (z) by 454 (x) points, where 454 reduces to 227 by imposing the Neumann condition. The timestep value, Δt, is taken as .2875 fs.

At the simulation boundaries an absorbing region is used to eliminate reflections at from the simulation edge. Additionally, as a check for the simulation, the total energy through the whole simulation region is calculated and found to remain constant, until the wave reaches the absorbing regions, at which point total energy is found to decrease.

7.3.2 Periodically Spaced Mirrors With Abrupt Surfaces

Using the structure presented in Fig. 7.1, simulations are performed on a DBR with periodically spaced mirrors having abrupt (flat) surfaces. Mirrors external to the cavity are spaced apart at a distance $d_{gap} = \frac{2k+1}{4}\lambda_0$ to facilitate constructive interference, with $d_{mir} = 0.38$ μm. Results are shown in Fig. 7.2 for 1, 2, and 3 mirrors with $k \subset \{0, 1, 2, 3, 4\}$. Using only one mirror yields a substantial increase in reflectivity over that found from a waveguide-air interface (37%); however further increases in reflectivity are markedly smaller using more mirrors, and after 3 mirrors simulations reveal that saturation appears to occur. Also, reflectivity is found to decrease as the spacing between mirrors increases. These characteristics are not seen

Reproduced with permission of the copyright owner. Further reproduction prohibited without permission.

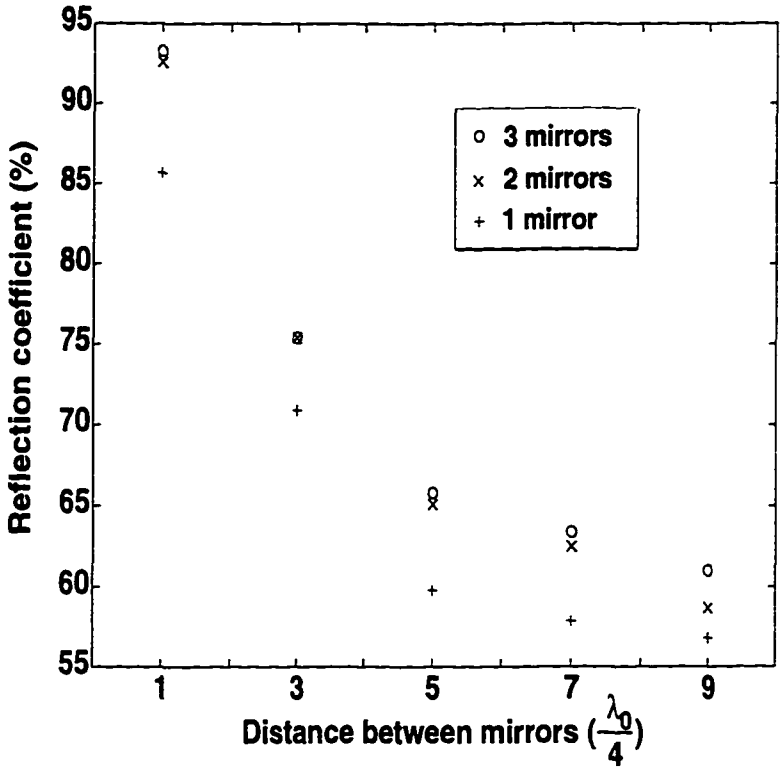


Figure 7.2: Reflection coefficient calculations using the structure presented in Fig. 7.1 for 1,2,and 3 mirrors. The mirrors are periodically spaced and assumed to have uniform surfaces.

when using a classical transmission-line analysis of a dielectric stack, which assumes infinite dielectric boundaries. This behavior is attributed to the divergence of the electric field from the core region at the waveguide-air interface.

Due to the large difference in refractive index at the interface, the reflectivity of a DBR-stack should be quite large using only a few periods, and this is seen in Fig. 7.2. However, since the interfaces at the dielectric boundaries are not infinite, light which has diverged at the interface will not constructively interfere with light re-entering the waveguide core. Since the refractive index of the air gap is much lower than that of the core, the electric field diverges quickly upon reaching the waveguide-air interface. Thus, a decrease in reflectivity is seen as d_{gap} increases. Increasing the number of mirrors has marginal effect after 3 mirrors as the power in the core region

Reproduced with permission of the copyright owner. Further reproduction prohibited without permission.

of each mirror becomes progressively smaller for each mirror farther from the active region end. The electric field also diverges from the core region of each mirror as well. A dramatic reduction in reflectivity is seen going from $k = 1$ to $k = 3$; further increases in mirror spacing yield smaller reductions in reflectivity, and at large mirror spacings it is expected that the reflectivity will be approximately 37 %.

7.3.3 Aperiodically Spaced Mirrors With Abrupt Surfaces

In the previous subsection it was assumed that the mirrors comprising the external DBR had periodic spacing. However, during fabrication, errors in lithography may occur. Although for devices with large error tolerances lithographical errors may not be a serious problem, both the submicron nature of the structures under study and the constraints of mirror placement in a DBR for high reflectivity place a premium on precise mirror position. Therefore, the case of aperiodic spacing of the mirrors is now considered.

In Fig. 7.3(a) we present a model of a two-mirror aperiodic external DBR system. Parameters of the simulation are the same as in section 4.1, except that the constant periodic spacing parameter, d_{gap}, is replaced by the variable gap lengths L_1 and L_2, which represent the spacings from the cavity to the first mirror and from the first mirror to the second mirror, respeectively. Gap length L_1 varies from 0.0 μm to 1.0 μm in increments of 0.1 μm, while L_2 ranges from 0.1 μm to 1.0 μm in increments of 0.1 μm.

Figure 7.3(b) shows the results of simulations performed varying L_1 and L_2. The results indicate that peak reflectivity occurs when L_1 and L_2 are equal to $\frac{\lambda_0}{4}$ or $\frac{3\lambda_0}{4}$. Conversely, maximum destructive interference occurs when L_1 and L_2 are equal to integer half-wavelengths. The position of the first mirror, for larger values of L_1,

Reproduced with permission of the copyright owner. Further reproduction prohibited without permission.

appears to be more critical than that of the second mirror; for example, at $L_1 = 0.8$ μm, varying L_2 from 0.6 μm to 0.8 μm, or from 0.2 μm to 0.4 μm does not appear to significantly affect the reflectivity of the DBR. In contrast, fixing L_2 and varying L_1 from 0.6 μm to 0.8 μm appears to show a change in reflectivity > 10 %. Also, the maximum reflectivity decreases as either L_1 or L_2 increase, due to the divergence of the electric field, as mentioned in section 4.2. Overall, the results show that errors attributed to lithography of less than 0.2 μm should not seriously impair the external DBR performance.

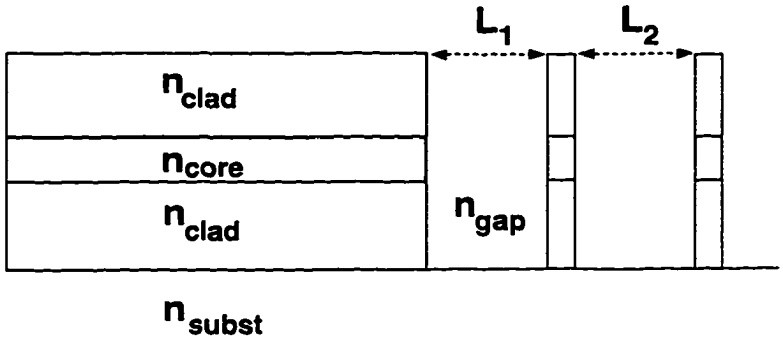
7.3.4 Periodically Spaced Mirrors With Non-Uniform Surfaces

In the previous two sections simulations have been performed using mirrors with abrupt (i.e. atomically flat) surfaces. However, a non-uniform mirror surface can be formed during etch processes such as and under-etch during a wet etch, or shadowing effects from a dry etch. Therefore, it is useful to model and simulate the effects of having mirrors with non-uniform surfaces.

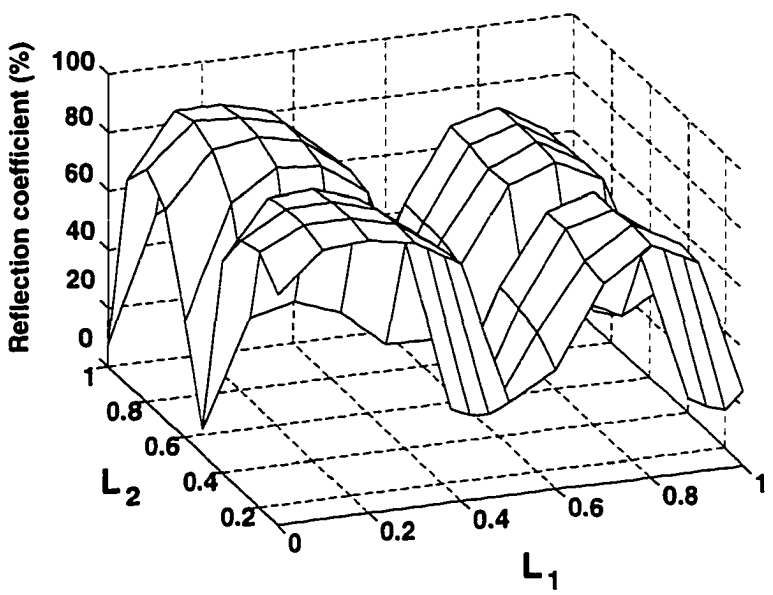
In Fig. 7.4(a) the model used for this set of simulations is shown. It is assumed the mirror surfaces are described by a parabola of the form $a(z-z_0)^2+b)$, where a is a "parabolicity depth" which controls the radius of curvature of the mirror surface. The mirror width $d_{mir} = 0.38$ μm; for $a \neq 0$, d_{mir} equals the maximum mirror. Thus, for $a = 0.06$ μm, the width at the (core) center of the mirror is 0.38 μm, but at the substrate surface the mirror width is 0.26 μm. For each simulation the mirror spacing d_{gap} increases from $\frac{\lambda_0}{4}$ to $\frac{9\lambda_0}{4}$ in increments of $\frac{\lambda_0}{2}$, while the mirror parabolicity depth a increases from 0.0 μm to 0.18 μm in steps of 0.03 μm.

In Fig. 7.4(b) results of simulations using a single-mirror external DBR with parabolic surfaces are presented. For all mirror spacings, a slight increase in reflection

Reproduced with permission of the copyright owner. Further reproduction prohibited without permission.



(a)



(b)

Figure 7.3: (a) The model for a structure assuming aperiodically spaced mirrors and (b) reflection coefficient calculations using the structure presented in (a). The mirrors are assumed to have uniform surfaces.

Reproduced with permission of the copyright owner. Further reproduction prohibited without permission.

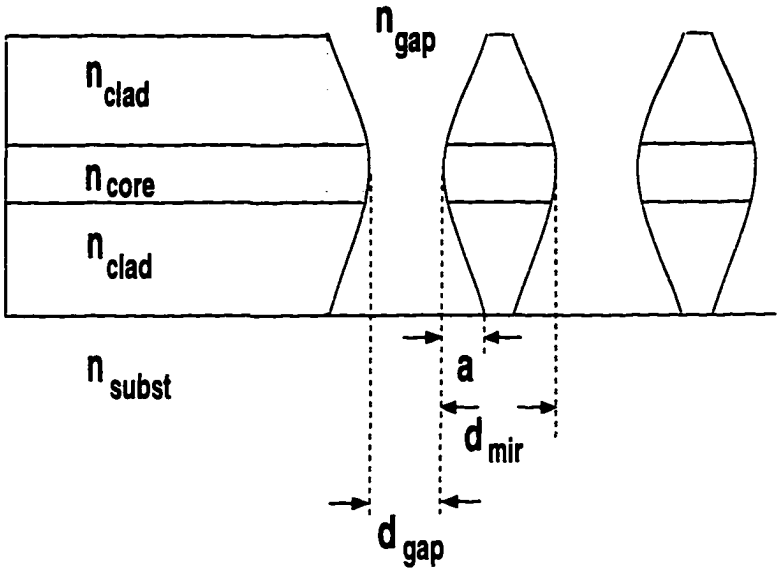
coefficient occurs for small values of a, possibly due to a lensing effect from the curved dielectrics. Also, for all values of d_{gap} considered, the reflection coefficient decreases as the mirror parabolicity becomes large. Figure 7.4(c) shows results of simulations using 2 mirrors having parabolic surfaces. The results are similar to those presented in Fig. 7.4(b): an increase in reflectivity for small mirror parabolicity, and a decrease in reflectivity for large values of a. The results appear to demonstrate that small mirror spacings have more tolerance for non-abrupt mirror surfaces, and that for large mirror spacings mirror curvature may be of concern.

7.3.5 Wavelength Dependence of the Reflectivity of the External DBR

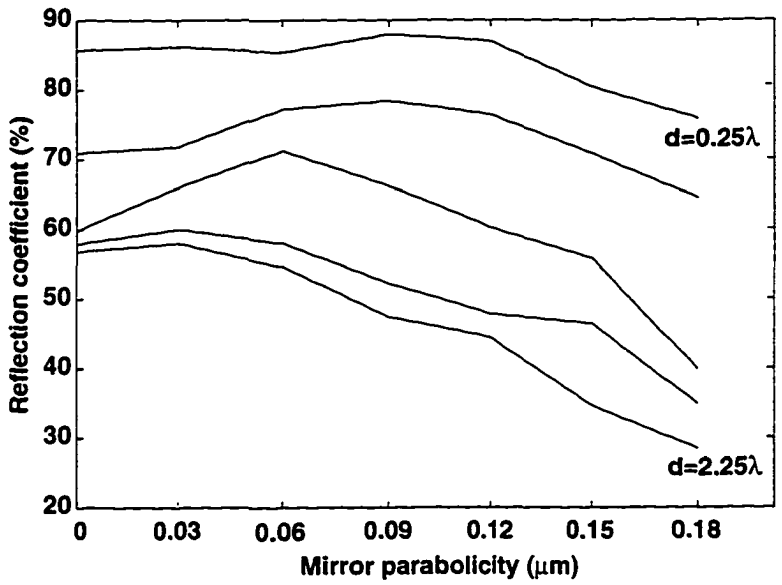
The simulations done to this point in the study have focused on using a constant wavelength, $\lambda_0 = 0.98$ μm. The reflectivity of the external DBR will change with wavelength, as the Bragg condition for constructive interference is given by Eq. (2.10). Thus, if the laser output wavelength λ differs from the structure design wavelength λ_0 (due to temperature effects, material characteristics, etc.), the reflectivity may be less than originally expected. Therefore, in this section we study th reflectivity of the external DBR versus wavelength.

Figures 7.5(a)-7.5(e) show the results of DBR configurations using 1 to 3 mirrors with different spacings. A transmission-line (classical one-dimensional) analysis curve is also plotted for comparison. The TLA assumes infinite dielectric interfaces with each material having a single refractive index; to adapt the mirrors for TLA, we assume each mirror is modeled as a single dielectric with an effective refractive index n_{eff}. The effective refractive index of a single mirror in our geometry is then calculated using the dispersion relation $\beta_0 = \frac{2\pi n_{eff}}{\lambda_0}$; for $\lambda_0 = 0.98$ μm, and $\beta_0 = 2.096 \times 10^7$

Reproduced with permission of the copyright owner. Further reproduction prohibited without permission.



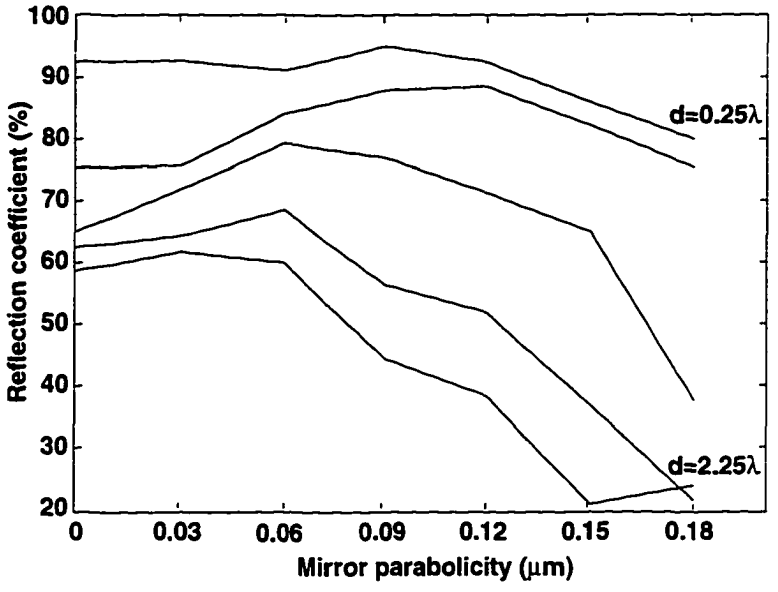
(a)



(b)

Figure 7.4: (a) the model for a structure assuming mirrors with nonuniform (parabolic) surfaces, and reflection coefficient calculations considering (b) one mirror.

Reproduced with permission of the copyright owner. Further reproduction prohibited without permission.



(c)

Figure 7.4: (c) Reflection coefficient calculations considering two mirrors for the structure in (a).

m^{-1}, $n_{eff} = 3.269$. Then, using the recursive relation [99]

$$Z_j = Z_{g,m} \frac{Z_{j+1} cos(\beta_j d_j) + i Z_{g,m} sin(\beta_j d_j)}{Z_{g,m} cos(\beta_j d_j) + i Z_{j+1} sin(\beta_j d_j)}, \tag{7.3}$$

where Z_j is the impedance looking away from the cavity end of the j^{th} dielectric (gap or mirror, in this instance) away from the cavity, $Z_{g,m}$ is the impedance of the j^{th} dielectric (gap or mirror), Z_{j+1} is the impedance looking from the $j+1$ dielectric, β_j is the wavenumber of the j^{th} dielectric, and d_j is the length of the j^{th} dielectric. Impedance Z_1 corresponds to the first dielectric gap, and the reflection coefficient using this classical analysis is then

$$R = \left| \frac{Z_{eff} - Z_1}{Z_{eff} + Z_1} \right|^2, \tag{7.4}$$

where Z_{eff} is the impedance of the cavity which has an assumed effective refractive index n_{eff}.

Reproduced with permission of the copyright owner. Further reproduction prohibited without permission.

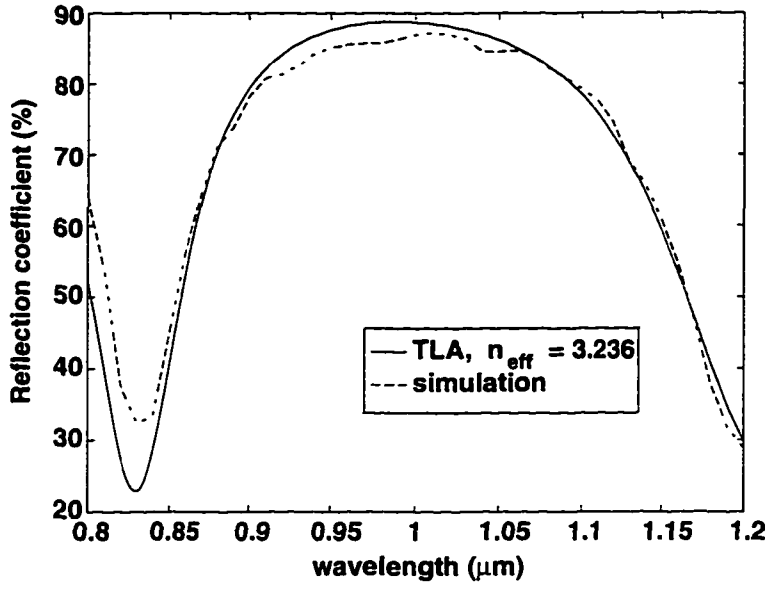
Simulation are done using $0.80\mu\text{m} \leq \lambda \leq 1.20\mu\text{m}$, with λ increments of 0.01 μm. (An inverse Fourier transform can recover this information using a single simulation using $\lambda = 1.0$ μm provided the spread in wavenumber $\Delta\beta$ is small. However, this necessitates a broad wavepacket spatially, which would extend beyond the limit of the 40 μm simulation region.) In addition, each mirror has width $d_{gap} = 0.38$ μm, as in previous sections. All other parameters are the same as mentioned in section 4.1.

Figure 7.5(a) shows the results of simulations done for a single-mirror external DBR spaced $\frac{\lambda_0}{4}$ from the cavity end. A TLA is also shown, plotted using the value of n_{eff} (3.236) which provided the best fit to simulation results, which is smaller than the value of 3.269 earlier obtained using the waveguide eigenvalue β_0. Simulation and classical approximation appear to be close, except that the destructive interference is not as strong at lower wavelengths, and peak reflectivity is slightly lower. The breadth of the main reflectivity peak of the external DBR appears to be as large as that classically predicted.

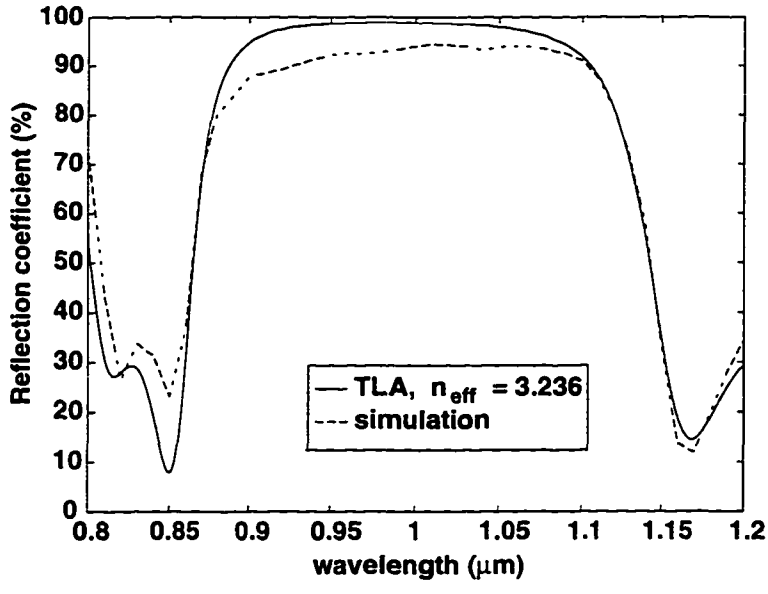
Figure 7.5(b) shows results of simulations for a two-mirror external DBR with mirror spacing $d_{gap} = \frac{\lambda_0}{4}$. As in the single-mirror case, the peak reflectivity is not as large as that classically predicited, and destructive interference is not as strong at lower wavelengths. Reflection coefficients from simulation appear to increase slightlt above λ_0, but the breadth of the main peak again appears to match the TLA.

Figures 7.5(c),7.5(d), and 7.5(e) show results of simulations for a three-mirror external DBR with mirror spacings $\frac{\lambda_0}{4}$ (c), $\frac{3\lambda_0}{4}$ (d), and $\frac{5\lambda_0}{4}$ (e). Figure 7.5(c) shows simulation results which are consistent with those presented in Figs. 7.5(a) and 7.5(b). Again, results appear to match the classical analysis more closely at longer wavelengths. The spectrum is more broad and sharper than the spectrums of 7.5(a) and 7.5(b). Results in Figs. 7.5(d) and 7.5(e) do not match as well with classical

Reproduced with permission of the copyright owner. Further reproduction prohibited without permission.



(a)



(b)

Figure 7.5: External DBR wavelength reflectivity calculations using the structure presented in Fig. 7.1 considering (a) 1 mirror with $d_{gap} = \frac{\lambda_0}{4}$, and (b) 2 mirrors with $d_{gap} = \frac{\lambda_0}{4}$

Reproduced with permission of the copyright owner. Further reproduction prohibited without permission.

approximations, although the shapes of the simulation curves does agree with that of the TLA. The widths of the reflectivity spectrums are narrower since the path lengths through the dielectric (air) gap between the mirrors have increased. In Fig. 7.5(d) the peak reflectivity occurs at 0.90 μm and gradually decreases reducing the width of the main reflectivity peak. In Fig. 7.5(e) the decrease in reflectivity from its maximum does not appear to be as sharp, though the peak itself is narrower. The effective refractive index found to give a best match for $d_{gap} = \frac{5\lambda_0}{4}$ is significantly lower (3.146) than the value of n_{eff} used in previous simulations, indicating that as the mirror spacing increases, the refractive index the propagating wave sees decreases. Overall, we find that although excursions of up to 0.05 μm on either side of λ_0 result in a small change in reflection coefficient due to the breadth of the main reflectivity peak even at larger mirror spacings, the DBR tolerance improves substantially as the number of mirrors used increases and the mirror spacing decreases.

7.3.6 Periodically Spaced Mirrors with Varying Gap Dielectrics

In the processing of monolithically-integrated circuits it is sometimes necessary to use a dielectric "filler" in some capacity, such as an insulator. For an optically-isolated integrated laser-photoreceiver circuit, then, instances may be envisioned where a dielectric maybe used as the gap material instead of air, as has been considered in all of the previous simulations. To examine the consequences of using non-air dielectrics, simulations are carried out varying n_{gap}.

The structure used is the same as that presented in Fig. 7.1 as a three-mirror external DBR. The parameters values are the same as discussed in section 4.1, except that n_{gap} is no longer a constant for all simulations. The total free-space wavelength optical path length for one round-trip through the three mirrors is chosen to remain

Reproduced with permission of the copyright owner. Further reproduction prohibited without permission.

constant as 20.58μm, which corresponds to a total phase shift 42π. Thus, by Eq. (2.10), changing β_1 (n_{gap}) results in a change in d_1 (d_{gap}), since both β_2 (β_0) and d_2 (d_{mir}) are fixed. For the three-mirror system, a phase shift of 42π, for $n_{gap} = 1.0$, gives $d_{gap} = \frac{9\lambda_0}{4}$. Choosing a smaller value for the total optical path length may result in errors since d_{gap} decreases as n_{gap} increases (small changes in d_{gap} may not be resolvable due to the resolution of Δz (0.02 μm), which is likely for smaller total phase shifts).

Figure 7.6 shows the results for simulations when increasing n_{gap} from 1.0 to 3.2 in increments of 0.1. For low refractive index, the reflection coefficient is significantly lower than that obtained from the classical analysis, due to wave divergence. As the refractive index increases the reflection coefficient decreases. During the intermediate range $1.4 \leq n_{gap} \leq 2.4$ two phenomena appear to balance each other. As the gap refractive index increases, the difference between n_{core} and n_{gap} decreases, leading reflectivity to decrease. However, as n_{gap} increases, wave divergence decreases, allowing more power to remain in the area of the core "projected" along the gap, enhancing constructive interference. Thus, in this region only a slight decrease in reflectivity is seen. For $n_{gap} > 2.4$, light divergence is no longer the primary limiting factor for high reflectivity, and the reflection coefficient falls quickly. As n_{gap} approaches n_{eff}, the classical and simulation results agree well, because of limited divergence. It is necessary to point out that because the total phase shift has been kept constant, the mirrors have also become more closely spaced together as n_{gap} increases, which also limits the field divergence.

Reproduced with permission of the copyright owner. Further reproduction prohibited without permission.

7.4 Experimental Results

Short cavity edge emitting lasers using a semiconductor/air DBR were both fabricated and tested by the author's colleague Ya-hsing Yuan [103]. The laser heterostructure used was a GaAs-based MQW tunneling injection structure [5], with gratings formed using RIE, as shown in Fig. 7.7 . Since the lasing wavelength of fabricated device is $\sim 1.0\mu$m, it can be used for comparison of theoretical results of the previous section with experimentally measured parameters.

In Fig. 7.7 a $\frac{5\lambda}{4}$ grating is shown, a value chosen due to consideration of mechanical stability and the depth of etch required in the structure. From the theoretical calculations in Fig. 7.2, a 2 mirror DBR $\frac{5\lambda}{4}$ should exhibit a reflectivity of $\sim$ 66%. with saturation occurring beyond this point.

In Fig. 7.8 the measured L-I characteristic of the laser for different cavity lengths are shown. The lasers have a cleaved mirror at one end and the DBR at the other. with the output taken from the cleaved end. From the measured slope of threshold current density versus inverse cavity length, a reflectivity of 60% for a 2 period DBR stack is extracted, which is in very good agreement with the 66% reflectivity value previously mentioned. In addition, the experimental data confirms that reflectivity saturates after two periods, for this mirror spacing.

7.5 Conclusions

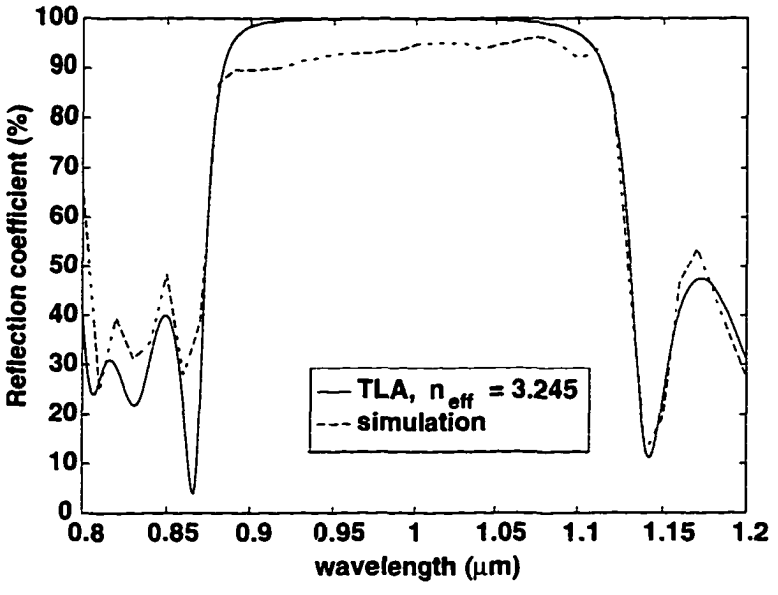
A laser cavity with an external DBR has been modeled and studied to explore the possibilities of using such structures in monolithic circuits requiring small cavity length, and therefore high reflectivity. Using air as the dielectric material between mirrors made of the same structure as the laser itself, we find that high reflectivity can be achieved using only 1 mirror, provided the period size of the DBR is small. As

Reproduced with permission of the copyright owner. Further reproduction prohibited without permission.

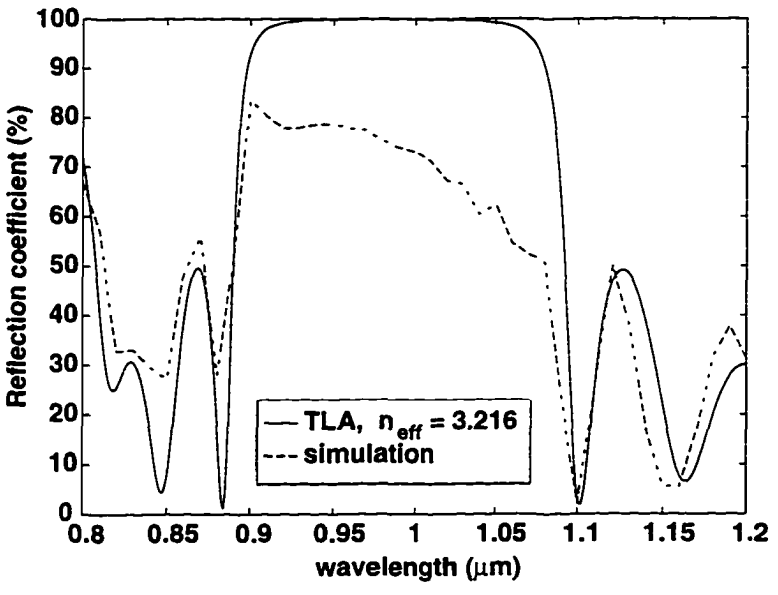
the period size increases, reflectivity decreases due to the divergence of light at the laser cavity-air interface. Increasing the number of mirrors in the DBR increases the reflectivity; however, the reflectivity appears to saturate after only 3 mirrors, again due to divergence. The external DBR's tolerance to lithographical errors, etch errors, and lasing away from design wavelength appear good in that reflectivity remains high for a reasonable excursion away from design parameters. Finally, introducing a material other than air as the gap dielectric material between mirrors results in a reduction in reflectivity. However, due to reduction in light divergence, it is likely that smaller period spacings than the one considered in this part of the study will yield reflectivity high enough to use a different gap dielectric a viable option.

Experimentally, measurements made on short cavity lasers with DBRs on one end yield results which are in very good agreement with calculated values. Thus, it appears that this method of increasing reflectivity using only a few mirrors can be useful in the design of short cavity lasers towards integrability.

Reproduced with permission of the copyright owner. Further reproduction prohibited without permission.



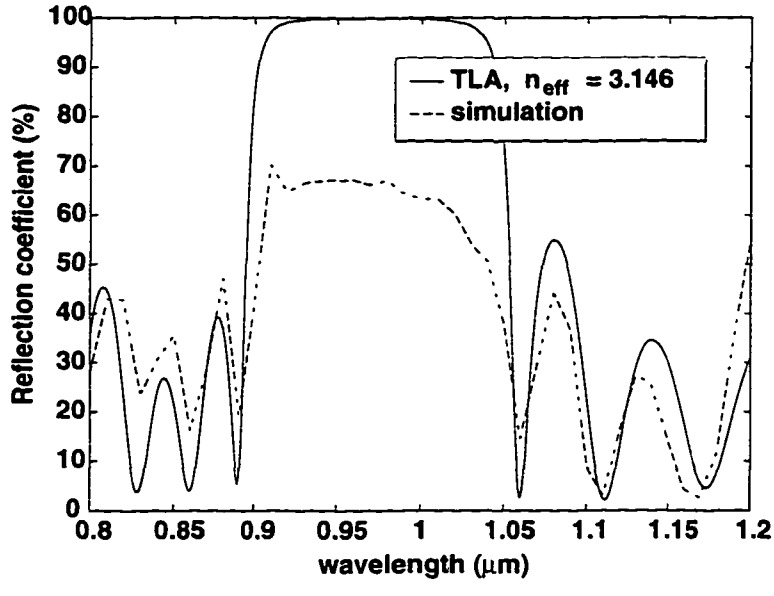
(c)



(d)

Figure 7.5: External DBR wavelength reflectivity calculations using the structure presented in Fig. 7.1 considering (c) 3 mirrors with $d_{gap} = \frac{\lambda_0}{4}$, and (d) 3 mirrors with $d_{gap} = \frac{3\lambda_0}{4}$

Reproduced with permission of the copyright owner. Further reproduction prohibited without permission.



(b)

Figure 7.5: External DBR wavelength reflectivity calculations using the structure presented in Fig. 7.1 considering (e) 5 mirrors with $d_gap = \frac{5\lambda_0}{4}$

Reproduced with permission of the copyright owner. Further reproduction prohibited without permission.

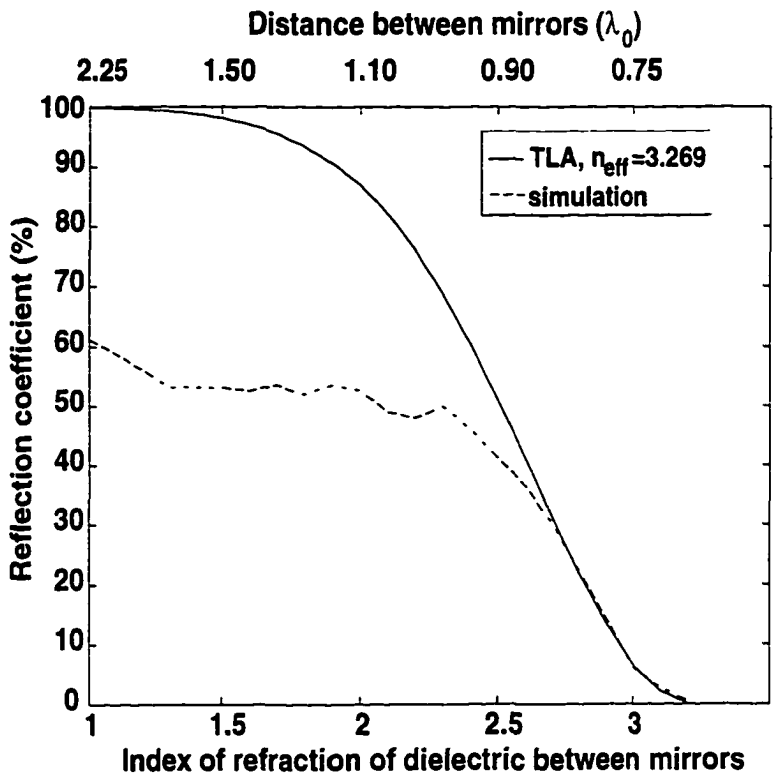


Figure 7.6: Reflection coefficient calculations using the structure presented in Fig. 7.1 considering 3 mirrors with varying gap refractive index.

Reproduced with permission of the copyright owner. Further reproduction prohibited without permission.

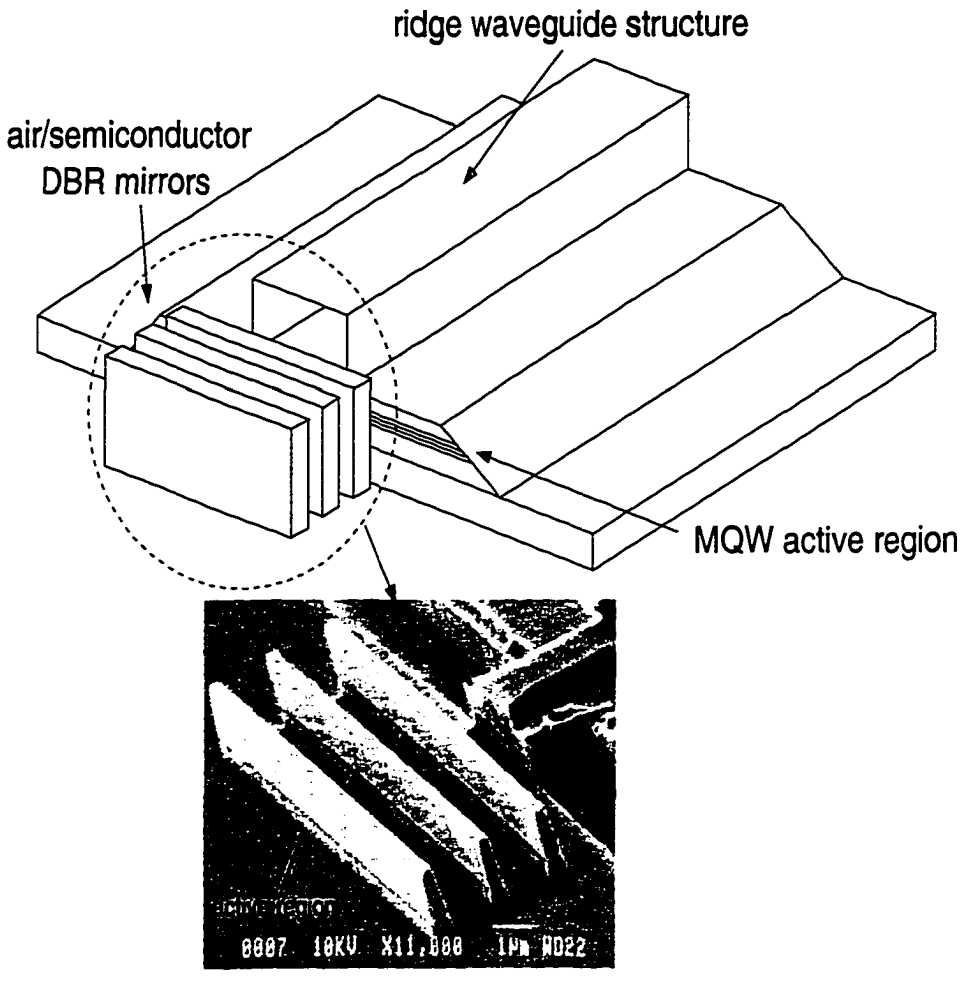


Figure 7.7: A schematic and scanning electron micrograph of the edge emitting laser with air/semiconductor DBR mirror etched via RIE. (From [103])

Reproduced with permission of the copyright owner. Further reproduction prohibited without permission.

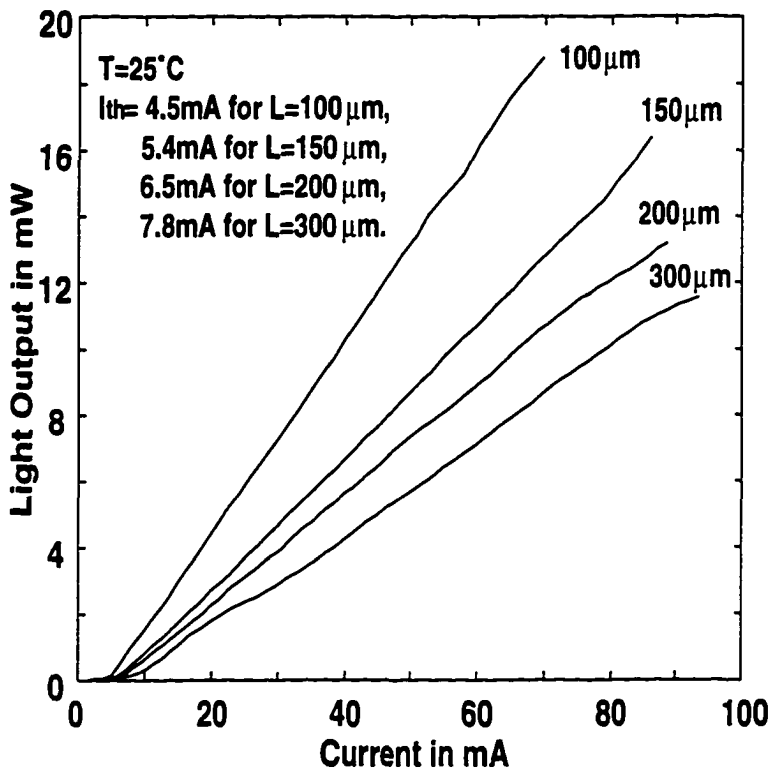


Figure 7.8: Measured L-I characteristics for edge emitting lasers with DBRs on one side. The light output is taken from the cleaved facet. (From [103].)

Reproduced with permission of the copyright owner. Further reproduction prohibited without permission.

CHAPTER VIII

CONCLUSIONS AND RECOMMENDATIONS FOR FUTURE STUDY

In this thesis several studies have been undertaken to better understand how certain physical phenomena affect device performance, and how optoelectronic and optical studies can be used to better optimize and utilize present devices. The work completed in this thesis will now be revisited, followed by suggestions for future work.

8.1 Review of present work

It is desired that the linewidth enhancement factor be minimized in semiconductor laser-based transmission systems due to the increases in linewidth and chirp attributable to α. In Chapter III a study of the effects of strain and temperature on α in InP-based MQW lasers was undertaken. It was seen that both increasing strain and decreasing device operation temperature improve α in the devices studied, attributable to the associated increase in differential gain in these devices.

Increasing the number of QW's in 1.55 μm InP-based devices has been a primary method of overcoming material limitations, especially Auger recombination, in this material system. Generally it is assumed that the carriers are injected uniformly into the active region. For the first time, the effects of non-uniform injection are examined

Reproduced with permission of the copyright owner. Further reproduction prohibited without permission.

with respect to operating characteristics of InP-based lasers, in order to see whether non-uniform injection degrades performance, In Chapter IV it is found that device performance does not significantly degrade, due to the compensatory effects of the wells receiving more holes than electrons under non-uniform injection.

In order to overcome the limiting factor of laser operation in a pulse code modulation scheme, the carrier recovery time from a gain-switched pulse, a novel transmission system based on time- and space-division multiplexing is introduced. In Chapter V, system limitations are examined theoretically and experimentally from the point of a single laser. Large signal modulation of different device structures is carried out, including the large signal modulation of quantum dot lasers for the first time. It is found that, for InP-based lasers, a tunneling-injection structure is more suitable in this type of application than an SCH structure, due to enhanced differential gain and improved injection efficiency. Investigation on QD devices reveal its potential as a low power, short pulse optical source, producing the shortest ($\sim$35 ps) pulses of the devices tested with zero additional DC bias apart from the feedthrough of the pulse source.

In order to investigate laser phenomena from a waveguiding viewpoint, two- and three-dimensional waveguiding formalism and the associated computational implementaion is discussed and demonstrated in Chapter VI. As an example of its use, the 2D simulator is applied to the modeling and experimental analysis of a 1.54 μm InP-based integrated laser-modulator. Results from the simulator are found to be in close agreement with experimentally-obtained measurements. A simple application of the 3D simulator is performed, illuminating the possibilities of future 3D studies.

In OEIC's it is desirable to reduce the transmitter size for many reasons, including the reduction of parasitics, improved device density. Reduction of the laser cavity

Reproduced with permission of the copyright owner. Further reproduction prohibited without permission.

length for an edge emitting laser with a semiconductor/air facet is generally unacceptable because of the increased mirror loss associated with reduction in cavity length. Noting that vertical cavity lasers incorporate a DBR mirror stack to reduce the mirror losses, in Chapter VII an edge emitting laser using a short air/semiconductor DBR stack is exhaustively modeled using the 2D simulator of Chapter VI. Including design and processing uncertainties, including aperiodic spacing of the DBR stack and off-design wavelength lasing, only two mirrors are found necessary to obtain a maximum in reflectivity, and thus a minimum in mirror loss. Simulations also show that wave divergence is the limiting factor prohibiting higher reflectivities than the best obtained in Chapter VI. Experimental results match very well with theoretical data, suggesting that the models used are indeed valid.

8.2 Suggestions for future work

The linewidth enhancement factor plays a major role in long-haul communication systems since the dispersion of the pulse during propagation through a fiber is dependent on α. In Chapter III it was seen strain and temperature reduce α. The analysis presented in Chapter III suggests a structure that can eliminate both plasma dispersion through carrier confinement and anomalous dispersion through enhanceed differential gain would be ideal in lowering α as much as possible. In this case, the device comes to one's mind is a quantum dot laser. At the time of this writing, there have been no studies of α in QD lasers; such a study would be important in determing the role of QD lasers in future fiber communication systems.

Non-uniform injection has been studied theoretically. However, no experimental studiesi have been carried out to determine the degree of non-unform injection in MQW laser. It is expected that for a very large number of wells, those wells farthest

Reproduced with permission of the copyright owner. Further reproduction prohibited without permission.

from a respective injection side will have few corresponding carriers from that injection side, and will be absorbing light rather than producing gain. An experimental study characterizing the non-uniform distribution of carriers in the wells would be useful in determining a limit as to what a maximum number of wells would be before the expected downturn due to absorption within the active region occurs.

In Chapter VI, the concept of a time- and space-division multiplexed array has been explored theoretically with experimental results focused on the laser. However, many issues have yet to be resolved. The chirp of the laser, while expected to be reduced substantially in the quantum dot laser via the reduction in α, will limit how far the pulse can ultimately travel without the penalty of dispersion. The realization of the high speed multiplexer is a challenging design issue. Additionally, the design of the gain-switching mechanism, either using an on-chip pulse generator like the step-recovery diode used in Chapter V, or an tapered energy-storage section in the laser itself [105] allowing gain switching, needs to be addressed as well.

Potential applications for the 2D and 3D simulators described in Chapter VI, abound. Examination of novel inner and outer cladding layer design to reduce near- and far-field patterns [106] can be easily investigated using the 2D simulator. Another interesting 2D investigation can be done in polar coordinates. In Chapter VII, a short air/semiconductor DBR stack was used to increase the reflectivity of the cavity end. A novel device concept would then extend this approach to VCSEL's. In Fig. 8.1 is the conceptualized approach to possible fabricate such a device. Figure 8.1(a) shows a 3 period AlAs/GaAs stack on the device surface, either GaAs- or InP-based. Atop the GaAs has been deposited, in "C" shapes, material to be used as an intermixing agent such as Si_3N_4 [107], [108]. After the intermixing, the VCSEL is etched with an AlAs-preferential solution (BHF), creating an air gap, as in Fig.

Reproduced with permission of the copyright owner. Further reproduction prohibited without permission.

8.1(b). The C-shaped "pillars" remaining in the AlAs mirror regions support the GaAs mirrors above them. Such a mirror stack would theoretically give a high (99%) reflectivity due to the large semiconductor/air difference. Because the active region in the vertical direction is defined essentially by the mirrors and the current injection, the effect of light divergence is expected to be negligible. Additionally, the doped region due to intermixing may be suitable for contact formation as well [104].

Several applications exist for the 3D simulator with microcavity and ring waveguide structures being among them. Extending again from the work in Chapter VII. as the current stripe narrows, the lateral (y-) direction will no longer be negligible compared to the growth (x-) direction. A 3D simulation is therefore appropriate. Fig. 8.2(a) and (b) show the 3D and 2D (top view) projections of the device, essentially the same as that studied in Chapter VII. Since wave divergence will now occur in the lateral direction has well, the use of curved mirrors, as in Fig 8.2(c) may be studied in order to elicit optimal design of the curved mirror structure. In addition, the vertical and horizontal near- and far-field patterns may be studied for novel devices. The design of such OEIC components such as couplers, T-junctions, and Bragg gratings may also be fully examined with the 3D simulator. Though at current writing the simulator may take a very long time ($\sim$ days), the progress of the computer industry makes it fathomable that even within a short time (i.e, within two years) that a highly detailed simulations will be accomplished using this (or a variant of this) on a single workstation within hours.

Reproduced with permission of the copyright owner. Further reproduction prohibited without permission.

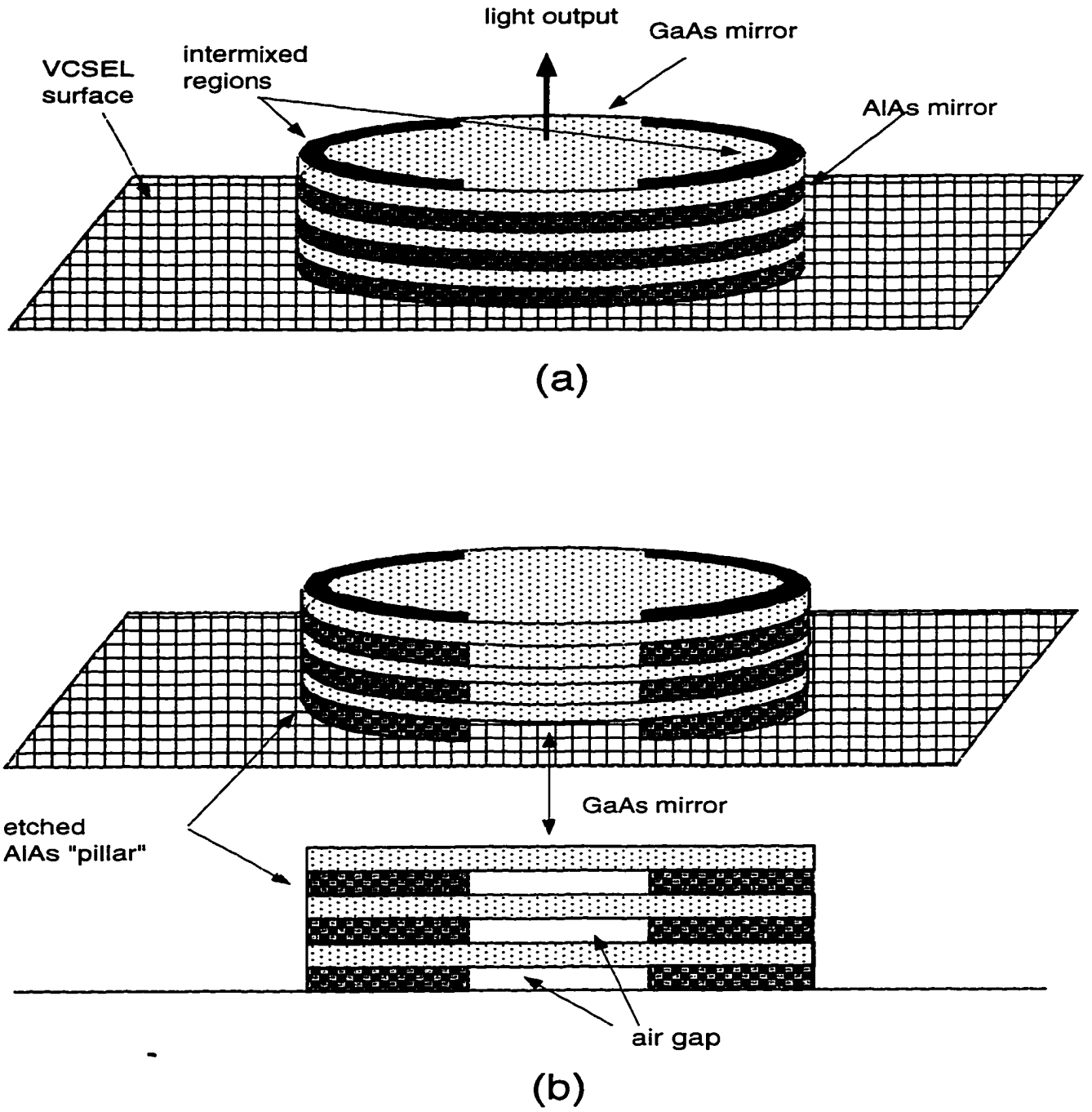


Figure 8.1: Envisioned short-period VCSEL examining (a) 3D view of mirror stack before etch with intermixing region shown, (b) 3D and 2D views of mirror stack after etch.

Reproduced with permission of the copyright owner. Further reproduction prohibited without permission.

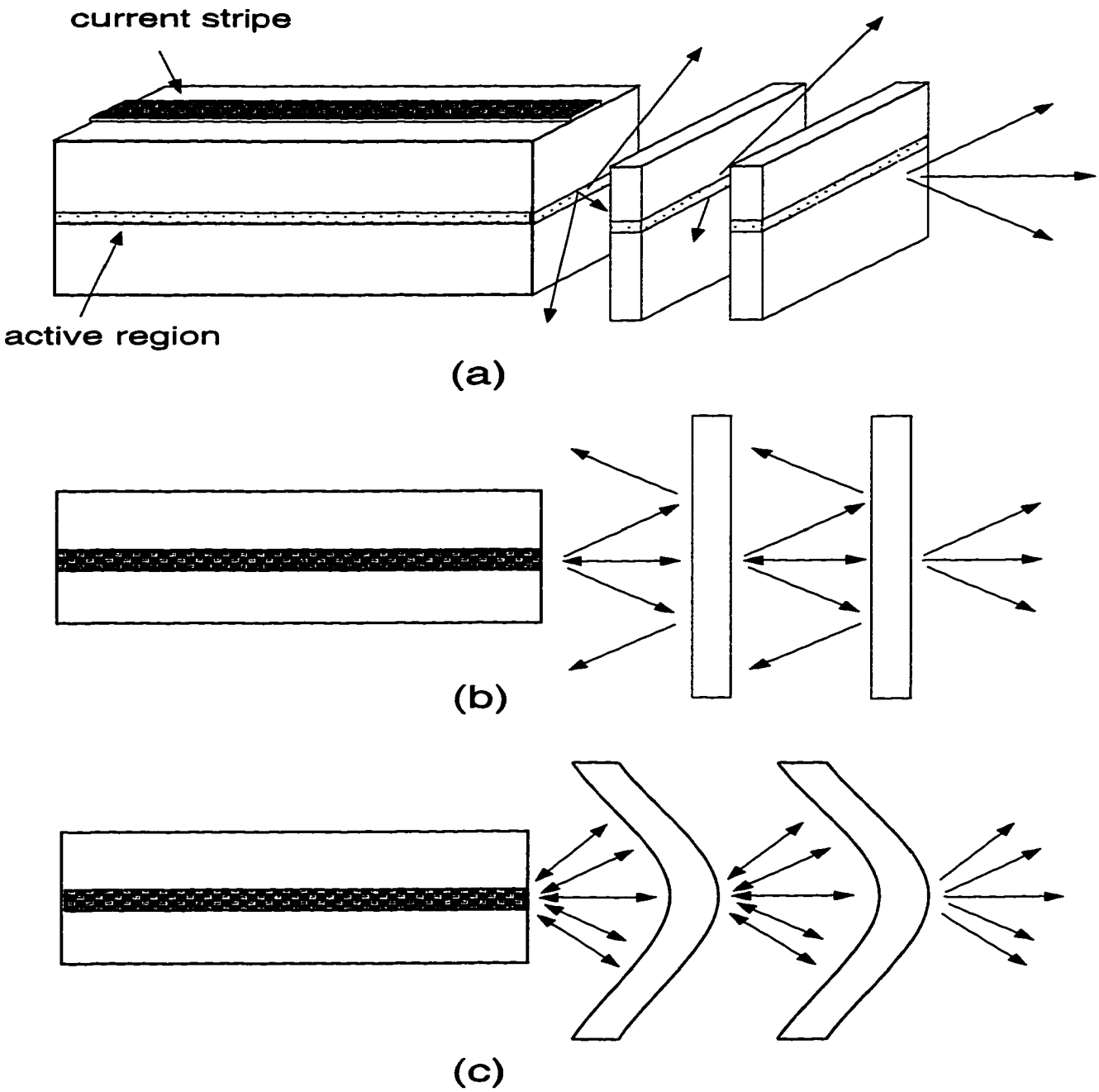


Figure 8.2: Edge emitting laser with DBR showing (a) 3D view of structure using flat mirrors as in Chapter VII, (b) top view of structure in (a), and (c) top view of structure in (a) with curved mirrors. The arrows are meant to emulate the light emerging from and being reflected by the laser cavity and the mirrors.

Reproduced with permission of the copyright owner. Further reproduction prohibited without permission.

APPENDICES

Reproduced with permission of the copyright owner. Further reproduction prohibited without permission.

APPENDIX A

THE DEPENDENCE OF LINEWIDTH ON THE LINEWIDTH ENHANCEMENT FACTOR

In Chapter II the effects of temperature and strain on the linewidth enhancement factor T were investigated. In this appendix the derivations for the dependence of α on the index of refraction n and carrier density N and the $1 + \alpha^2$ dependence of linewidth on α are given. This derivation follows [14].

A.1 Derivation of the linewidth enhancement factor

The linewidth enhancement factor has two contributing factors: 1) changes in the active medium refractive index from changes in the gain of the medium, known as *anomalous* dispersion, and 2) changes in the active medium refractive index due to carrier movement caused by the optical field, known as free carrier or *plasma* dispersion [32]. Each of these will be treated separately, in the following.

A.1.1 Anomalous dispersion

In the laser (Fabry-Perot) cavity, the intensity of the photon field after propagating a roundtrip distance of $2l$ can be expressed as

$$|E(2l)|^2 = |E(0)|^2 e^{(g-\alpha_l)(2l)}, \tag{A.1}$$

Reproduced with permission of the copyright owner. Further reproduction prohibited without permission.

where g denotes the gain of the medium, and α_l represents the cavity and mirror losses. Assuming the propagating field can be expressed as a plane wave, $E(z) = E(0)e^{jkz}$, where $k = \frac{\omega n}{c}$, k being the complex wavevector. The complex refractive index n is expressed $n = n_R - in_I$, where n_R and n_I represent the real and imaginary parts of the index of refraction, respectively. Then, after a distance $2l$,

$$g - \alpha_l = -\frac{2\omega n_I}{c}. \tag{A.2}$$

At threshold, $g = \alpha_l$, $\epsilon_r = n^2$ is real, where the complex permittivity is $\epsilon = \epsilon_r \epsilon_0$. Changes in ϵ_r due to changes in carrier density N can then expressed, to first-order, as

$$\begin{aligned}
\epsilon_r(n_{\text{th}} + \Delta n_R - i\Delta n_I) &= (n_{\text{th}} + \Delta n_R - i\Delta n_I)^2 \\
&= (n_R + \Delta n_R - i\Delta n_I)^2 \\
&\approx n_R^2 + 2n_R(\Delta n_R - i\Delta n_I) \\
&\approx n_R^2 + 2n_R\Delta n_I(\alpha - i) \\
&\approx n_R^2 - i2n_R\Delta n_I(1 + i\alpha), \qquad \text{(A.3)} \\
& \qquad \text{(A.4)}
\end{aligned}$$

where the linewidth enhancement factor (no subscript) $\alpha \equiv \frac{\Delta n_R}{\Delta n_I}$. Note that the second order terms (products of two perturbations) have been discarded. A perturbation in the carrier density around threshold results in a change in the gain. From Eq. (A.2), the corresponding change in Δn_I is

$$\Delta n_I = -\frac{c}{2\omega}\Delta g \tag{A.5}$$

or

$$\frac{dn_I}{dN} = -\frac{c}{2\omega}\frac{dg}{dN} \tag{A.6}$$

Reproduced with permission of the copyright owner. Further reproduction prohibited without permission.

for $N \rightarrow 0$.

Through the Kramers-Kronig (K-K) relations, a change in the real part of the refractive index Δn_R can be related to Δn_I. The K-K relation is an application of the Cauchy integral [33] where the real and imaginary parts of a complex function $f(z)$ can be related to each other, provided $f(z) \rightarrow 0$ as $z \rightarrow \infty$, $z = x + iy$. The relations are, for $f(x_0) = u(x_0) + iv(x_0)$, [34]

$$u(x_0) = \frac{2}{\pi} P \int_0^\infty \frac{xv(x)}{x^2 - x_0^2} dx, \tag{A.7}$$

$$v(x_0) = -\frac{2}{\pi} P \int_0^\infty \frac{x_0 u(x)}{x^2 - x_0^2} dx, \tag{A.8}$$

where P represents the Cauchy principle value and it is assumed $f(z)$ is symmetric about the y- axis. The symmetry is important since only non-negative real frequencies physically exist. Because $n^2 \rightarrow 1$ as $\omega \rightarrow \infty$, the K-K relations cannot be used to solve directly for $\frac{dn}{dN}$ in a strict sense. Therefore, the complex susceptibility $\chi = n^2 - 1$ is used instead, where it can be seen from Eq. (A.4) $\Delta\chi = 2n_R \Delta n_I$. From this, α_a, the linewidth enhancement factor contribution from anomalous dispersion, can be written as [35]

$$\alpha_a = \frac{d\chi_R}{d\chi_I} \tag{A.9}$$

where

$$\frac{d\chi_I(N, E_l}{dN} = \int_0^\infty dE \frac{dg(N, E)}{dN} \frac{\hbar/T_2}{(E - E_l)^2 + (\hbar/T_2)^2}, \tag{A.10}$$

and, through the K-K relations,

$$\frac{d\chi_R(N, E_l}{dN} = \int_0^\infty dE \frac{dg(N, E)}{dN} \frac{(E - E_l}{(E - E_l)^2 + (\hbar/T_2)^2}, \tag{A.11}$$

where E_l is the lasing wavelength, and a Lorentzian function has been introduced to include collision broadening, whose time is given as T_2 If $T_2 = \infty$, the K-K relations as defined in Eqs. (A.7)-(A.8) are obtained.

Reproduced with permission of the copyright owner. Further reproduction prohibited without permission.

A.1.2 Plasma dispersion

In addition to the anomalous dispersion there is an additional contribution to α from a change in N due to carrier movement caused by the optical field. The movement induces a polarization $\mathbf{P}$ [32],

$$\mathbf{P} = -\frac{q^2}{\omega^2}\frac{N}{m_r^* m_0}\mathbf{E}, \tag{A.12}$$

where q is the electron charge, omega is the optical frequency in radians, m_r^* is the (unitless) reduced mass of a hole-electron pair, and $\mathbf{E}$ is teh electric field vector. (The reduced mass is evaluated numerically from the density of states function.) The change in n_R is the

$$\Delta n_R = -\frac{r_0 N}{2\pi E^2 n m_r^* m_0}. \tag{A.13}$$

where r_0 is the classical electron radius, E is the photon energy, and n is the refractive index. Combining $\alpha \equiv \frac{\Delta n_R}{\Delta n_I}$ and Eq. (A.2 yields Eq. α_p, the contribution to α from plasma dispersion, [37],[40]

$$\alpha_p(\lambda_l) = \frac{q^2 \lambda_l}{2pi\epsilon_0 n c^2 m_r^* m_0}\left(\frac{dg(N,\lambda_l)}{dN}\right)^{-1}, \tag{A.14}$$

where λ_l is the lasing wavelength. Then,

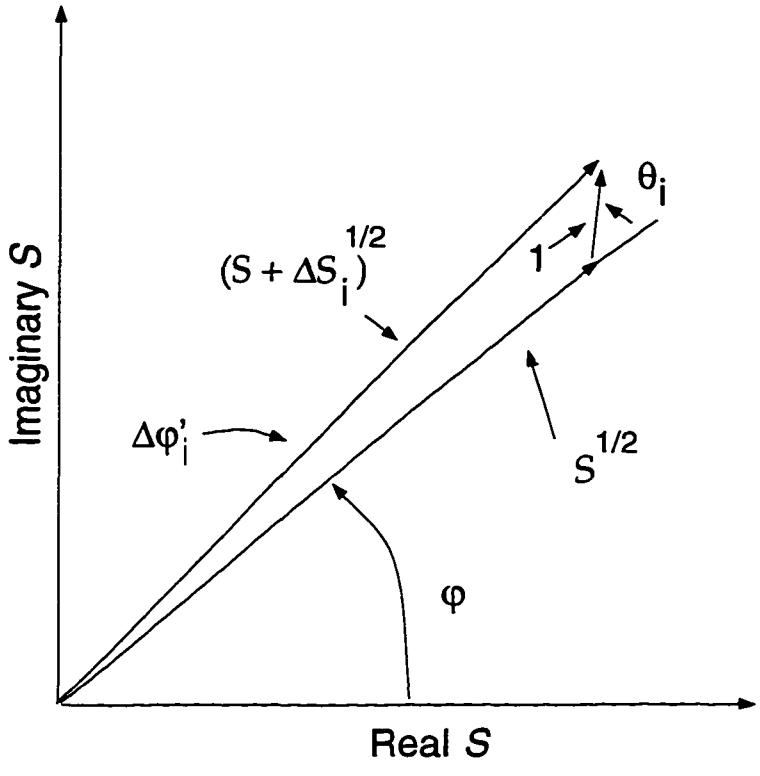
$$\alpha(\lambda_l) = \alpha_a(\lambda_1) + \alpha_p(\lambda_l). \tag{A.15}$$

A.2 Sources of phase fluctuations

Refer to the Figure on page 167 (after [14]). The photon field is represented by complex amplitude $E(t)$ so that the intensity $S = E^* E$ also equals the number of photons in the cavity

$$E(t) = S(t)^{\frac{1}{2}} e^{i\phi}, \tag{A.16}$$

Reproduced with permission of the copyright owner. Further reproduction prohibited without permission.



where $\phi(t)$ represents the phase of the photon field. The i^{th} spontaneous emission event is then assumed to change the magnitude E by ΔE_i, where ΔE_i has unit magnitude and random phase as

$$\Delta E_i = e^{i\phi+\theta_i} \tag{A.17}$$

where θ_i represents a random phase change. The assumption that ΔE_i has unit magnitude is justified since it leads to the correct average rate of increase in S due to spontaneous emission and the Langevin noise sources for S and ϕ. The total phase change for many spontaneous emission events is then assumed to be the sum of the phase changes $\Delta\phi_i$.

There are two contributions to $\Delta\phi_i$. In the Figure, the change $\Delta\phi'$ is due to the out of phase component of ΔE_i. This change is

$$\Delta\phi_i' = S^{-\frac{1}{2}} \sin\theta_i. \tag{A.18}$$

Reproduced with permission of the copyright owner. Further reproduction prohibited without permission.

The second contribution is due to the intensity change and the fact that intensity and phase changes are coupled (derived in the next section). As seen from the Figure, an amplitude change from $E^{\frac{1}{2}}$ to $(E+\Delta E_i)^{\frac{1}{2}}$ yields

$$\Delta E_i = 1 + 2E^{\frac{1}{2}}\cos\theta_i \tag{A.19}$$

The average of the second term in Eq. (A.19) averages to zero, so on average spontaneous emission causes a field intensity change of adding one photon to the i^{th}. The contribution $\Delta\phi''$ involves knowing the phase rate equation $\dot{\phi} = \frac{\partial\Delta\varphi}{\partial t}$, which is derived in the following section.

A.3 Derivation of the phase rate equation

The wave equation for the photon field (as given in Section 5.2) is

$$\frac{\partial^2 E}{\partial z^2} = \frac{1}{c^2}\frac{\partial^2(\epsilon E)}{\partial t^2}, \tag{A.20}$$

where

$$E(t) = S^{\frac{1}{2}}(t)e^{-i(\omega t+\phi)} + c.c. \tag{A.21}$$

To first order, dispersion can be accounted for by expanding ϵE around the optical frequency ω as

$$\epsilon E \sim \left(\epsilon(\omega)S^{\frac{1}{2}} + i\frac{\partial\epsilon}{\partial\omega}\dot{S}^{\frac{-1}{2}}\right)e^{-i(\omega t+\phi)} + c.c. \tag{A.22}$$

Inserting this result into Eq. (A.20) yields for $\dot{S^{\frac{1}{2}}}$, to first order,

$$\frac{2i\omega}{c^2}\left(\epsilon + \frac{\omega}{2}\frac{\epsilon}{\omega}\right)\dot{S}^{\frac{1}{2}} = \left(\frac{\omega^2}{c^2}\epsilon - k^2\right)S^{\frac{1}{2}} \tag{A.23}$$

At threshold, ϵ is real, so

$$\epsilon + \frac{\omega\partial\epsilon}{2\partial\omega} = n_R(n_R + \omega\frac{\partial n_R}{\partial\omega} = \frac{c}{v_g}n_R. \tag{A.24}$$

Reproduced with permission of the copyright owner. Further reproduction prohibited without permission.

where c is the speed of light *in vacuo* and v_g is the group velocity of light in the active medium. The relations derived in Section 3.2 relating $\epsilon(N)$ and $n(N)$ at threshold are repeated here,

$$\frac{\omega n_R}{c} = k, \tag{A.25}$$

$$\epsilon_r(n_{\rm th} + \Delta n_R - i\Delta n_I) \approx n_R^2 - i2n_R\Delta n_I(1 + i\alpha), \tag{A.26}$$

and $\dot{S^{\frac{1}{2}}}$ becomes

$$\begin{aligned} \dot{S^{\frac{1}{2}}} &= \frac{-\omega}{c} v_g \Delta n_I (1 + i\alpha) S^{\frac{1}{2}} \\ &= \frac{(g - \alpha_\gamma) v_g}{2} (1 + i\alpha) S^1 2 \end{aligned} \tag{A.27}$$

Then, using $S = EE^*$, and $E = E^* e^{i\frac{\phi}{2}}$, the rate equations for the intensity and phase of the field are

$$\dot{S} = v_g(g - \alpha_\gamma)S, \tag{A.28}$$

$$\dot{\phi} = \frac{\alpha v_g}{2}(g - \alpha_\gamma). \tag{A.29}$$

A.4 Linewidth enhancement

Combining Eqs. (A.28) and (A.29) the phase rate of change is

$$\dot{\phi} = \frac{\alpha}{2S}\dot{S} \tag{A.30}$$

Let $S(0) = S_0 + \Delta S$ and $S(\infty) = S_0$, where S_0 represents the steady-state intensity and ΔS represents the amplitude of initial intensity fluctuations, as in the case of, for example, laser turn-on. Then,

$$\begin{aligned} \Delta\phi_i'' &= -\frac{\alpha}{2S}\Delta S_i \\ &= -\frac{\alpha}{2S}(1 + 2S^{\frac{1}{2}}\cos(\theta_i) \end{aligned} \tag{A.31}$$

Reproduced with permission of the copyright owner. Further reproduction prohibited without permission.

The total phase change is the sum of the two contributions

$$\begin{aligned}\Delta\phi_i &= \Delta'_{phi} + \Delta''_{phi} \\ &= -\frac{\alpha}{2S} + \frac{1}{S^{\frac{1}{2}}}(\sin\theta_i - \alpha\cos\theta_i) \end{aligned} \tag{A.32}$$

The term $\Delta\phi'$ denotes a constant phase change. For an average spontaneous emission rate R, the average phase change over a time t is

$$\Delta\phi' = -\frac{\alpha R t}{2S} \tag{A.33}$$

The total phase fluctuation for $N = Rt$ events will be

$$\Delta\phi'' = \sum_{i=1}^{N} S^{-\frac{1}{2}}(\sin\theta_i - \alpha\cos\theta_i). \tag{A.34}$$

For random angles the average of all of the cross terms vanishes and

$$\Delta\phi^2 = \frac{R(1+\alpha^2)t}{2S}. \tag{A.35}$$

From the nature of spontaneous emission events the phase ϕ has a Gaussian probability density. Then [63]

$$< E^*(t)E(0) >= |E(0)|^2 e^{-\frac{|t|}{t_{coh}}} \tag{A.36}$$

where the coherence time t_{coh} is given by $\Delta t_{coh} = \frac{<\Delta\phi^2>}{2t}$. The power spectrum of the laser can be obtained for the Fourier transform of $< E^*(t)E(0 >$, and is found to be spectrum is Lorentzian, with a linewidth $\delta\nu$

$$\delta\nu = \frac{1}{\pi t_{coh}} = \frac{R}{4\pi S}(1+\alpha^2). \tag{A.37}$$

Thus, the linewidth depends on α as $1+\alpha^2$.

Reproduced with permission of the copyright owner. Further reproduction prohibited without permission.

APPENDIX B

IMPROVEMENT OF STABILITY FOR THE PARABOLIC TWO-DIMENSIONAL WAVE EQUATION USING THE SLOW-WAVE APPROXIMATION

The equation to be solved, for the TE-mode, is

$$\frac{\partial \vec{E}}{\partial t} = \frac{i\omega_0}{2}\left\{\vec{E} - \frac{\vec{\nabla} \times \vec{\nabla} \times \vec{E}}{\omega_0^2 \mu\epsilon}\right\}, \tag{B.1}$$

For simplicity, a one-dimensional (x-direction) system is assumed, since the treatment can easily be extended to the two dimensional systems presented in Chapters VI and VII. Assuming that the electric susceptibility ϵ and the magnetic permeability μ are constant in space, Eq. (B.1) becomes

$$\frac{\partial E}{\partial t} = \frac{i\omega_0}{2}\left\{E + \frac{\nabla^2 E}{\omega_0^2 \mu\epsilon}\right\}, \tag{B.2}$$

where the subscript x has been dropped for notational ease. Noting that

$$E(t + \Delta t) = E(t) + \Delta t \frac{\partial E}{\partial t} + \frac{(\Delta t)^2}{2}\frac{\partial^2 E}{\partial t^2} + \cdots, \tag{B.3}$$

then

$$E(t + \Delta t) = \exp\left(\Delta t \frac{\partial}{\partial t}\right) E(t), \tag{B.4}$$

or

$$\exp\left(-\frac{\Delta t}{2}\frac{\partial}{\partial t}\right) E(t + \Delta t) = \exp\left(\frac{\Delta t}{2}\frac{\partial}{\partial t}\right) E(t) \tag{B.5}$$

Reproduced with permission of the copyright owner. Further reproduction prohibited without permission.

which, expanded to first order, becomes

$$\left(1-\frac{\Delta t}{2}\frac{\partial}{\partial t}\right)E(t+\Delta t)=\left(1+\frac{\Delta t}{2}\frac{\partial}{\partial t}\right)E(t), \tag{B.6}$$

which is also known as the *Pade* approximation. Denoting $E_m^{n+1} = E_m(t+\Delta t)$, $E_m^n = E_m(t)$, we have

$$\left(1-\frac{\Delta t}{2}\frac{\partial}{\partial t}\right)E_m^{n+1}=\left(1+\frac{\Delta t}{2}\frac{\partial}{\partial t}\right)E_m^n. \tag{B.7}$$

Using Eq.(A.2) in Eq.(A.7), we obtain

$$\begin{aligned} &E_m^{n+1}-\left(\frac{\Delta t}{2}\right)\left(\frac{i\omega_0}{2}\right)\left\{E_m^{n+1}+\frac{E_{m+1}^{n+1}-2E_m^{n+1}+E_{m-1}^{n+1}}{(\Delta x)^2}\right\} \\ &\quad = E_m^n+\left(\frac{\Delta t}{2}\right)\left(\frac{i\omega_0}{2}\right)\left\{E_m^n+\frac{E_{m+1}^n-2E_m^n+E_{m-1}^n}{(\Delta x)^2}\right\} \end{aligned} \tag{B.8}$$

where the operator ∇^2 has been expanded as a difference scheme. According to von Neumann, the error in a numerical finite-difference approach can be written in a Fourier series

$$Z=\sum e^{\alpha n}e^{j\beta m} \tag{B.9}$$

where Z is defined as the difference between the exact and computed answers. For the total error to remain bounded, $\forall n,m$,

$$\left|e^{\alpha n}e^{j\beta m}\right|\leq 1. \tag{B.10}$$

This yields the condition

$$\left|e^{\alpha n}\right|\leq 1 \qquad \forall n. \tag{B.11}$$

Expanding Eq. (A.8) in terms of Z, we may write

$$\begin{aligned} &Z_m^{n+1}-\left(\frac{\Delta t}{2}\right)\left(\frac{i\omega_0}{2}\right)\left\{Z_m^{n+1}+\frac{Z_{m+1}^{n+1}-2Z_m^{n+1}+Z_{m-1}^{n+1}}{(\Delta x)^2}\right\} \\ &\quad = Z_m^n+\left(\frac{\Delta t}{2}\right)\left(\frac{i\omega_0}{2}\right)\left\{Z_m^n+\frac{Z_{m+1}^n-2Z_m^n+Z_{m-1}^n}{(\Delta x)^2}\right\}, \end{aligned} \tag{B.12}$$

Reproduced with permission of the copyright owner. Further reproduction prohibited without permission.

or, after some algebra,

$$e^{\alpha} = \frac{1 + \left(\frac{\Delta t}{2}\right)\left(\frac{i\omega_0}{2}\right) + \left(\frac{i\Delta t}{4\omega_0\mu\epsilon(\Delta x)^2}\right)(2\cos\beta - 2)}{1 - \left(\frac{\Delta t}{2}\right)\left(\frac{i\omega_0}{2}\right) - \left(\frac{i\Delta t}{4\omega_0\mu\epsilon(\Delta x)^2}\right)(2\cos\beta - 2)}, \tag{B.13}$$

where Eq. (A.9) has been substituted for. Since $2\sin^2\frac{\beta}{2} = 1 - \cos\beta$, Eq. (A.13) becomes

$$e^{\alpha} = \frac{1 + \left(\frac{\Delta t}{2}\right)\left(\frac{i\omega_0}{2}\right) - \left(\frac{i\Delta t}{\omega_0\mu\epsilon(\Delta x)^2}\right)\sin^2\frac{\beta}{2}}{1 - \left(\frac{\Delta t}{2}\right)\left(\frac{i\omega_0}{2}\right) + \left(\frac{i\Delta t}{\omega_0\mu\epsilon(\Delta x)^2}\right)\sin^2\frac{\beta}{2}}. \tag{B.14}$$

Using the condition given by Eq. (A.11), we obtain

$$\begin{aligned} &1 + \left(\frac{\Delta t}{2}\right)\left(\frac{i\omega_0}{2}\right) - \left(\frac{i\Delta t}{\omega_0\mu\epsilon(\Delta x)^2}\right)\sin^2\frac{\beta}{2} \\ &\leq 1 - \left(\frac{\Delta t}{2}\right)\left(\frac{i\omega_0}{2}\right) + \left(\frac{i\Delta t}{\omega_0\mu\epsilon(\Delta x)^2}\right)\sin^2\frac{\beta}{2}. \end{aligned} \tag{B.15}$$

Equation (A.15) is rewritten

$$\frac{\Delta t(i\omega_0)}{2} \leq \left(\frac{2i\Delta t}{\omega_0\mu\epsilon(\Delta x)^2}\right)\sin^2\frac{\beta}{2}, \tag{B.16}$$

or

$$(\Delta x)^2 \leq \frac{4\sin^2\frac{\beta}{2}}{\omega_0^2\mu\epsilon}. \tag{B.17}$$

But β is arbitrary, depending on the series expansion. Hence a maximum bound acceptable for convergence cannot be established, since $\sin^2\frac{\beta}{2}$ may be arbitrarily small.

To circumvent this situation, we make the substitution

$$U(x,t) = e^{\frac{-i\omega_0 t}{2}} E(x,t), \tag{B.18}$$

which causes a change in phase but does not affect the magnitude of the field envelope. From this,

$$\frac{\partial U(x,t)}{\partial t} = e^{\frac{-i\omega_0 t}{2}} \frac{\partial E(x,t)}{\partial t} - \frac{i\omega_0}{2} e^{\frac{-i\omega_0 t}{2}} E(x,t). \tag{B.19}$$

Reproduced with permission of the copyright owner. Further reproduction prohibited without permission.

Equation (A.2) then is transformed to

$$\frac{\partial U}{\partial t} = \frac{i}{2\omega_0 \mu \epsilon} \frac{\partial^2 U(x,t)}{\partial x^2}. \tag{B.20}$$

Equation (A.12) is now written

$$\begin{aligned} & Z_m^{n+1} - \left(\frac{\Delta t}{2}\right)\left(\frac{i\omega_0}{2}\right)\left\{\frac{Z_{m+1}^{n+1} - 2Z_m^{n+1} + Z_{m-1}^{n+1}}{(\Delta x)^2}\right\} \\ & = Z_m^n + \left(\frac{\Delta t}{2}\right)\left(\frac{i\omega_0}{2}\right)\left\{\frac{Z_{m+1}^n - 2Z_m^n + Z_{m-1}^n}{(\Delta x)^2}\right\}. \end{aligned} \tag{B.21}$$

Similarly, Eq. (A.14) becomes

$$e^{\alpha} = \frac{1 - \left(\frac{i\Delta t}{\omega_0 \mu \epsilon (\Delta x)^2}\right)\sin^2\frac{\beta}{2}}{1 + \left(\frac{i\Delta t}{\omega_0 \mu \epsilon (\Delta x)^2}\right)\sin^2\frac{\beta}{2}}. \tag{B.22}$$

This result, unlike Eq. (A.15), satisfies the condition of Eq. (A.11). Therefore the field U allows the numerical technique unconditonal stability in the von Neumann sense without loss of information.

Reproduced with permission of the copyright owner. Further reproduction prohibited without permission.

APPENDIX C

POTENTIAL LOCALLY ONE-DIMENSIONAL FINITE DIFFERENCE TIME DOMAIN SCHEMES FOR FULLY-VECTORIAL THREE DIMENSIONAL SIMULATIONS

In Chapter VI an iterative method for fully-vectorial (FV) FDTD simulations was described and implemented. The method is attractive for primarily two reasons: simplicity and flexibility. The implementation of the implicit formulation is straightforward. Flexibility is attained through both the use of the slow-wave approximation and the moving simulation region, reducing memory overhead and computation time. However, the method still has serious drawbacks. For example, although the magnitude of the residual error vector after m iterations at some time step n may be small ($\sim 10^{-15}$), the rate of convergence per iteration slows, especially as a wavefront approaches a large refractive index difference. In addition, although overrelaxation can speed convergence, finding the proper relaxation factor may involve significant trial-and-error.

In the two-dimensional simulations of Chapters VI and VII, the locally one-dimensional (LOD) scheme was introduced in order to provide a computationally efficient algorithm, since only a tridiagonal matrix need be inverted to solve the electric field profile at a given half-time step. This scheme allows for both savings

Reproduced with permission of the copyright owner. Further reproduction prohibited without permission.

in memory and in time. However, the FV three-dimensional (3D) problem does not have such an obvious counterpart, due to the inability to uncouple to polarizations.

In Chapters VI and VII the slowly-varying envelope approximation is used to remove the second differentiation of the electric field with respect to time, resulting in a large savings of memory as only the previous timesteps data is needed. Furthermore, in Appendix B it is shown that a phase extraction equal to one-half the propagating frequency ω_0 ensures that the slowly-varying envelope approximation, when locally applied, will be bounded in a von Neumann sense $\forall t$. Applying the slowly-varying envelope approximation to the FV 3D problem yields

$$\frac{\partial \vec{E}}{\partial t} = \frac{i\omega_0}{2}\left(\vec{E} - \frac{\vec{\nabla} \times \vec{\nabla} \times \vec{E}}{\omega_0^2 \mu_0 \epsilon(\mathbf{r})}\right). \tag{C.1}$$

Setting $\vec{U} = \vec{E}e^{-\frac{j\omega_0 t}{2}}$ and substituting into Eq. (C.1) yields

$$\frac{\partial \vec{U}}{\partial t} = \frac{i}{2\omega_0^2 \mu_0 \epsilon(\mathbf{r})} \vec{\nabla} \times \vec{\nabla} \times \vec{U}. \tag{C.2}$$

The field $\vec{U}$ is expressed as $\vec{U}(\mathbf{r}) = U_x\hat{x} + U_y\hat{y} + U_z\hat{z}$. Expanding Eq. (C.2) in terms of the x-polarization gives

$$\begin{aligned} \frac{\partial U_x}{\partial t} = \frac{i}{2\omega_0 \mu\epsilon}\Big(&\frac{\partial U_x}{\partial x}\frac{\partial \ln \epsilon}{\partial x} + U_x \frac{\partial^2 \ln \epsilon}{\partial x^2} + \frac{\partial U_y}{\partial x}\frac{\partial \ln \epsilon}{\partial y} + \\ &U_y \frac{\partial^2 \ln \epsilon}{\partial x \partial y} + \frac{\partial U_z}{\partial x}\frac{\partial \ln \epsilon}{\partial z} + U_z \frac{\partial^2 \ln \epsilon}{\partial x \partial z} + \frac{\partial^2 U_x}{\partial x^2} + \frac{\partial^2 U_x}{\partial y^2} + \frac{\partial^2 U_x}{\partial z^2}\Big), \end{aligned} \tag{C.3}$$

Similar equations exist for the $\hat{y}$ and $\hat{z}$ polarizations of $\vec{U}$ as well. It can be seen that local application of the von Neumann stability criterion reveals Eq. (xpol2) to be unconditionally stable.

Reviewing the 2D LOD scheme gives a split for the single polarization E_y:

$$\frac{1}{2}\frac{\partial E_y}{\partial t} = \frac{i}{2\omega_0 \mu_0 \epsilon} \partial^2 E_y \partial x^2, \tag{C.4}$$

$$\frac{1}{2}\frac{\partial E_y}{\partial t} = \frac{i}{2\omega_0 \mu_0 \epsilon} \partial^2 E_y \partial z^2. \tag{C.5}$$

Reproduced with permission of the copyright owner. Further reproduction prohibited without permission.

Summing Eq. (C.4) and (C.5) returns the original 2D equation for E_y as described in Chapter VI.

Applying the same type of method to the component U_x yields

$$\frac{1}{3}\frac{\partial U_x}{\partial t} = \mathcal{L}_x f(\vec{U}) + C_1, \tag{C.6}$$

$$\frac{1}{3}\frac{\partial U_x}{\partial t} = \mathcal{L}_x f(\vec{U}) + C_2, \tag{C.7}$$

$$\frac{1}{3}\frac{\partial U_x}{\partial t} = \mathcal{L}_x f(\vec{U}) + C_3 \tag{C.8}$$

, where $\mathcal{L}_i$ includes the derivatives $\frac{\partial^n}{\partial i^n}$, $i = x, y$ or z, $n = 1, 2$, and $C_{1,2,3}$ is a function of $\vec{U}$ without spatial derivatives.

The split formulae of Eqs. (C.6)-(C.8) can assume several different forms. Two potentially useful splits are discussed below.

C.1 Split 1: Incorporation of known field values at advanced timesteps

From Chapter VI, it is seen that the Jacobi iterative for the $n+1$ timestep is substantially improved when the already known field values $E(x_{1\ldots m})$ at timestep $n+1$ are incorporated into the calculation of the field value at x_{m+1}. Intuitively it would appear that including known field values at time $t = (n+1)\Delta t$ would improve the accuracy of the LOD 3D method as well.

In the spirit of the LOD scheme and the split equations given for U_x in Eqs. (C.6)-(C.8), let

$$\begin{aligned} U^{n+\frac{1}{3}} &= \mathcal{L}_x f(\vec{U}^n) \\ U^{n+\frac{2}{3}} &= \mathcal{L}_x f(\vec{U}^{n+\frac{1}{3}}) \\ U^{n+1} &= \mathcal{L}_x f(\vec{U}^{n+\frac{2}{3}}) \end{aligned} \tag{C.9}$$

Reproduced with permission of the copyright owner. Further reproduction prohibited without permission.

Keeping the tri-diagonal nature of the LOD scheme, and incorporating updated field values of U_y, and U_z at advanced time steps leads to a split

$$\frac{\partial U_x^{n+\frac{1}{3}}}{\partial t} = \frac{i}{2\omega_0\mu\epsilon}\Big(\frac{\partial U_x^n}{\partial x}\frac{\partial \ln\epsilon}{\partial x} + U_x^n\frac{\partial^2 \ln\epsilon}{\partial x^2} + \frac{\partial U_y^n}{\partial x}\frac{\partial \ln\epsilon}{\partial x} + \frac{1}{3}U_y^n\frac{\partial^2 \ln\epsilon}{\partial x\partial y} + \frac{\partial U_z^n}{\partial x}\frac{\partial \ln\epsilon}{\partial z} + \frac{1}{3}U_z^n\frac{\partial^2 \ln\epsilon}{\partial x\partial z} + \frac{\partial^2 U_x^n}{\partial x^2}\Big), \tag{C.10}$$

$$\frac{\partial U_x^{n+\frac{2}{3}}}{\partial t} = \frac{i}{2\omega_0\mu\epsilon}\Big(\frac{1}{3}U_y^{n+\frac{1}{3}}\frac{\partial^2 \ln\epsilon}{\partial x\partial y} + \frac{\partial^2 U_x^{n+\frac{1}{3}}}{\partial y^2} + \frac{1}{3}U_z^{n+\frac{1}{3}}\frac{\partial^2 \ln\epsilon}{\partial x\partial z}\Big), \tag{C.11}$$

$$\frac{\partial U_x^{n+1}}{\partial t} = \frac{i}{2\omega_0\mu\epsilon}\Big(\frac{1}{3}U_y^{n+\frac{2}{3}}\frac{\partial^2 \ln\epsilon}{\partial x\partial y} + \frac{\partial^2 U_x^{n+\frac{2}{3}}}{\partial z^2} + \frac{1}{3}U_z^{n+\frac{2}{3}}\frac{\partial^2 \ln\epsilon}{\partial x\partial z}\Big). \tag{C.12}$$

Note terms such as $U_y^n\frac{\partial^2 \ln\epsilon}{\partial x\partial y}$ are evenly weighted over each one-third time step.

Although in the solution for U_x in this case depends completely on the previous one-third time step, solution for U_y^{n+1} and U_z^{n+1} can incorporate terms $\sim f(U_x^{n+1})$ (in solving for U_y^{n+1}) and $\sim f(U_x^{n+1}, U_y^{n+1})$ (in solving for U_z^{n+1}). Hence, previously computed values at the current step can be used to update other field values in order to improve the simulation's accuracy.

C.2 Split 2: Use of previous field values exclusively at advanced timesteps

Suppose the simulation does not include updated field values in the calculation. The split for U_x can be kept the same, while $U_y^{n+1} \sim f(U_x^{n+\frac{2}{3}}, U_y^{n+\frac{2}{3}}, U_z^{n+\frac{2}{3}})$ and a similar situation for U_z. On the other hand, the method presented in the previous section necessitates that at each one-third time step the calculation of each polarization of U must be done serially, since U_y^{n+1} depends on U_x^{n+1} and so forth. However, if only previously computed values as in this instance at $t = (n+1)\Delta t$ depends solely on $t = (n+\frac{2}{3})\Delta t$, U_x^{n+1},U_y^{n+1},and U_z^{n+1}, can be computed simultaneously, i.e. in parallel. The implication that the LOD scheme can be put to use in a parallel

Reproduced with permission of the copyright owner. Further reproduction prohibited without permission.

manner for this class of problems offers not only a tremendous improvement in computation time but also memory savings, as the entire problem is distributed over, in this simplified case, 3 machines working in parallel at each time-step.

In conclusion, two types of LOD schemes have been introduced for the FV 3D FDTD simulation. The first type calculates the components of the vector field in a serial manner using already updated field values to enhance accuracy. The second type trades off the expected improvement in accuracy for the potential for parallel computation. Although the first is more suited for a single workstation and the second for a network environment, the memory and computational efficiency advantages over the iterative method explored in Chapter VI merits further exploration.

Reproduced with permission of the copyright owner. Further reproduction prohibited without permission.

BIBLIOGRAPHY

Reproduced with permission of the copyright owner. Further reproduction prohibited without permission.

BIBLIOGRAPHY

[1] "Electronics manufacturers re-discover the telephone," http://www.cnn.com/TECH/9701/17/computer.telephone/index.html.

[2] Youssef M. Ibrahim, "As most wired nation, Finland has jump on 21st century," http://search.nytimes.com

[3] K. Y. Lau, N. Bar-Chaim, I. Ury, C. Harder, and A. Yariv. *IEEE J. Quantum Electron.*, **20**, pg. 71, 1984.

[4] T. Ikegami and Y. Suematsu, *Electron. Commun. Jpn* , **53**, pg. 69, 1970.

[5] X. Zhang, A.L.Gutierrez-Aitken, D.Klotzkin, P. Bhattacharya, C.Caneau, and R. Bhat, *Electron. Lett.*, **32**, pg. 1715, 1996.

[6] S. Watanabe, T. Terahara, I. Yokota, T. Naito, T. Chikama, and H. Kuwahara, *IEEE J. Lightwave Tech.*, **11**, pg. 116, 1993.

[7] S. Saito, Y. Yamamoto, and T. Kimura, *Electron. Lett.*, **16**, pg. 826, 1980.

[8] C.A. Brackett, *IEEE J. Select. Areas Commun.* , **8**, pg. 948, 1990.

[9] M. Ohtsu, *Highly Coherent Semiconductor Lasers*, Chapter 6. Boston: Artech House, 1992.

[10] G.P. Agrawal, *Fiber-Optic Communication Systems* . New York: Wiley, 1992.

[11] E. G. Vicente De Vera and B. Glance, *IEEE Photon. Technol. Lett.*, **2**, pg. 781, 1990.

[12] K. Y. Lau, N. Bar-Chaim, I. Ury, C. Harder, and A. Yariv. *Appl. Phys. Lett.***43**, pg. 329, 1984.

[13] T. Morioka, H. Takara, S. Kawanishi, O. Kamatani, K. Takiguchi, K. Uchiyama, M. Saruwatari, H. Takahashi, M. Yamada, T, Kanamori, and H. Ono, *Electron. Lett.*, **32**, pg. 906, 1996.

[14] C. H. Henry, *IEEE J. Quantum Electron.*, **QE-18**, pg. 259, 1982.

Reproduced with permission of the copyright owner. Further reproduction prohibited without permission.

[15] K. Vahara and A. Yariv, *IEEE J. Quantum Electron.*, **QE-19**, pg. 1096, 1983.

[16] A. Yariv, *Quantum Electronics*, third ed., Appendix A. New York: Wiley, 1989.

[17] A. Y. Cho and J. R. Arthur, *Progress in Solid-State Chemistry*, **10**, pg. 157, 1975.

[18] J. Chelikowsky and M. Cohen, *Phys. Rev. B*, **14**, pg. 556, 1976.

[19] J. C. Slater and G. F. Koster, *Phys. Rev. B*, **94**, pg. 1498, 1954.

[20] E. O. Kane, J. Phys. Chem. Solids, **1**, pg. 82, 1956.

[21] E. O. Kane, J. Phys. Chem. Solids, **1**, pg. 249, 1957.

[22] E. O. Kane, *Physics of III-V Compounds*, Chapter 3. New York:Academic (1966).

[23] M. Jaffe and J. Singh, Solid State Comm. **62**, pg. 399, 1987.

[24] M. Jaffe, PhD Thesis, University of Michigan, 1989.

[25] J. Singh, *Physics of Semiconductors and Their Heterostructures*, New York: McGraw-Hill, 1993.

[26] O. Madelung, *Semiconductors: Group IV Elements and III-V Compounds*, New York: Springer-Verlag, 1991.

[27] C. Harder, K. Vahala, and A. Yariv *Appl. Phys. Lett.*, **42**, pg. 328, 1983.

[28] M. W. Fleming and A. Mooradian, *Appl. Phys. Lett.*, **38**, pg. 511, 1981.

[29] C. Henry, *IEEE J. Quantum Electron.*, **QE-18**, pg. 301, 1982.

[30] K. Vahala and A. Yariv, *IEEE J. Quantum Electron.*, **QE-19**, pg. 1096, 1982.

[31] K. Vahala and A. Yariv, *IEEE J. Quantum Electron.*, **QE-18**, pg. 1101, 1982.

[32] C. H. Henry, *J. Appl. Phys.*,**52**, pg. 4457, 1981.

[33] S. Fischer,*Complex Variables*, Chapter 2, Pacific Grove, CA: Wadsworth, 1990.

[34] G. Arfken, *Mathematical Methods for Physicists*, Chapter 7, New York: Academic Press, 1985.

Reproduced with permission of the copyright owner. Further reproduction prohibited without permission.

[35] K. Vahala, L. C. Chiu, S. Margalit, and A. Yariv, *Appl. Phys. Lett.*, **42**, pg. 631, 1983.

[36] A. Kimura, M. Nido, S. Murata, J. Shimizu, K. Naniwae, and A. Suzuki, *IEEE Photon. Technol. Lett.*, **5**, pg. 983, 1993.

[37] K. S. Jepsen, N. Storkfelt, M. Vaa, and K. Stubjaker, *IEEE J. Quantum Electron.*, **30**, pg. 635, 1994.

[38] N. Storkfelt, B. Mikkelsen, D. S. Olesen, M. Yamaguchi, K. E. Stubkjaer, *IEEE Photon. Technol. Lett.*, **3**, pg. 632, 1991.

[39] K. Kikuchi, M. Amano, C. E. Zah, and T. P. Lee, *IEEE J. Quantum Electron.*, **30**, pg. 571, 1994.

[40] T. Yamanaka, Y. Yoshikuni, K. Yokoyama, W. Lui, S. Seki, *IEEE J. Quantum Electron.*, **29**, pg. 1609, 1993.

[41] D. T. Nichols, PhD Thesis, University of Michigan, 1992.

[42] N.K.Dutta, N. Anders-Olsson, H. Temkin, T.Tanbun-Ek, and R. Logan, *IEEE J. Quantum Electron.*, **27**, pg. 678, 1991

[43] N.K. Dutta, H. Temkin, T.Tanbun-Ek, and R.Logan, *Appl. Phys. Lett.*, **57**, pg. 1390, 1990.

[44] P. Zory, *Quantum Well Lasers*, New York: Academic Press, 1993.

[45] B.W. Hakki and T.J.Paoli, *J. Appl. Phys.*, **44**, pg. 4113, 1973.

[46] L. F. Tiemeijer, P. J. A. Thijs, J. J. M. Binsma, and T. v. Dongen, *Appl. Phys. Lett.*, **60**, pg. 2466, 1992.

[47] L. J. Davis, PhD Thesis, University of Michigan, 1994.

[48] H. Yoon, A. L. Gutierrez-Aitken, J. Singh, P. Bhattacharya, and S. Lourdudoss, *Proceedings of IEEE/Cornell Conference on Advanced Concepts in High-Speed Semiconductor Devices and Circuits*, 364, Ithaca (August 1995).

[49] C. H. Lin, C. L. Chua, Z. H. Zhu, and Y. H. Lo, *Appl. Phys. Lett.*, **65**, pg. 2383, 1994.

[50] J. M. Luttinger and W. Kohn, *Physical Review*, **97**, pg. 869, 1955.

[51] P. Lawaetz, *Phys. Rev. B*, **4**, pg. 3460, 1971.

[52] J. P. Loehr and J. Singh, *IEEE J. Quantum Electron.*, **27**, pg. 708, 1991.

[53] Y. Lam, PhD Thesis, University of Michigan, 1993.

Reproduced with permission of the copyright owner. Further reproduction prohibited without permission.

[54] P. Bhattacharya, *Semiconductor Optoelectronic Devices*, Chapter 3. Englewood Cliffs, NJ: Prentice-Hall (1994).

[55] Y. Arakawa, K. Vahala, and A. Yariv, *Appl. Phys. Lett.*, **45**, pg. 950, 1984.

[56] N. Tessler and G. Eisenstein, *IEEE J. Quantum Electron.*, **29**, pg. 1586, 1993.

[57] H. Yoon, PhD Thesis, University of Michigan, 1996.

[58] G. D. Sanders and Y. C. Chang, *Phys. Rev. B*, **35**, pg. 1300, 1987.

[59] H.C.Casey and M. Panish, *Heterostructure Lasers*, New York: Academic Press, 1978.

[60] L. G. Melcer, J. R. Karin, R. Nagarajan, and J.E. Bowers, *IEEE J. Quantum Electron.*, **27**, pg. 1417, 1991.

[61] G. P. Agrawal and N. K. Dutta, , *Long-Wavelength Semiconductor Lasers* . New York: Van Nostrand Reinhold, 1986

[62] J. E. Bowers, *Solid State Electron.*, **30**, pg. 1, 1987.

[63] M. Lax, *Phys. Rev. B*, **160**, pg. 290, 1967.

[64] T. Takahashi and Y. Arakawa, *IEEE J. Quantum Electron.*, **27**, pg. 1824. 1991.

[65] T. Tanaka, J. Singh Y. Arakawa, and P. Bhattacharya, *Appl. Phys. Lett.*, **62**, pg. 756, 1993.

[66] D. Marcuse, *IEEE J. Quantum Electron.*, **20**, pg. 1139, 1984.

[67] K. Y. Lau and A. Yariv, *Appl. Phys. Lett.*, **47**, pg. 84, 1985.

[68] *IEEE J. Quantum Electron.*, **23**, pg. 1039, 1987.

[69] M. Jinno, *IEEE Photon. Technol. Lett.*, **5**, pg. 1140, 1993.

[70] X. Zhang, private communication.

[71] D. Klotzkin, K-C. Syao, and P. Bhattacharya, "Modulation Characteristics of High Speed (f_{-3dB}=20 GHz) Tunneling Injection InP/InGaAsP 1.55 μm Ridge Waveguide Lasers Extracted from Optical and Electrical Measurements," submitted to *IEEE J. Lightwave Tech.*, March 1997.

[72] D. Klotzkin, K. Kamath, and P. Bhattacharya, unpublished.

[73] D. Klotzkin, X. Zhang, and P. Bhattacharya, "Carrier Dynamics in High Speed (f_{-3dB}¿40 GHz) 0.98 μm Multiquantum Well Tunneling Injection Lasers Determined from Electrical Impedance Measurements," submitted to *IEEE Photon. Technol. Lett.*, October 1996.

Reproduced with permission of the copyright owner. Further reproduction prohibited without permission.

[74] M. J. Adams, *An Introduction to Optical Waveguides* . New York: Wiley, 1981.

[75] H. Kogelnik, "Theory of Optical Waveguides", in *Guided-Wave Optoelectronics*, T. Tamir, ed., New York: Springer-Verlag 1990.

[76] P. Kendall, M. J. Adams, S. Ritchie, and M. J. Robertson, *IEEE J. Quantum Electron.*, **QE-12**, pg. 378, 1976.

[77] P. N. Robson and P. C. Kendall, *Rib Waveguide Theory by the Spectral Index Method*, Somerset: Wiley, 1990).

[78] W. P. Huang, C. L. Xu, S. T. Chu, and S. K. Chaudhuri, *IEEE J. Lightwave Tech.*, **11**, pg. 1209, 1993.

[79] R.Y. Chan and J.M. Liu, *IEEE Photon. Technol. Lett.*. **18**. pg. 1001, 1994.

[80] C. M. Herzinger, C. C. Liu, T. A. DeTemple, and W. C. Chiu, *IEEE J. Quantum Electron.*, **29**, pg. 2273, 1993.

[81] I. Vurgaftman and J. Singh, *Appl. Phys. Lett.*, **66**, pg. 288, 1995.

[82] K. S. Yee, **AP-14**, pg. 302, 1966.

[83] S. T. Chu and S. K. Chaudhuri, *IEEE J. Lightwave Tech.*, bf. 7, pg. 2033. 1989.

[84] I. Vurgaftman, PhD Thesis, University of Michigan, 1995.

[85] J. Strikwerda, *Finite Difference Schemes and Partial Differential Equations*, Chapters 1-3. Pacific Grove, CA: Wadsworth and Brooks, 1989.

[86] A. R. Mitchell, *Computational Methods in Partial Differential Equations*, Chapter 1. Aberdeen: Aberdeen University Press (1969).

[87] Ye G. D'Yakanov, Z. Vycisl Mat. i Mat. Fiz, **3**, pg. 385, 1983.

[88] A. Taflove, *Computational electrodynamics: the finite-difference time-domain method* . Boston: Artech House (1995).

[89] J.-P. Berenger, J. Computational Physics, **114**, pp. 185-200, 1994.

[90] D. S. Katz, E. T. Thiele, and A. Taflove, IEEE. Microwave and Guided Wave Letters, **4**, pp. 268-270, 1994.

[91] J. Todd, *Survey of Numerical Methods* . New York: McGraw-Hill (1962).

[92] R. S. Varga, *Matrix Iterative Analysis* . Englewood Cliffs, NJ: Prentice-Hall (1962).

Reproduced with permission of the copyright owner. Further reproduction prohibited without permission.

[93] Y. Yuan, R. Jambunathan, J. Singh, and P. Bhattacharya, *IEEE J. Quantum Electron.*, **33**, pg. 408, 1997.

[94] R. Jambunathan, Y. Yuan, J. Singh, and P. Bhattacharya, Proc. SPIE, **3006**, pg. 222, Optoelectronic Integrated Circuits, 1997.

[95] Y. Yuan, PhD Thesis, University of Michigan, 1997.

[96] P. McIloy, K. Kurobe, and Y. Uematsu, *IEEE J. Quantum Electron.*, **21**, pg. 1958, 1985.

[97] J. Wilcox, G. Peterson, S. Ou, J. Yang, M. Jansen, and D. Schechter, *J. Appl. Phys.*, **64**, pg. 6564, 1988.

[98] H. T. Jiang, private communication.

[99] S. Ramo, J. R. Whinnery, and T. Van Duzer, *Fields and Waves in Communication Electronics* . New York: Wiley (1984).

[100] W. Cheney and D. Kincaid, *Numerical Mathematics and Computing.* Pacific Grove, CA: Brooks/Cole (1985).

[101] D. Yevick, J. Yu, W. Bardyszewski, and M. Glasner, *IEEE Photon. Technol. Lett.*, **7**, pp. 658-660, 1995.

[102] A. V. Oppenheim, A. S. Willsky, and I. T. Young, *Signals and Systems*, Chapters 3–4. Englewood Cliffs, NJ: Prentice-Hall (1983).

[103] Y.Yuan, T. Brock, and P. Bhattacharya

[104] K. Tai, L. Yang, H. Wang, J. D. Wynn, and A. Y. Cho, *Appl. Phys. Lett.*, **56**, pp. 2496-2498, 1990.

[105] S. H. Yang, S. Smith, J. Fitz, and C. H. Lee, *IEEE Photon. Technol. Lett.*, **8**, pp. 337-339, 1996.

[106] S.-T. Yen and C.-P. Lee, *IEEE J. Quantum Electron.*, **32**, pp. 1588-1595, 1996.

[107] M. Gerhold, A. Onischenko, J. Sarma, and P. Bhattacharya, "Novel Design of a Hybrid Cavity Surface Emitting Laser", submitted to *IEEE J. Quantum Electron.*, March, 1997.

[108] K. J. Beernink, K. Sun, R. L. Thornton, and D. W. Treat, *Appl. Phys. Lett.*, **68**, pp. 284-286, 1996.

Reproduced with permission of the copyright owner. Further reproduction prohibited without permission.